

UNIVERSITÀ DEGLI STUDI DI PADOVA

SCUOLA DI SCIENZE

Dipartimento di Geoscienze
Direttore Prof. Cristina Stefani

TESI DI LAUREA MAGISTRALE
IN
GEOLOGIA E GEOLOGIA TECNICA

THE TERTIARY PEGMATITE FIELD OF THE CENTRAL ALPS IN THE SOUTHWESTERN BERGELL INTRUSION

Relatore: *Prof. Giorgio Pennacchioni*
Correlatori: *Dott.ssa Anna Maria Fioretti*
Dott. Alberto Ceccato

Laureando: Simone Papa

ANNO ACCADEMICO 2015 / 2016

INDEX

1. INTRODUCTION 1

2. GEOLOGICAL SETTING 5

2.1 Bergell pluton 5

2.1.1 Tonalite
2.1.2 Granodiorite
2.1.3 Transition zone between granodiorite and tonalite
2.1.4 Structure of the pluton
2.1.5 Emplacement and syn-magmatic deformation

2.2 Novate granite 12

2.3 Pegmatite field of the Central Alps 12

3. FIELD OBSERVATIONS 16

3.1 Intrusive rocks of the Bergell pluton 17

3.2 Dykes and veins 19

3.2.1 Set A
3.2.2 Set B
3.2.3 Set C
3.2.4 Set D
3.2.5 Discussion

3.3 Ductile deformation 29

3.3.1 Distributed and localised ductile deformation
3.3.2 Ductilely deformed quartz veins

3.4 Brittle deformation 37

4. PETROGRAPHY OF THE SAMPLED DYKES 42

4.1 Petrographic description 43

4.1.1 Pegmatite dykes
4.1.2 Granite dykes

4.2 Separation of minerals for dating 48

5. GEOCHEMISTRY OF THE SAMPLED DYKES 50

5.1 Geochemical characterisation 50

5.1.1 Silica vs oxide Harker variation diagrams
5.1.2 AFM diagram and classification of granitoids
5.1.3 Trace elements

5.2 Classification of pegmatites 60

6. SUBMAGMATIC AND SOLID STATE DEFORMATION 64

6.1 Submagmatic to post-magmatic deformation of the sampled dykes . .64

6.2 Ductile deformation of the quartz veins 65

6.2.1 Low-strain domain
6.2.2 Medium-strain domain
6.2.3 High-strain domain

6.3 Deformation history of the quartz veins 73

6.4 Crystallographic preferred orientations of the quartz veins 74

6.4.1 Medium-strain domain
6.4.2 High-strain domain
6.4.3 CPO evolution and comparison with the Adamello pluton quartz veins

6.5 Granitoid mylonite 78

6.6 Brittle deformation 78

7. CONCLUSIONS 82

7.1 The pegmatite field of the Central Alps in the Val dei Ratti area 82

7.2 Post-magmatic deformation in the Bergell pluton 83

7.3 Future development 83

BIBLIOGRAPHY 86

ANALYTICAL TECHNIQUES 93

ACKNOWLEDGEMENTS 95

1. INTRODUCTION

The tectonic stack of Alpine metamorphic units of the Central Alps hosts the largest field of Tertiary pegmatites of the Alps. Recent studies on these pegmatites attempted a comprehensive multidisciplinary approach integrating mineralogical, petrographic, structural and geochronological data for two selected areas in the central part of the pegmatite field: namely the 'Codera area', at the western border of the Bergell batholith, and the 'Bodengo area', more to the east and to the south, between the Mera and Mesolcina valleys (Guastoni et al., 2014; Fig. 1.1). The two areas contain pegmatites with a similar degree of evolution and mineral contents; but markedly different texture, orientation and deformation. $^{208}Pb/^{232}Th$ dating on monazite yielded two different age groups with Codera pegmatites ranging from 28 to 25 Ma, and Bodengo ones from 23 to 19 Ma (Pozzi, 2014). Whether this indicates the occurrence of two distinct intrusion events or a migration toward the west of the pegmatite field with time, it is still unclear.

In this study we investigated a new area of the pegmatite field located in the upper Valle dei Ratti, at the southwestern border of the Bergell batholith. This area was chosen because:

i) it is close to the 'Codera area' of the previous study (about 7 kilometers to the south; Fig. 1.1);
ii) it is completely within the Bergell pluton, and therefore the intrusion age of the Bergell pluton (32-30 Ma; e.g. von Blanckenburg et al. 1992), provides a maximum age constraint for the dykes intrusion;
iii) the area contains a swarm of numerous pegmatitic dykes with different orientations, which is already visible in aerial photographs;
iv) glacier polished surfaces provide optimal outcrops that allow a detailed field study.

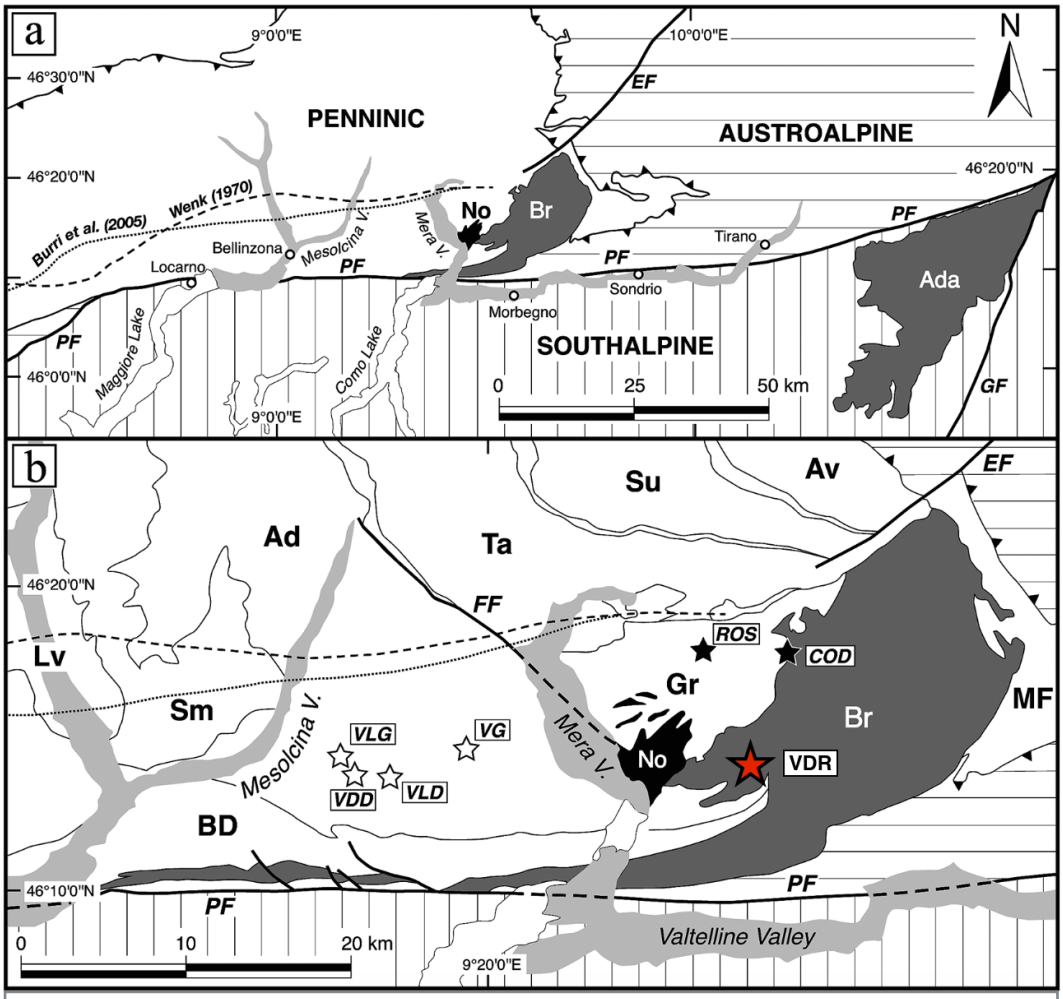


Figure 1.1 **a)** Simplified structural map of the Central Alps with the field of the Alpine (Oligocene–Miocene?) pegmatites as reported by Wenk (1970) and Burri et al. (2005) outlined by dashed and dotted lines, respectively. The map also shows the two major Tertiary batholiths of Adamello (**Ada**) and Bergell (**Br**), in grey, and the smaller and younger Novate stockwork intrusion, in black. The thick black lines represent the Periadriatic Fault (***PF***), the Giudicarie Fault (***GF***), and the Engadine Fault (***EF***). The light grey areas represent quaternary deposits along major valleys. **b)** Structural map of the Bergell batholith and the region on the west showing the locations of the Codera (black stars) and the Bodengo areas (empty stars). The red star indicates the area studied in this work, located in the upper Valle dei Ratti. The map also shows the main boundaries (thin black lines) of the Penninic tectonic units: **Lv** = Leventina; **Sm** = Simano; **Ad** = Adula; **Ta** = Tambò; **Su** = Suretta; **Av** = Avers; **BD** = Bellinzona-Dascio; **MF** = Malenco-Forno. The thick black line labeled **FF** is the Forcola Fault. Figure and caption from Guastoni et al. (2014)

We chose to study a limited but meaningful area, where several sets of discordant dykes with different orientations and different features crosscut each other. The aim of the fieldwork was (i) to recognise the intrusion sequence of dykes and (ii) to sample representative examples of each generation.

The field observation have been integrated by the mineralogical and geochemical characterisation of the different dykes. The final aim of the work is dating the different dykes whose relative sequence of emplacement had already been established in the field. Preliminary work for dating has been performed during the thesis with separation of monazite, apatite and zircon from 2 sets of samples each representative of the whole sequence of dykes of the area that include at least 4 stages of dyke magmatism. The aim of the study is to discriminate between the following possible scenarios:

i) in the Val dei Ratti area it is exposed a dyke intrusion sequence that cover the entire time span of the pegmatitic field intrusion, with older ‘Codera-like’ dykes and younger ‘Bodengo-like’ dykes;
ii) in the Val dei Ratti area it is represented a polyphasic magmatism of ‘Codera-like' age, and the younger ‘Bodengo-like’ dykes are not represented.

This will give more information in order to discriminate whether there was a migration in time and space of the pegmatitic magmatism or in every different area of the pegmatitic field all the dykes intrusion events are represented.

During the fieldwork, it was also analysed the deformation sequence (mostly ductile) that took place during the cooling of the pluton. As will be shown in this thesis, in the Val dei Ratti area the sequence of dykes intrusion is crosscut by ductilely deformed quartz veins. The presence of quartz veins is common in similar geological settings. Ductilely deformed quartz veins have already been studied by the structural geology group from the University of Padova in the Adamello, Rieserferner and Lake Edison (Sierra Nevada) plutons (e.g. Pennacchioni et al., 2010; Ceccato et al., 2015; Pennacchioni & Zucchi, 2013

respectively). They represent a perfect natural sample for the study of ductile deformation in quartz for at least three reasons:

i) the veins are monomineralic and so there is no strain partitioning between different minerals;
ii) after emplacement the pluton cools rapidly to the ambient host rock temperature, and so the veins open and are deformed in a short time span, during which the direction of regional shortening remains constant;
iii) the rapid cooling ed exhumation preserves the deformed microstructures, avoiding the complex deformational history that takes place during the exhumation of metamorphic terrains.

In all the studied cases, a standard evolution of the deformation in the veins has been observed. It involves a first phase of stretching of the coarse-grained vein crystals to develop mono-crystalline ribbons, followed by the dismantling of the ribbons by means of conjugated 'discrete zones of recrystallisation', and by a latest stage of pervasive recrystallisation.

The second aim of the thesis is thus to study the optical microstructure and the CPO of the quartz veins, in order to compare the ductile post-magmatic deformation of the Bergell pluton with the analogous sequences of deformation already studied in the Adamello, Rieserferner and Sierra Nevada plutons. The study of the quartz veins and the comparison with similar structures in similar geological settings, can give informations about the temperature at which the ductile deformation occurred. This would be a minimum temperature for the dykes intrusion, since all the generations of dykes were crosscut by the quartz veins.

2. GEOLOGICAL SETTING

For the brief introduction to the geology of the Bergell pluton, we refer to the classical works of Berger and Gieré, 1995; Davidson et al., 1996 and Schmid et al., 1996 and to the review concerning the Bergell pluton in Rosenberg, 2004. For the chapters about the Novate granite and the pegmatite field, we mainly refer to the works of Ciancaleoni and Marquer, 2006; Liati et al., 2000 and Guastoni et al., 2014.

2.1 Bergell pluton

The Bergell pluton represents one of a few major igneous complexes of Tertiary age in the Alps (together with the Adamello, Rieserferner and Pohorje plutons and other minor intrusions). All Tertiary plutons in the Alps are found in the vicinity of the Periadriatic Fault System (PFS), hence they were termed Periadriatic (Salomon, 1897).

The Bergell pluton is composed primarily of tonalite and granodiorite, with minor amounts of gabbro, hornblendite and diorite (Wenk, 1973 and 1986; Wenk et al., 1977; Trommsdorff and Nievergelt, 1983; Reusser, 1987; Diethelm, 1989). It is a composite pluton in that mafic rocks (predominantly tonalite and minor amounts of gabbro and other mafic rock types) form the margins of the pluton with granodiorite occupying the core and north-western margin. A zone where mingling and mixing occurred, the 'Transition Zone' (The 'Übergangszone' of Moticska, 1970 and Wenk and Cornelius, 1977), is commonly present between the granodiorite and the tonalite, but is best developed in the west. In the east, cross-cutting relationships between tonalite and granodiorite demonstrate the slightly younger crystallisation age of the granodiorite in this part of the pluton (Gyr, 1967; Trommsdorff and Nievergelt, 1983; Berger and Gieré, 1995), consistent with radiometric dating. Von Blanckenburg (1992) showed that the tonalite and

granodiorite at the eastern margin cooled through their solidus at 32 and 30 Ma, respectively (see review by Hansmann, 1996).

In the areas of interest of our work, only two of the lithologies of the Bergell pluton crop out: namely the tonalite and the granodiorite.

2.1.1 Tonalite

The tonalite is predominantly composed of plagioclase, quartz, hornblende, biotite and small amounts of epidote and K-feldspar (Reusser, 1987). It has a well-developed foliation defined by the preferred orientation of biotite and plagioclase laths, and/or a lineation defined by the preferred alignment of elongate hornblende crystals.

Structural observations at the eastern, western and southern margin of the pluton revealed a continuous transition from magmatic flow to high-temperature solid-state syn-intrusive deformation (Berger and Gieré, 1995; Davidson et al., 1996; Berger et al., 1994; Rosenberg et al., 1994; Berger et al., 1996; Berger and Stünitz, 1996). Foliations and lineations along the western margin of the pluton are always concordant with those of the surrounding rocks. Geobarometry based on the Al content in hornblende indicates that the pressure of final crystallization of the tonalite decreases from greater than 8 kbars in the west to less than 5 kbars in the northeast (Reusser, 1987; Davidson et al., 1996).

2.1.2 Granodiorite

The granodiorite mainly contains plagioclase, quartz, K-feldspar and biotite, and (in some places) hornblende (Gyr, 1967; Reusser, 1987). K-feldspar occurs both as megacrysts (3-5 cm, but sometimes > 10 cm) and in the matrix. Near the tonalite contact in the west, the granodiorite (and the Transition zone) usually has a well-developed foliation marked by the preferred orientation of biotite, whereas

the alignment of K-feldspar megacrysts defines a mineral lineation. In the east, and center of the pluton, foliations and lineations are usually subtle or not present, except close to the contact with the country rocks (Drescher-Kaden and Storz, 1926; Berger and Gieré, 1995). In some areas the granodiorite exhibits a distinct magmatic layering, documented by accumulation of K-feldspars that are oriented parallel to the layers. A solid-state overprint is sporadically observed in quartz domains (Wenk, 1973). However, this overprint is very much weaker than that observed in the tonalite and does not define a pervasive solid-state foliation.

Both the granodiorite and tonalite contain abundant homogeneous enclaves of dioritic to monzonitic composition (‘endogene Xenolithe’ of Gansser and Gyr, 1964; ‘mafic enclaves’ in the present work). These inclusions are more common in the granodiorite, where they are typically oval to round in shape and often occur concentrated in large numbers. In the tonalite, the enclaves are usually present as schlieren. Diethelm (1990) concluded that these enclaves represent products of mingling between injected basic magmas and the slowly cooling tonalite and granodiorite magmas. In the eastern part of the intrusion, the shapes of mafic enclaves reveal a strain concentration towards the contact of the pluton (Berger and Gieré, 1995).

2.1.3 Transition zone between granodiorite and tonalite

The Transition zone (“Übergangszone” of Moticska, 1970; Wenk and Cornelius, 1977; Hansmann, 1981), found only in the southern and southwestern parts of the intrusion, is an inhomogeneous zone characterized by alternating layers of tonalitic and granodioritic rocks, probably due to mingling between the tonalite and granodiorite magmas. Magmatic mixing is also indicated in the Transition zone by the presence of rocks with intermediate chemical compositions between the tonalite and the granodiorite (Reusser, 1987).

Contacts between the Transition zone and the tonalite are delineated by the first occurrence of K-feldspar megacrystals. The Transition zone-granodiorite contact is less clear and often gradational. When present, fabrics within the Transition zone are concordant with the surrounding rocks. These observations suggest that tonalite and granodiorite had a common magmatic stage, at least in the southern and southwestern parts of the pluton.

2.1.4 Structure of the pluton

Post-intrusive tilting and erosion of the Bergell pluton resulted in the present-day exposure of a 12 km deep crustal section between the eastern and western ends of the pluton, as supported by the following observations: (i) all structures plunge to the east (Cornelius, 1915; Staub, 1918; Trommsdorff and Nievergelt, 1983; Rosenberg et al., 1995; Schmid et al., 1996b); (ii) petrologic data indicate a westward, post-intrusive pressure increase of 3–4 kbar (Reusser, 1987; Davidson et al., 1996) and a westward temperature increase (Rosenberg and Stünitz, 2003); (iii) geochronologic data show progressively younger ages from east to west (Villa and von Blanckenburg, 1991), and finally, (iv) paleomagnetic data, suggest west-side-up tilting around a N-S striking axis (Rosenberg and Heller, 1997). Moreover, 3 km of relief through the pluton, allow the reconstruction of the three-dimensional shape of the intrusive body (Fig. 2.1).

The floor of the Bergell's main body is exposed over more than 30 km along the western contact, and within a tectonic window in the central part of the pluton. This contact is everywhere concordant with a high-temperature, syn-migmatitic shear zone, which follows a previous nappe boundary (Diethelm, 1989; Davidson et al., 1996), corresponding to the North-Penninic suture zone (Schmid et al., 1996) i.e. the Misox zone between the Adula and Tambo nappes (Fig. 2.1). In profile view (Fig. 2.1), the pluton occupies the same structural position as the Tambo and Suretta nappes north of the Engadine line, i.e. between the Adula-Gruf

unit at the base and the South-Penninic Malenco-Forno and Lizun ophiolite complexes on top, dissected by the post-magmatic Engadine line (Schmid and Froitzheim, 1993). The uppermost part of the exposed pluton was intruded immediately below the base of the Austroalpine nappes (e.g. Margna nappe), whose temperature was less than 300°C at the time of emplacement. As a result, the country rocks above the roof of the pluton behaved as a rigid lid (Laubscher, 1983b) while the migmatitic floor of the pluton was still highly ductile.

The southern margin of the pluton, commonly termed the tail, is a 40 km long, steep tabular body of tonalite, sub-parallel to the Periadriatic Fault System (Fig. 1.1). The tonalitic tail belongs to the Periadriatic mylonitic zone. According to

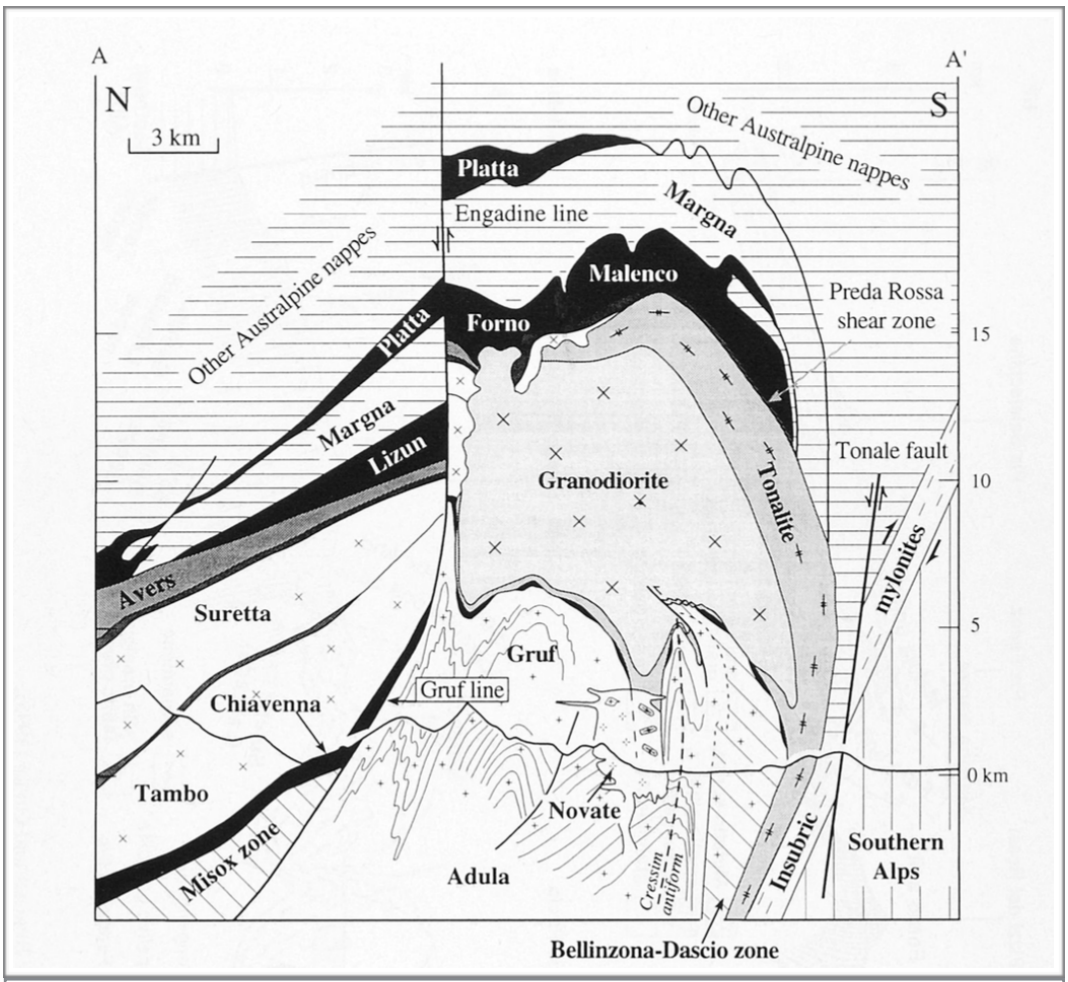


Figure 2.1 Synthetic N-S section through the Bergell pluton, after Schmid et al. (1996b).

Rosenberg et al. (1995), Davidson et al., (1996) and Berger et al. (1996), this tabular body represents the feeder dyke of the Bergell intrusion.

2.1.5 Emplacement and syn-magmatic deformation

After ascent along the transpressive PFS, final emplacement occurred in two stages (Fig. 2.2). First, the magmas were emplaced to the north of the PFS, along

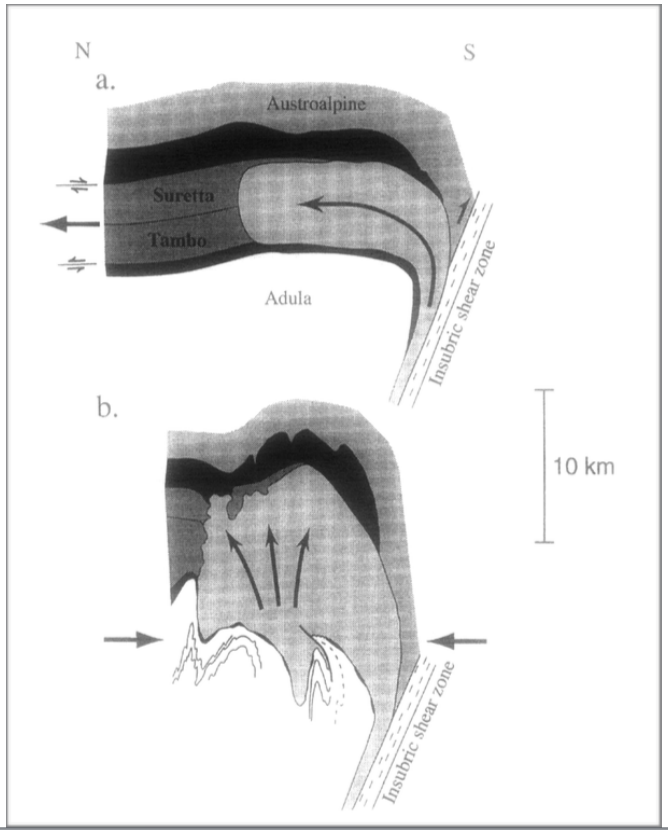


Figure 2.2 Schematic cross-sections depicting the intrusion history of the Bergell pluton. (a) The Bergell pluton (light gray) is emplaced as a magma from south to north over the underlying Adula nappe. The well-developed foliation along the base of the pluton probably formed at this time (the first deformation step, see text). (b) The base of the Bergell pluton is folded during N-S compression and simultaneous E-W extension while it is still partially molten (the second deformation step, see text). Shortening of the base of the pluton forces remaining magma to intrude the crust at higher structural levels (arrows), causing flattening of the contact metamorphic aureole near the top of the pluton (eastern contact). Figure and caption from Davidson et al. 1996.

an active and gently inclined nappe contact. During this phase a magmatic foliation formed, parallel to the foliation of the underlying country rocks (Davidson et al., 1996). Emplacement of the pluton is interpreted to be part of a regional deformation phase (the Niemet-Beverin phase of Schmid et al., 1996), accompanied by vertical extrusion in the Southern Steep Belt (Merle, 1994; Berger et al., 1996) and late-stage differential northward displacement of the Tambo and Suretta nappes (see Schmid et al., 1990; Merle and Guillier, 1989).

Second, the base of the pluton and its country rocks were folded, still in the presence of melt, as indicated by crosscutting relationships between folds and tonalitic veins (Rosenberg et al., 1995) and by microstructural observations of tight folds lacking any solid-state overprint (Davidson et al., 1996). The axial planes of these folds can be traced from the base of the pluton westward, into the underlying country rocks for several tens of kilometers, indicating that the pluton was folded during large-scale regional N-S shortening.

At higher structural levels, now represented by the eastern contact, intense E-W horizontal shortening in the margin and metamorphic aureole (Conforto-Galli et al., 1988; Berger and Gieré, 1995) resulted in a steep, north- south striking synmagmatic foliation (Berger and Gieré, 1995), which is perpendicular to the regional structures of Oligo-Miocene age in the area. This shortening event was therefore ascribed to final emplacement of the pluton by radial expansion or ballooning (Conforto-Galli et al., 1988; Berger and Gieré, 1995). Syn-magmatic folding at the base of the Bergell and ballooning at its top occurred simultaneously (Rosenberg et al., 1995).

Giger and Hurford (1989) show that the Bergell pluton cooled rapidly during and after crystallisation and suggest that the entire Central Alps were exhumed as more or less a rigid block due to strain localization within the Insubric mylonite belt during backthrusting. Therefore, backthrusting along the Insubric shear zone and associated tilting of the pluton must have outlasted the synmagmatic deformations.

2.2 Novate granite

A magmatic body in close spatial relation to the Bergell pluton is the Novate (San Fedelino) granite, that crops out in the Val Mera, south of Chiavenna (Fig. 1.1). The Novate granite is not a single large intrusive body but is composed by a multitude of dykes and stocks of up to several hundreds of metres in size (Gianola et al., 2014). The Novate granite is a fine-grained, locally garnet-bearing, S-type two-mica peraluminous leucogranite. It consists of quartz, plagioclase, K-feldspar, biotite, muscovite, and in many places garnet (Repossi, 1915; Piccoli, 1961; Moticska, 1970). Based on geochemical criteria, the Novate granite is not related genetically to the calc-alcaline Bergell suite. It rather derived by partial melting of crustal rocks during late-Alpine decompression (e.g. Reusser, 1987; Oschidari and Ziegler, 1992; von Blanckenburg et al., 1992).

The granite is commonly foliated, with the foliation defined by the preferred orientation of micas. However, the Novate granite crosscuts the late back-folding structures and Bergell pluton fabrics (Wenk, 1973; Berger et al., 1996). Hence, the intrusion of this granite is clearly younger than final emplacement and syn-magmatic folding of the Bergell pluton (Davidson et al., 1996, Berger et al., 1996). This is confirmed by the U-Pb SHRIMP dating of zircon from the Novate granite that yielded an age of intrusion of 24.0 ± 1.2 Ma (Liati et al., 2000).

2.3 Pegmatite field of the Central Alps

The tectonic stack of Alpine nappes of the Central Alps hosts the largest field of Tertiary (Oligocene–Miocene?) pegmatites of the Alps. This field is sharply delimited to the south by the PFS and extends, with a N–S width of over 15 km, for about 100 km from the Ossola valley (to the west) to the Sissone valley (to the east) (Fig. 1.1). Pegmatites are abundant in the southern steepened “roots” of the Alpine nappes (Southern Steep Belt, SSB: Studer 1851, Milnes 1974), adjacent to

the Periadriatic Fault, and progressively decrease in number towards the north, where the nappes become flat-lying (Stern 1966, Burri et al. 2005). The regional boundary of the pegmatite field (which includes associated aplites) was mapped by Wenk (1970) and later by Burri et al. (2005) (Fig. 1.1). The pegmatite field geographically overlaps (1) the highest-temperature domain of the Barrovian metamorphic dome (Lepontine metamorphic dome), whose isograds are discordant to the nappe boundaries and (2) the zone of Alpine migmatisation. Therefore, in the SSB the leucocratic dikes (including pegmatite and aplite) are often associated with small granitoid bodies (metric to decametric in size) and in situ leucosome segregates of the host rock (Burri et al. 2005). The interpretation of this structural assemblage is locally difficult due to the occurrence of pre-Alpine leucocratic dikes, migmatites, and granitoids (Hänny et al. 1975, Romer et al. 1996, Galli et al. 2012, 2013). The age of Alpine migmatisation and of emplacement of leucocratic dykes in the Central Alps apparently spans approximately the same age bracket as the Tertiary intrusions, whose end-members are represented by the Bergell pluton and the younger and smaller Novate stockwork intrusion. Uranium-Pb dating of monazite from orthogneisses and migmatites from the SSB of the Bodengo valley yielded an age of 23–24 Ma (Hänny et al. 1975, Köppel et al. 1980), which is slightly older than the Rb-Sr whole rock isochron age of 22 Ma. Along the western boundary of the Bergell pluton, within the Gruf complex, recent SHRIMP U-Pb dating has yielded ages in the range of 34–29 Ma for the outer rim of pre-Alpine zircons (Galli et al. 2012). These ages are consistent with field observations that migmatisation at 720–740 °C in the Gruf complex was coeval with intrusion of the Bergell pluton (Davidson et al. 1996, Berger et al. 1996, Galli et al. 2012). SHRIMP U-Pb dating of multiple zircon domains from migmatite leucosomes of the SSB close to Bellinzona (Rubatto et al. 2009) suggests protracted melting over a time span ranging from 32 to 22 Ma. Gebauer (1996) dated the migmatisation event of the SSB within the Cima Lunga nappe at 32.4 ± 1.1 Ma by SHRIMP U-Pb zircon

dating; this age indicates that migmatisation was coeval with the early phases of the Bergell intrusion.

Similarly, in the western part of the pegmatite field, pegmatites intruding amphibolite-facies mylonites of the Simplon ductile shear zone have been dated from 29 to 25 Ma (with a discordant dike as young as 20 Ma) by the U-Pb method applied to monazite and xenotime (Romer et al. 1996, Schärer et al. 1996). It is noteworthy that Romer et al. (1996) distinguished two generations of pegmatite-aplite from the same outcrop at Malesco: (1) the oldest, which intruded along the host-rock foliation and is slightly deformed, yielded an U-Pb age from monazite of 29.2 ± 0.2 Ma; (2) the youngest, which is undeformed and is discordant to the foliation, yielded an U-Pb age from xenotime of 25.5–26.5 Ma. This is consistent with the SHRIMP U-Pb zircon age of 25.1 ± 0.6 Ma obtained for a pegmatite cross cutting the Alpine foliation of the SSB more than 50 km to the east, just north of San Vittore (Gebauer 1996). This age overlaps with the Novate intrusion age determined by Liati et al. (2000), who suggested that this pluton, and coeval non-outcropping intrusive bodies, could have been the source of the numerous pegmatites and aplites of the SSB.

If on the regional scale a coincidence between magmatism, migmatisation, and pegmatite emplacement is established, on the local scale there is a conspicuous number of pegmatite dykes that apparently postdate the main phase of migmatisation and associated ductile deformation. As for the Novate intrusion, in the area between Bellinzona and the Chiavenna valley, pegmatites crosscut the folds of the Cressim backfolding phase (Nagel et al. 2002), which is associated with the steepening of the main nappe foliation and nappe boundaries in the SSB. However, Wenk (1973) noted that, though less deformed than the host Bergell intrusives, pegmatites are locally involved in ductile deformation. He also reported mutual crosscutting relationships between pegmatites and the Novate intrusion, from which he inferred that they were broadly contemporaneous. Galli et al. (2013) reported that aplite and pegmatite dikes are present within (and show

a weaker ductile overprint than) mylonites, indicating that the emplacement of these dikes was late, but still syn-tectonic.

Available Rb-Sr and K-Ar ages provide some chronological and temperature constraints on intrusion of pegmatites, though the meaning of these ages in terms of cooling temperature is still debated (e.g., Villa 1998). A summary of regional radiometric data is given by Hansmann (1996) and includes data from pegmatites, the Bergell intrusives, and metamorphic rocks. For the western Bergell tonalite, Hansmann (1996) reconstructed a cooling history (adjusted to an altitude of 1900 m a.s.l.) from magmatic conditions at 28–32 Ma to ca. 300 °C (K-Ar of muscovite and Rb-Sr of biotite) at ca. 21 Ma. A Rb-Sr muscovite age of 26.3 ± 1 Ma for a pegmatite intruding the Gruf complex in the Piana valley (a tributary of the Codera valley) could record the age of cooling through ca. 500 °C. If this assumption is correct, it provides the minimum age of the pegmatites in the area, as well as the minimum temperature for their emplacement.

3. FIELD OBSERVATIONS

The studied area is located within the southwestern part of the Bergell pluton, in the upper Val dei Ratti (province of Sondrio, Italy). The area is located at the rim of the intrusion and includes an outer domain showing an inhomogeneous alternation of tonalite and porphyric granodiorite (forming the southern part of the study area) and an inner domain of porphyric granodiorite (Fig. 3.1). In the alpine geological literature the tonalite and the porphyric granodiorite are referred to as 'Serizzo' and 'Ghiandone', respectively. The upper part of the Val dei Ratti extends from around 2250 m up to 2800 m of altitude, and provides easy accessible, relatively flat, glacier polished outcrops that are ideal for detailed

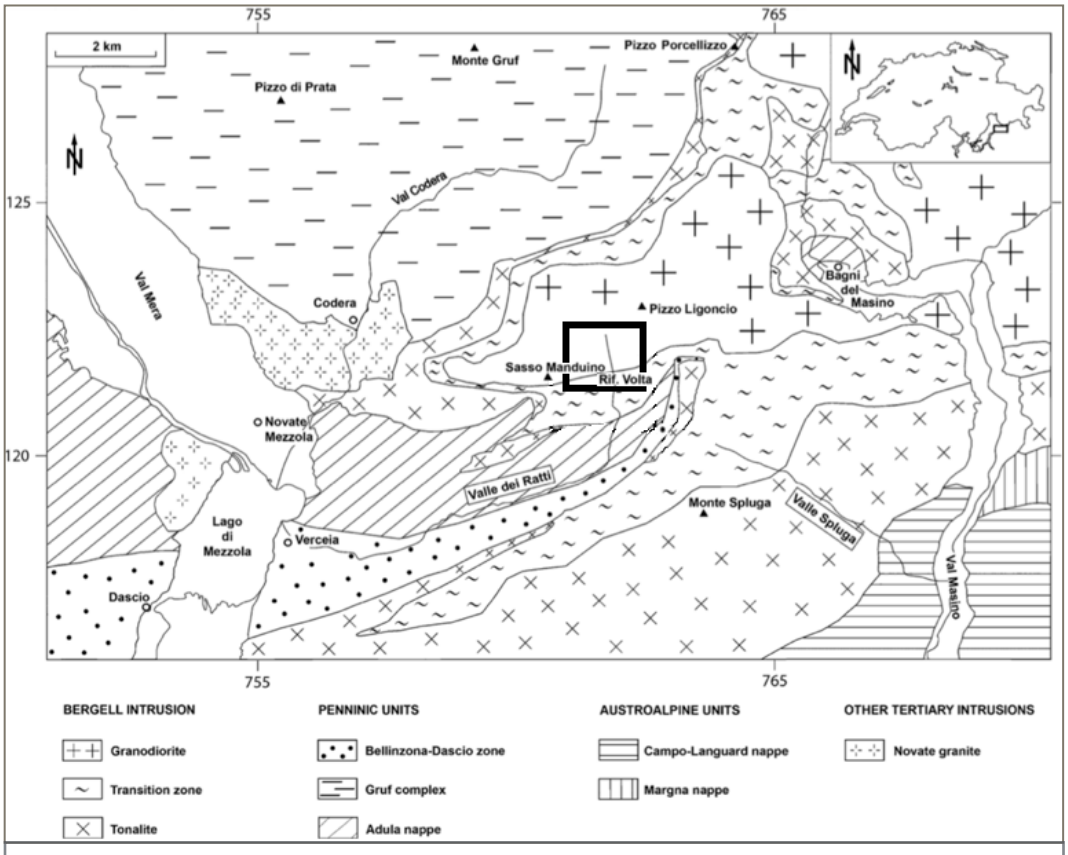


Figure 3.1 Tectono-geological sketch (modified after Berger et al., 1996) showing the studied area in the upper Valle dei Ratti. The area falls at the boundary between the Bergell Granodiorite and Transition zone.

mapping and structural analysis. The studied area is representative of structural levels of the pluton close to the base of the main body of the Bergell pluton, intruded at a depth of 22-26 km according to Davidson et al. (1996).

The intrusive rocks, as well as the country rocks, are crosscut by a swarm of leucocratic dykes (pegmatites and aplites), microgranite dykes and by a set of quartz veins. The aim of the field work was to establish: (i) the number of dyke intrusion events; and, (ii) based on the crosscutting relationships, the relative chronological sequence of the different generations of dykes and veins. Based on this analysis, representative samples of each set of dykes were sampled for petrographic, mineralogic, geochemical analysis and eventually for dating.

3.1 Intrusive rocks of the Bergell Pluton

In the studied area two different magmatic facies crop out: a porphyric granodiorite and a tonalite. The granodiorite crops out in the northern (and upper) part of the area, while toward the south the tonalite becomes dominant (Fig. 3.1). There is no sharp boundary between the two facies, but a gradational contact between the homogeneous granodiorite and a 500-800 m wide area characterised by alternating layers of tonalitic and granodioritic rocks. This inhomogeneous area is referred to as the Transition zone in the literature.

The tonalite in the studied area consist of medium grained rocks with macroscopically visible plagioclase, quartz, amphibole and biotite (Fig. 3.2d). The granodiorite is characterised by a porphyric texture defined by idiomorphic megacrystals of K-feldspar (up to 10 cm in length; Fig. 3.2a); local accumulations of these megacrystals are common (Fig. 3.2b). The matrix mainly consists of plagioclase, quartz and biotite. Mafic enclaves (Fig. 3.2a) are common in both the tonalite and the granodiorite, and have been interpreted as magma mingling features (Moticska 1970).

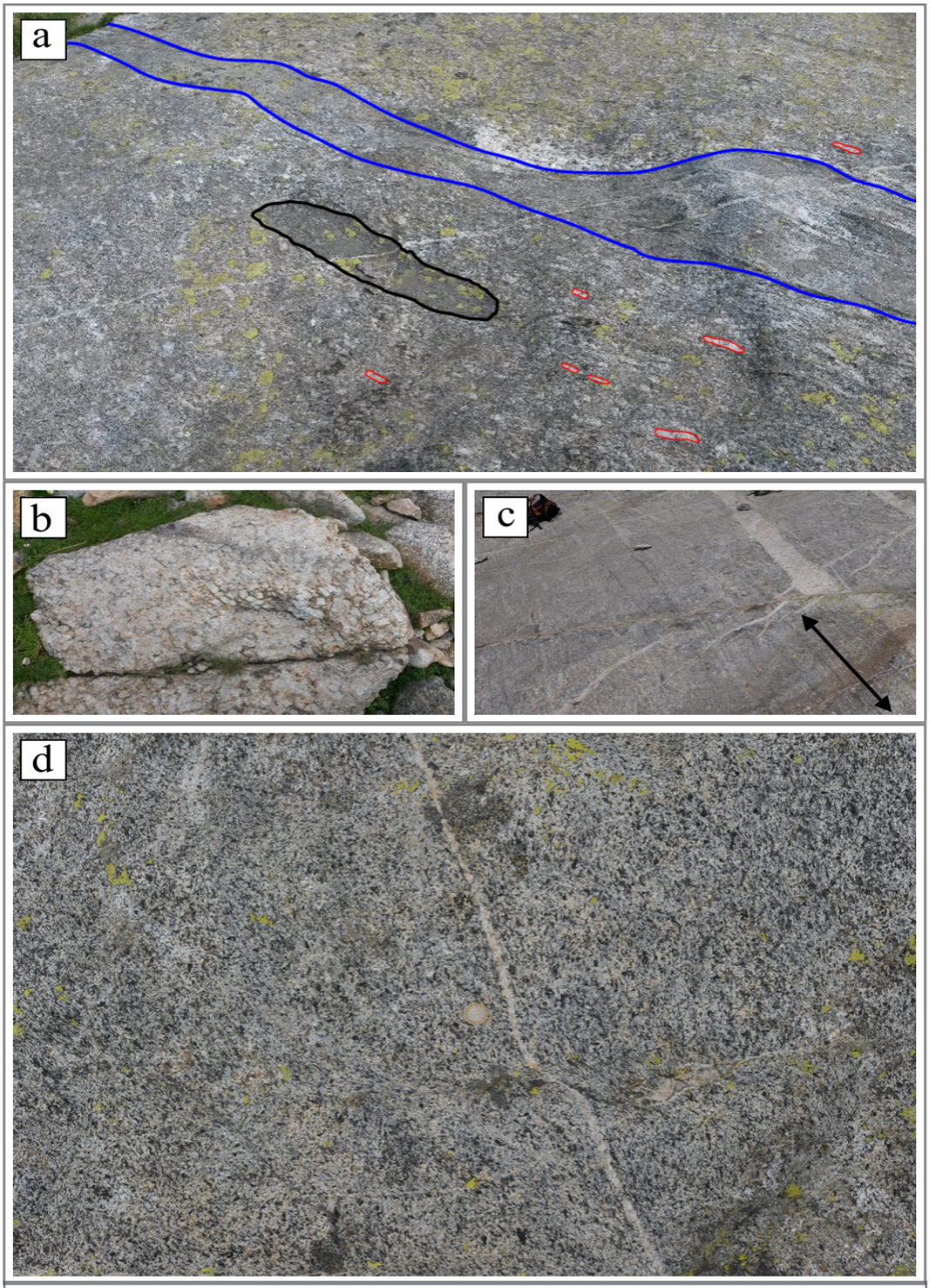


Figure 3.2 **a)** Magmatic foliation in the granodiorite. An elongated mafic enclave and the compositional banding are highlighted in black and blue respectively. The larger megacrystals (in red) are up to 5-7 cm long. **b)** Accumulation of K-feldspar megacrystals. **c)** Compositional banding in the transition zone. **d)** Typical appearance of the tonalite (1 euro coin for scale).

Granodiorites and tonalites are characterised by a strong magmatic foliation striking E-W and steeply dipping (average: 356/76, dip direction/dip; Fig. 3.3), i.e. subparallel to the pluton boundary and to the lithologic contact between the granodiorite and the transition zone (Fig. 3.1). The magmatic foliation is outlined by:

i) the preferred orientation of the K-feldspar megacrystals;

ii) a compositional banding;

iii) the elongation of mafic enclaves (Fig. 3.2a).

These have all been interpreted as magmatic flow features (e.g. Gianola et al., 2014; Davidson et al., 1996). Slightly elongated or flame-shaped mafic enclaves are probably deformed during a still partial molten state. The compositional banding (Fig. 3.2a,c) is particularly evident in the Transition Zone. It consists of an alternation of leucocratic and melanocratic bands, the latter being enriched in biotite and amphibole. This layering is mostly absent in the main granodiorite zone.

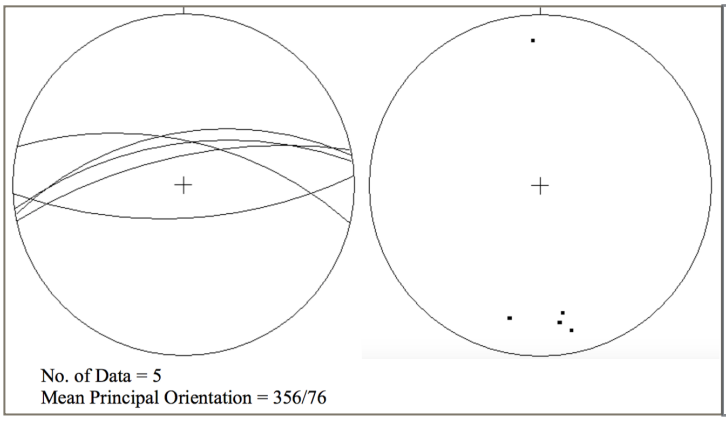


Figure 3.3 Stereoplots (lower hemisphere, equal area) of the orientation of the magmatic foliation, plotted as planes on the left-hand side and as pole to planes on the right.

3.2 Dykes and veins

The field work was mainly focused on the study of the complex network of dykes and veins crosscutting the fabrics of the Bergell pluton. These dykes include three main rock types: aplites, pegmatites and granites. Aplites contains mainly K-

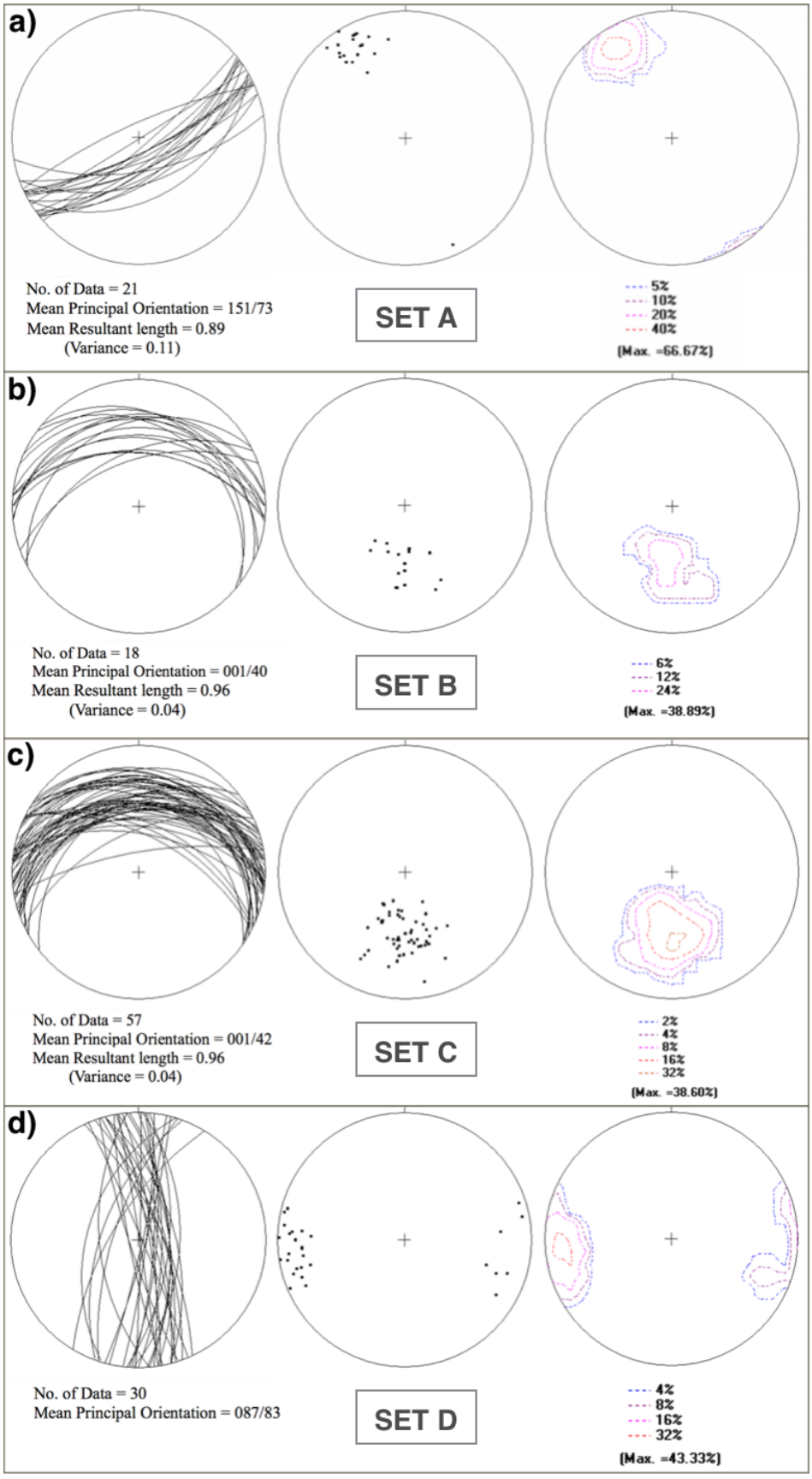

a)
No. of Data = 21
Mean Principal Orientation = 151/73
Mean Resultant length = 0.89
(Variance = 0.11)
SET A
5%
10%
20%
40%
(Max. =66.67%)
b)
No. of Data = 18
Mean Principal Orientation = 001/40
Mean Resultant length = 0.96
(Variance = 0.04)
SET B
6%
12%
24%
(Max. =38.89%)
c)
No. of Data = 57
Mean Principal Orientation = 001/42
Mean Resultant length = 0.96
(Variance = 0.04)
SET C
2%
4%
8%
16%
32%
(Max. =38.60%)
d)
No. of Data = 30
Mean Principal Orientation = 087/83
SET D
4%
8%
16%
32%
(Max. =43.33%)

Figure 3.4 (previous page) Stereographic plots (lower hemisphere, equal area) of the orientation of the four sets of dykes. Data are plotted as planes in the left-hand column, and as poles to planes in the other two.

feldspar, plagioclase, quartz, biotite and locally garnet, while pegmatites, in the coarse-grained most evolved zones, can also contain macroscopic muscovite and aquamarine beryl. However, the same dyke commonly display a composite structure, with an asymmetrical alternation of pegmatite and aplite layers and the structure of the dyke con change along strike from one type to the other.

The granitic dykes include either layered medium-grained and homogeneous fine-grained dykes, and contain mostly quartz, K-feldspar, plagioclase, biotite and muscovite. The layered structure is due to the presence of biotite-rich layers.

The field relationships allowed the recognition of four main sets of dykes, with different orientations and consistent mutual crosscutting relationships. Most of the dykes are locally continuous over distances of tens to hundreds of metres. We will refer to the four sets as type-A, B, C and D dykes in an oldest to youngest sequence.

3.2.1 Set A

The type-A dykes consist of both aplite/pegmatite and granite dykes (Fig. 3.5), constantly striking NE-SW and dipping steeply toward SE (average: 151/73, dip direction/dip; Fig. 3.4a). Type A-dykes never exceed a width of a few tens of centimeters. They are commonly pervasively foliated, with the foliation delineated by biotite.

The type-A granite dykes are medium-grained and show a banded appearance defined by biotite-rich layers (cm-thick). These layers commonly localised the ductile deformation as evident from the displacement of younger dykes crosscutting the type-A dykes (Fig. 3.5c).

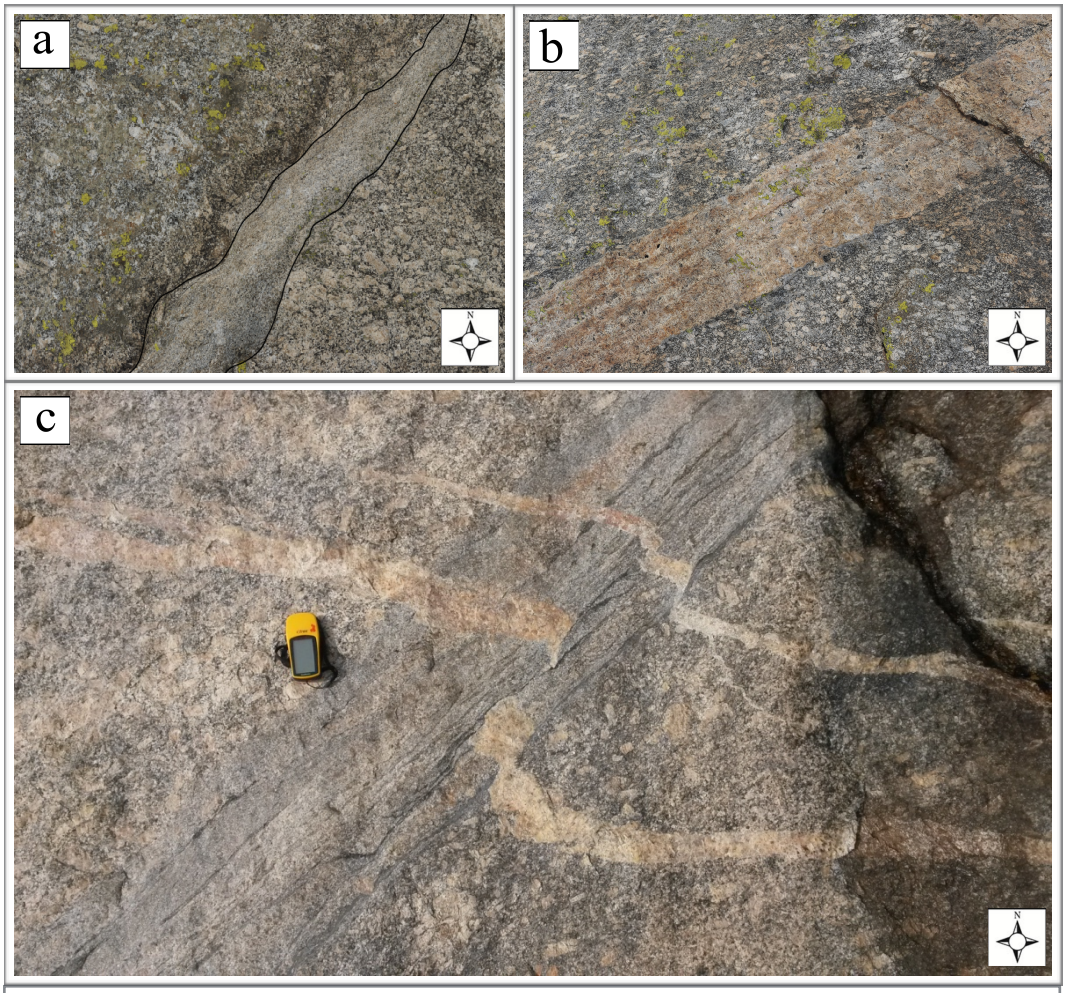


Figure 3.5 **a)** Typical appearance of the type-A granite dykes. The dyke boundaries, highlighted in black, are curved and irregular. **b)** A coarse-grained type-A pegmatite dyke. **c)** Biotite-rich layers within the type-A granite dykes are often reactivated as ductile shear zones, offsetting the crosscutting dykes.

The type-A pegmatites and aplites (Fig. 3.5b) mainly consist of a coarse to fine-grained assemblages of quartz, K-feldspar, plagioclase and biotite. Evolved pegmatites bearing other macroscopic accessory minerals (e.g. garnet, beryl and tourmaline) have not been observed.

The type-A dykes have commonly ‘evanescent’ (not sharp) boundaries; these boundaries can be locally irregular though the dykes maintain an overall constant orientation over tens to hundreds of metres (Fig. 3.5a,c).

3.2.2 Set B

Type-B dykes are fine-grained granite (microgranite) dykes (Fig. 3.6a,b), striking approximately E-W and variably (in the range from a few degrees to 60°) dipping toward the N (average: 001/40, dip direction/dip; Fig. 3.4b). They consists of fine-grained quartz, K-feldspar, plagioclase, biotite and muscovite. They are homogeneous in composition, but commonly foliated. These dykes can locally reach a width of a few metres, but most commonly are around 20-50 cm thick; the largests of them extend across the entire top of the valley (c.a 2 km). Type-B dykes sharply crosscut type-A dykes without exploiting these precursor structures.

3.2.3 Set C

Type-C dykes represent by far the main set of dykes in the Val dei Ratti area. They consist of pegmatite and aplite dykes, locally up to more than 1 m wide, striking consistently E-W, dipping northward with an angle of 20°-75° (average: 001/42, dip direction/dip; Fig. 3.4c). The orientation of this set of dykes is pretty much the same as the previous, but it can be clearly distinguished by the different lithology and because type-C dykes always cut through type-B dykes. They exploit the previous microgranite dykes and injects along the boundaries or at the core of the type-B dykes, the opposite never being observed in the studied area. The type-C dykes themselves are often reinjected at the core by other pegmatites or aplites of the same type.

Type-C pegmatites are richer in accessory minerals than the previous type-A: diffuse garnet and rare aquamarine beryl have been observed in the field. Garnet is commonly present in both aplites and pegmatites, and typically forms layers parallel to the boundaries of the dyke. Graphic garnet has also been observed in pegmatites. Aquamarine beryl is present in the most evolved facies of pegmatite dykes, where the grain size is coarser and the dykes show graphic textures of

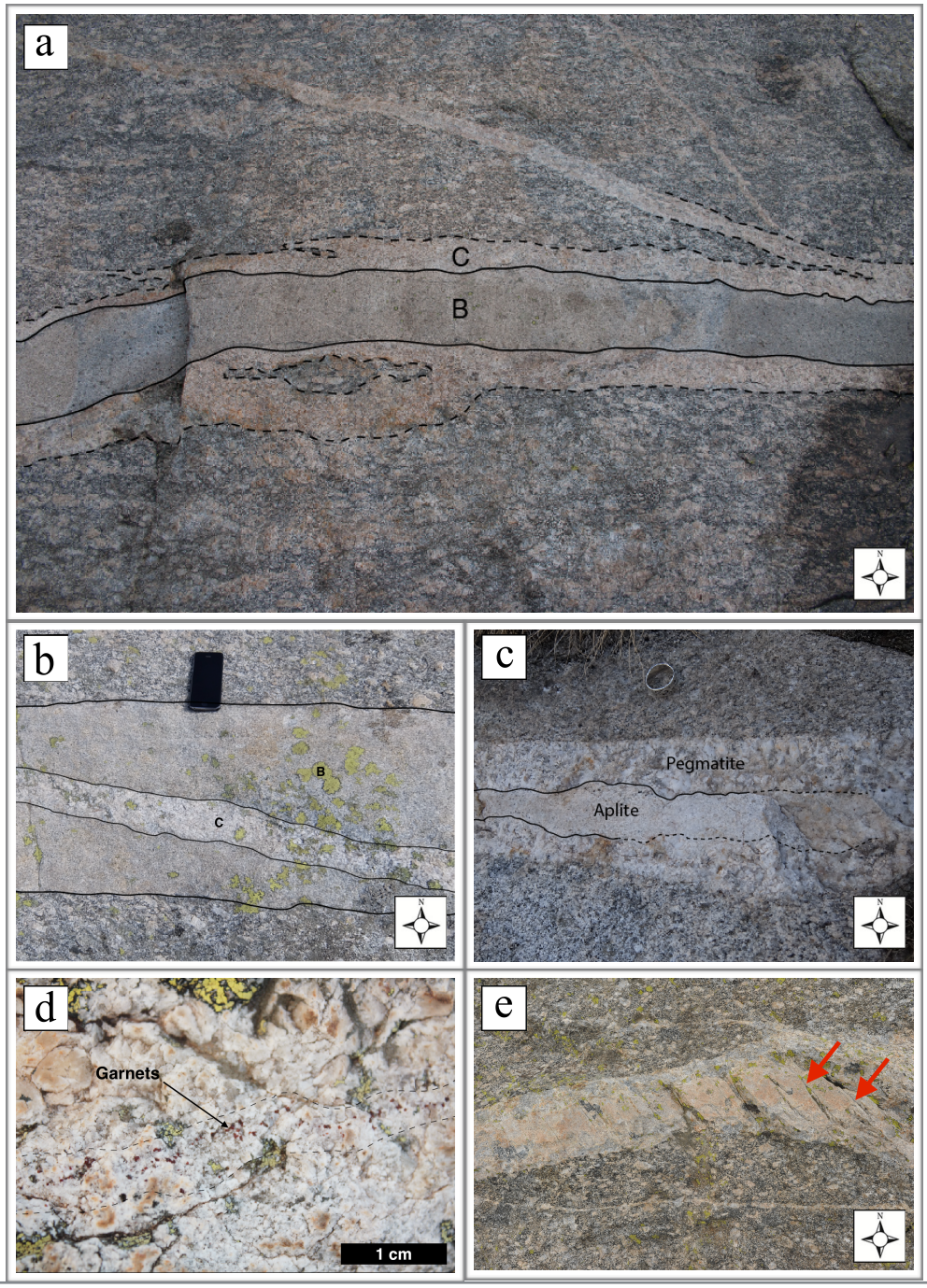


Figure 3.6 **a-b)** Type-C dykes (b) crosscut and (a) exploit the boundaries of the type-B microgranite dykes. **c)** A type-C dyke shows a roughly symmetric structure with aplitic core and pegmatitic borders. The pegmatite shows a graphic texture of quartz and feldspar. Ring for scale. **d)** A garnet-rich layer in a type-C pegmatite. Garnets generally do not exceed a few mm in size. **e)** A set of parallel fractures (red arrows) linking the borders of a type-C pegmatite dyke. This is a common feature in these dykes.

quartz and feldspars. In these portions of the dykes platy muscovite crystals can grow up to 3-4 cm.

Type-C dykes have commonly a composite structure due to the alternation of pegmatitic and aplitic portions (Fig. 3.6c). This can result in the development of a symmetric structure with aplitic centers and pegmatitic borders or vice versa, or, more commonly, in an asymmetric structure. However, in the pegmatitic portions the grain size is never very coarse, with quartz and feldspar crystals only locally coarser than a few centimeters.

As well as the previous sets, also type-C dykes are foliated. Commonly, these dykes contain a set of inclined fractures linking the boundaries (Fig. 3.6e). Fracture surfaces are decorated with chlorite.

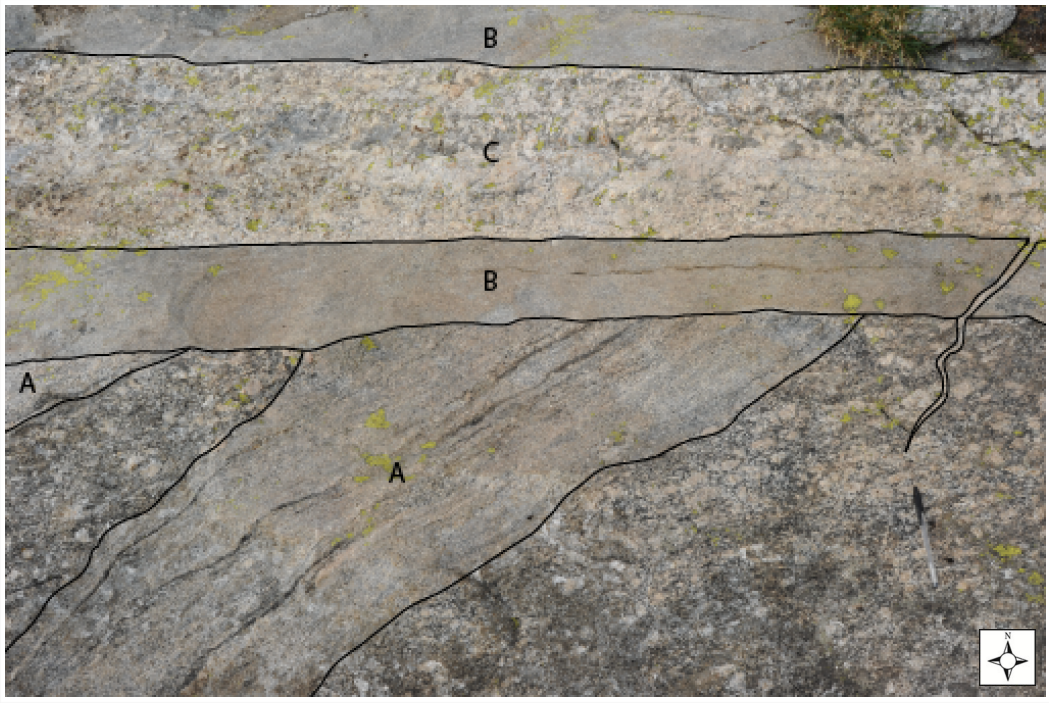


Figure 3.7 Crosscutting relationship between sets A, B and C. The type-C pegmatite exploits the core of the type-B microgranite. The injection vein of the type-C dyke into the host rock, visible in the right-hand side of the photo testify that the pegmatite is older than the microgranite. Type-A dykes show the typically layered appearance and are crosscut by all the other dykes. Pen (15 cm) for scale.

3.2.4 Set D

Type-D dykes are the youngest we have been able to observe in the studied area: aplite and pegmatite dykes striking N-S and almost vertical (average: 087/83, dip direction/dip; Fig. 3.4d). These dykes are less widespread than the previous, but they are easily distinguishable because of the different orientation and because they clearly cut through all the other dykes (Fig. 3.8b). They definitely close the sequence of dykes intrusions. In only few cases they exceed 20 cm in width (commonly 5-10 cm), but despite the limited thickness they are characterised by a remarkable continuity and regularity, being possible to follow the same dyke without interruption or change in orientation for hundreds of meters. Locally, they can consist of coplanar sets of en-echelon segments. The grain size is generally smaller than that of the E-W pegmatites, and generally aplitic texture prevails over pegmatitic. Both aplite and pegmatite dykes contain small (less than 1-2 mm) rounded garnets, generally arranged into planar layers. Aquamarine beryl has also been observed.
In some cases type-D dykes were intruded at their core by quartz veins that subsequently underwent a ductile deformation, developing a quartz mylonite that offset the crosscut dykes (Fig. 3.8a).

Although dykes with different orientation and field relationships are present in the studied area, the data are not solid enough to justify the definition of more sets. Nevertheless, observations and measurements show a strong consistency of orientations and mutual field relationships for the four sets described above.

3.2.5 Discussion

Orientations and relative age of these sets of dykes can be compared with those of the main set of dykes in the ‘Bodengo’ and ‘Codera’ areas as described in

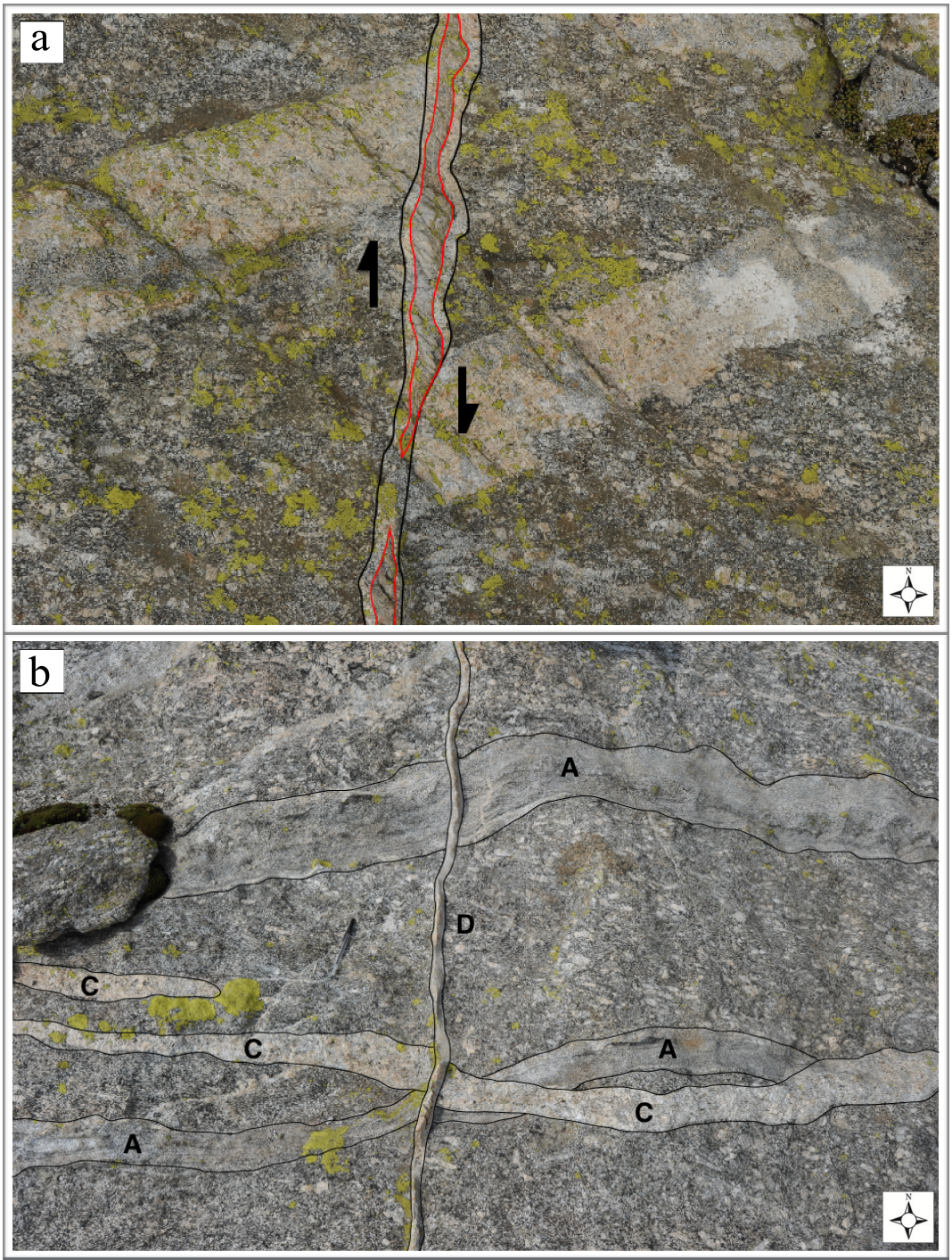


Figure 3.8 **a)** The type-D dyke shows a ductilely deformed quartz vein at its core, highlighted in red. The deformation along the quartz-mylonite results in a decimetric offset of a crosscut type-C dyke. **b)** General appearance of the type-D dykes: thin, aplitic dykes, that form a positive relief off the outcrop surface and sharply crosscut all the other dykes. Pen (15 cm) for scale.

Guastoni et al., 2014. The main set of pegmatites of the Bodengo area strikes approximately N-S and dips, from moderately to steeply, toward W to WNW. The dominant set of pegmatites in the Codera area is steeply dipping both toward north and south, with mean strike about 70° and it is crosscut by a set of microgranite dykes E-W striking and moderately dipping toward N. Codera pegmatites are older (28-25 Ma) and intruded before the emplacement of the Novate stockwork (24.0 ± 1.2 Ma; Liati et al. 2000), while Bodengo pegmatites are post-Novate (23-19 Ma).

Based on the orientation and the crosscutting relationships, we speculate that the main set of Codera pegmatites correspond to our set A, and the E-W trending set of microgranite dykes to our set B (Fig. 3.9). The younger Bodengo pegmatites have instead the same orientation and crosscutting relationships as our set D.

As already discussed by Guastoni et al. (2014) the fine-grained granite (the 'microgranite' of Guastoni et. al, and 'type-B granite' of this work) has characteristics similar to those of the Novate granite, that is described as a fine-grained, locally garnet-bearing, S-type two-mica peraluminous leucogranite (Liati

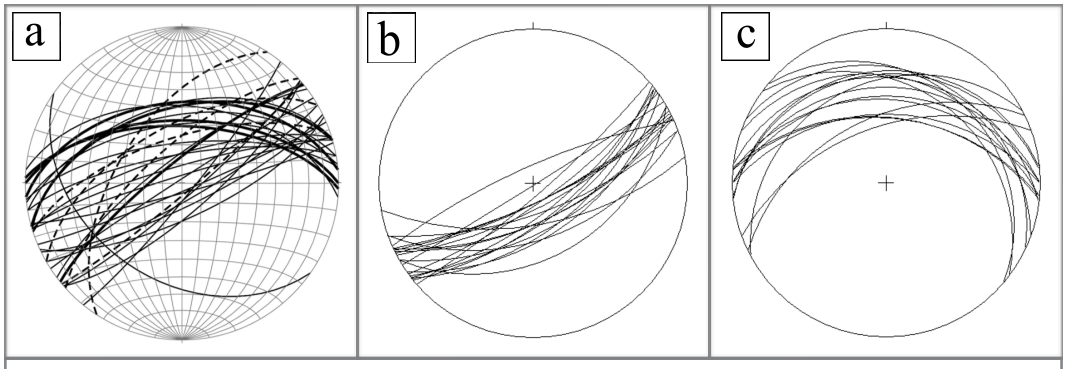


Figure 3.9 **a)** Stereographic plots (lower hemisphere, equal area) of the orientations of dykes and veins from the upper eastern Codera valley. The thin lines represent the main pegmatite set, thick lines are leucocratic (microgranite) dikes, and dashed lines indicate quartz veins. From Guastoni et al., (2014) **b-c)** Stereographic plots (lower hemisphere, equal area) of the orientations of set A (b) and set B (c) from the upper Val dei Ratti. Compare the orientation of the Codera main set of pegmatite dykes with the set A of the present work, and of

et al., 2000). The intrusion of set B could therefore be directly related to the emplacement of the Novate stockwork. If this is the case, set A should have intruded in the time span between 30 (emplacement of the Bergell pluton) and 23-25 Ma, and set D should be younger than 23-25 Ma. These ages would perfectly match the ages of the Codera and Bodengo pegmatites.

However, to prove this speculations, accurate dating of monazite from every set of dykes is needed.

3.3 Ductile deformation

3.3.1 Distributed and localised ductile deformation

To a first approximation, the studied area mainly consists of plutonic rocks with a preserved magmatic structure. However, a weak solid-state deformation fabric is present in both tonalite and granodiorite. Commonly the solid-state deformation exploited the magmatic foliation as indicated by the elongation of quartz grains along the magmatic foliation.

In addition to the pervasively distributed solid state overprint of the magmatic rocks, post-magmatic deformation also includes the development of localised ductile shear zones. These ductile shear zones exploited precursor (or pre-existing) planar heterogeneities that include:

i) joints/fractures;
ii) quartz veins;
iii) biotite-rich layers within granite dykes (Fig. 3.5c);
iv) mafic enclaves and melanocratic bands in the host rock (3.10b);
v) magmatic foliation of the host rock;
vi) mafic dykes (not described in this work, but occasionally observed).

The tonalite, that is finer grained than the granodiorite, is proner to deformation and shows peculiar features as small scale shear zones along joint-like structures

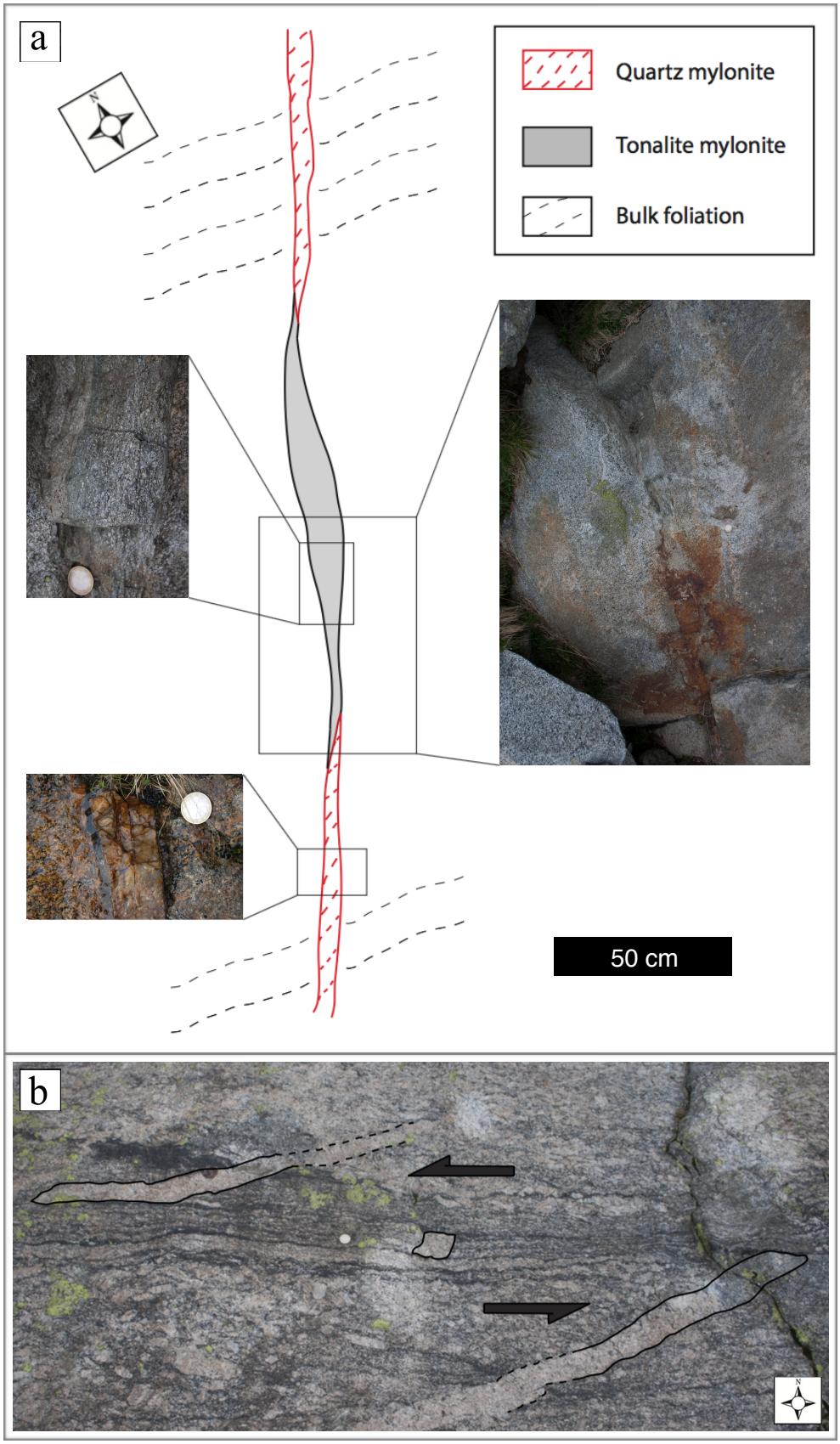

a
Quartz mylonite
Tonalite mylonite
Bulk foliation
50 cm
b

Figure 3.10 (previous page) **a)** Schematic map of an outcrop within the tonalite facies of the transition zone. Two left-stepping quartz-mylonites veins with sinistral fabric on the outcrop plane. The contractional stepover shows a gneissic mylonite, developed from the tonalite. The senses of shear given by the contractional stepover (dextral) and by the mylonitic fabric in the quartz vein (sinistral) are not consistent. 1 Euro coin for scale in all the photos. **b)** A leucocratic dyke is displaced along melanocratic bands parallel to the magmatic foliation of the host rock. 1 Euro coin for scale.

or on the stepover between en-echelon veins (3.10a). Locally, dykes trending N-S are dragged along the foliation of the host rock. Mafic enclaves and melanocratic bands are rich of relatively weak minerals, mainly biotite, and thus they represent perfect precursor for ductile deformation (3.10b). Generally, deformation features are more common and evident in the tonalite, but they are present in the coarser granodiorite too.

Differently to what can be seen in other plutons and other deformed metagranitoids, the pegmatite dykes do not look to have localised the deformation: neither they concentrated the deformation (e.g. Pennacchioni, 2005; Pennacchioni and Zucchi, 2012), nor they formed paired shear zones at their boundaries (e.g Pennacchioni and Mancktelow, 2007). This is also true for those dykes well oriented for shear reactivation, consistently with the inferred N-S regional shortening direction. However, consistently with several recent studies on the post-magmatic high temperature deformation in plutons (e.g Pennacchioni and Mancktelow, 2007), all the ductile shear zones in the Val dei Ratti area of the Bergell pluton seem to have exploited some pre-existing compositional or structural heterogeneities.

3.3.2 Ductilely deformed quartz veins

In the studied area (sheared) quartz veins and related joints/fractures form a steeply dipping, approximately NNE-SSW striking set of lineaments that crosscut

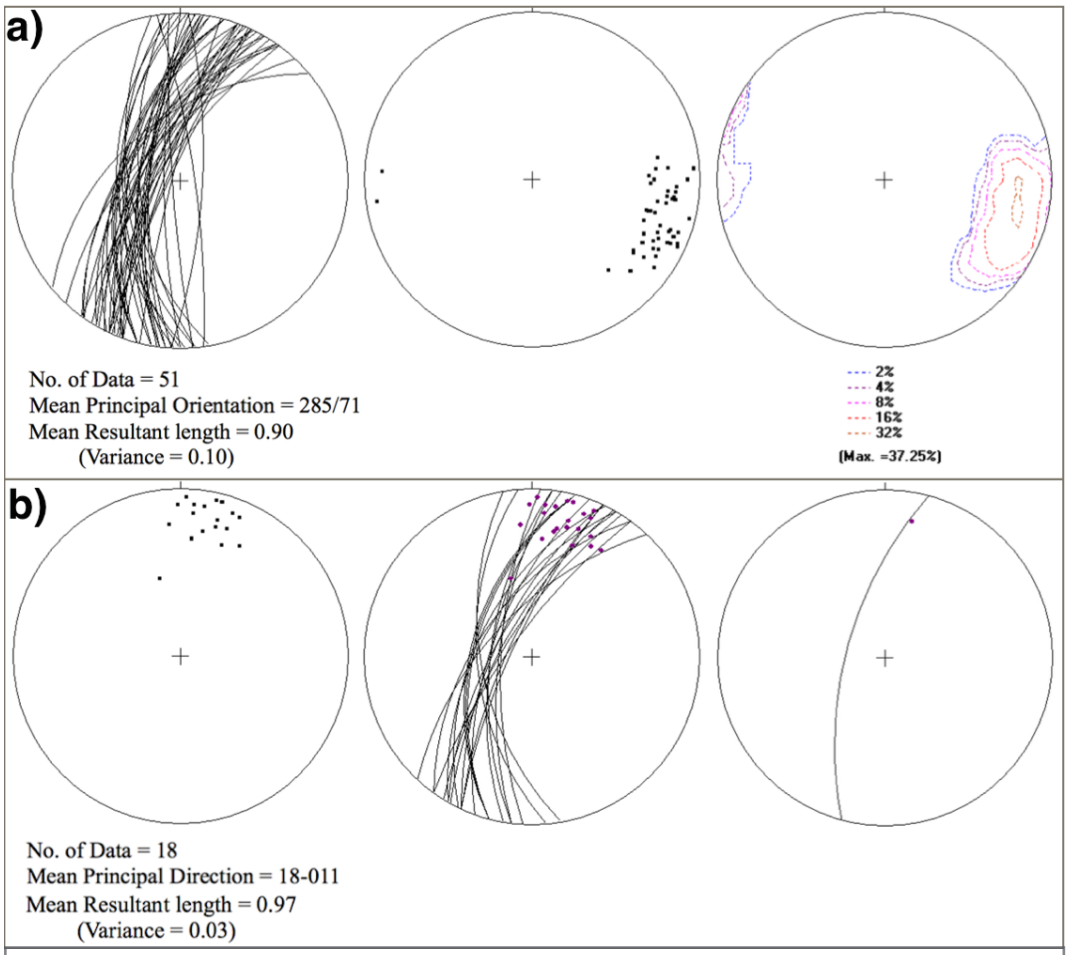


Figure 3.11 Stereographic plots (lower hemisphere, equal area) of the lineaments (joints, quartz veins, cataclasites) belonging to the set striking NNE-SSW. **a)** Orientation of all the lineaments. Data are plotted as planes in the left-hand column, and as poles to planes in the other two. **b)** Lineations measured on quartz vein and cataclasite surfaces. The right-hand plot shows the mean orientation of all the structural elements plotted as a plane and the mean direction of the lineation plotted as a line.

all the sets of dykes. This set has a narrow range of orientation, with a dip direction spanning between 260 and 320, but predominantly around 285 (average: 285/71, dip direction/dip; Fig. 3.11a). All the lineations, measured in the mylonitic quartz veins, are close to horizontal (average: 011/18, dip direction/dip; Fig. 3.11b). Based on that, we can infer that the kinematics of these steeply dipping shear zones is oblique, with a dominant strike-slip component.

The quartz veins decorate discontinuously the precursor fractures that locally show an en-echelon pattern (e.g. Fig. 3.14), with left-stepping geometries prevailing on right-stepping, even though both of them have been observed. In other cases, the veins are very continuous over distances of several metres (or tens of metres) and straight. Veins range form a millimetric scale up to a thickness of 15 centimetres or locally more. They are remarkably rich of pyrite, the oxidation of which lends a peculiar reddish colour to the quartzitic rock (Fig. 3.13a).

The fractures/veins locally do not show any macroscopic offset of crosscut markers. More commonly, however, they accommodated a sinistral sense of shear. In fact, in the large majority of the cases, the mylonitic foliation developed in the quartz veins, as can be seen on the outcrop plane, has a monoclinic asymmetry indicative of a left-lateral sense of shear (Fig. 3.13a). The shear zones are limited by the width, length and orientation of the quartz veins, and never extend into the host rock (Fig. 3.13a). Only in a few cases a dragging of the foliation along the border of the vein has been observed. A foliation is generally only developed at the contractional step over between overlapping en-echelon terminations of the veins (Fig. 3.10a; 3.16).

The sense of shear inferred from the orientation of the internal foliation of the quartz veins is locally contrasting with the observed separation of markers (e.g. pegmatite dykes) on the outcrop surface. In some cases, the sinistral shear zone vein is associated with dextral separation of the markers; in other cases there is

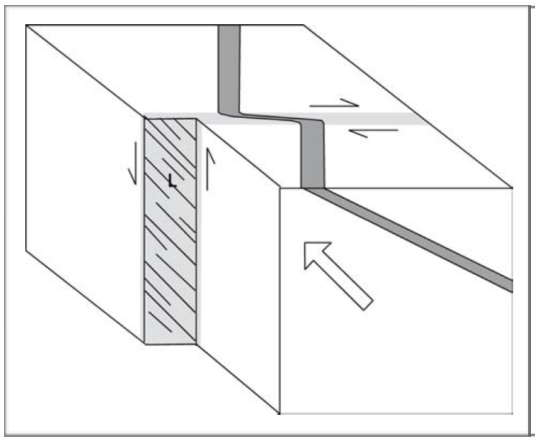


Figure 3.12 Schematic presentation of a shear zone illustrating how deflection of a marker can give the wrong sense of shear if not used in a section parallel to the movement direction; the frontal block moves up and to the left, but the deflected layer indicates an apparent sinistral displacement on a horizontal surface. From Passchier and Trouw (2005).

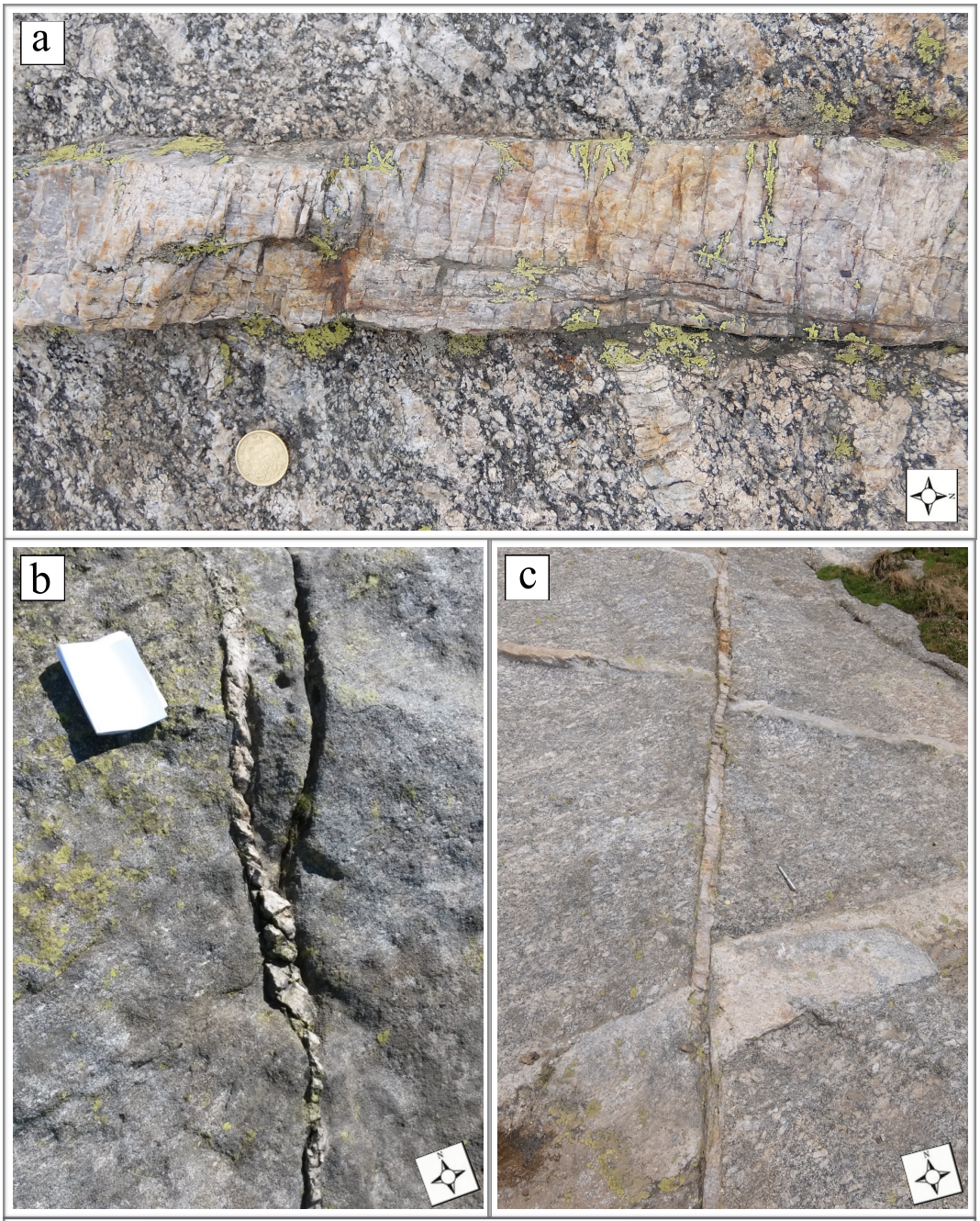


Figure 3.13 **a)** Detail of a quartz mylonite. The oblique foliation indicates a sinistral sense of shear, deformation doesn't propagate in the host rock. Red spots result from the oxidation of pyrite crystals. **b)** Pull-apart structure along a quartz vein indicates a sinistral sense of shear. **c)** Non consistent separation of pegmatite dykes along a mylonitic quartz veins.

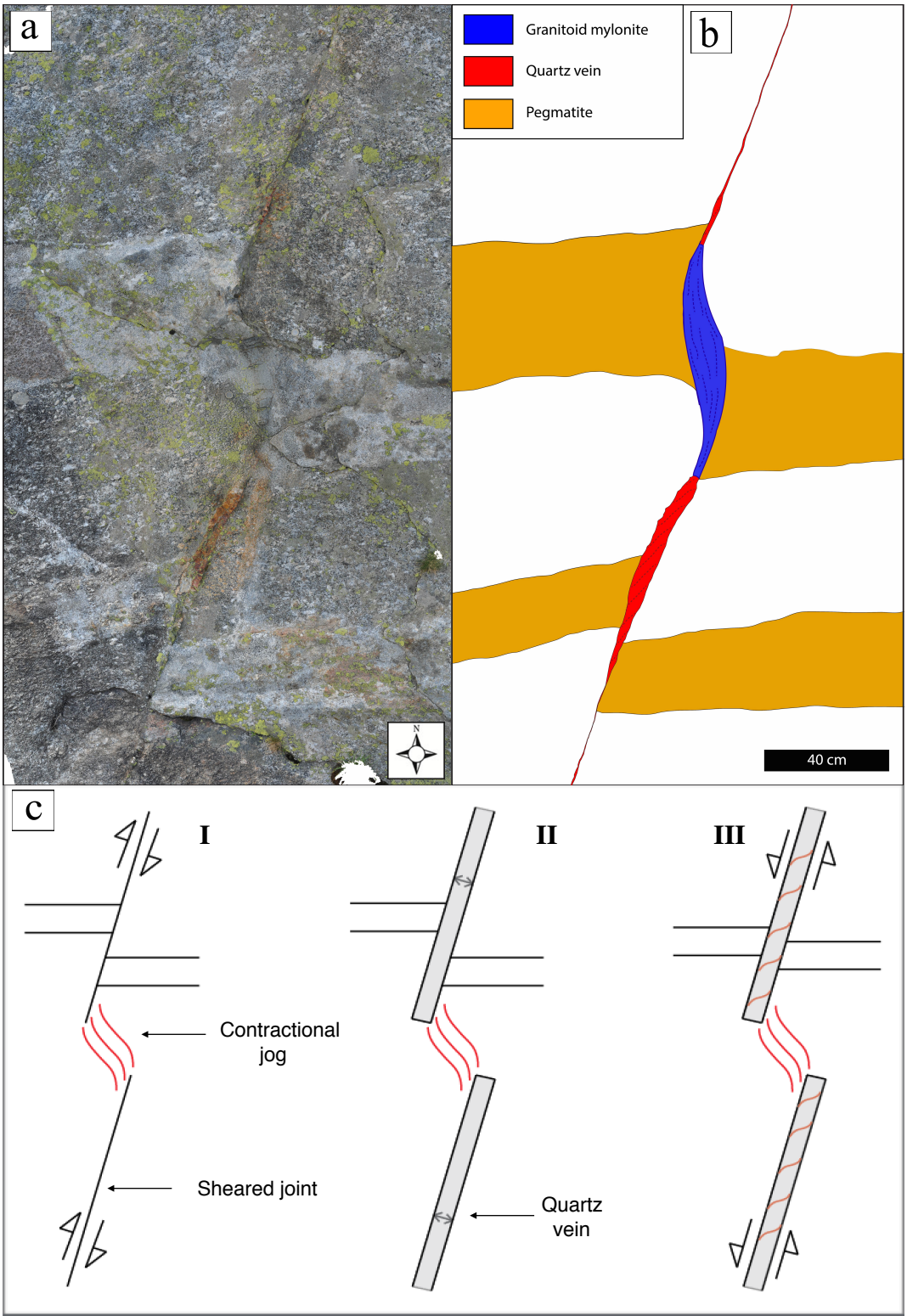


Figure 3.14 **a-b)** Photomosaic and map surface of the outcrop in figure 3.11c. **c)** Schematic diagram of a possible hypothetical sequence of events that can lead to this structure. Description in the text.

even a contrasting separation (either dextral and sinistral) of different dykes crosscut by the same sheared vein (Fig. 3.13c). This discrepancy between marker separation and the sense of shear inferred from the mylonitic microstructure of the vein, can be explained in some cases by a cut effect of the marker/shear zones so that the separation actually does not reflect the real offset. However, this explanation does not apparently holds for the case of relatively steeply dipping crosscut dykes, considering the relatively flat attitude of the outcrops and the shallowly plunging lineation of the quartz mylonites. In fact, wrong sense of shear indicators can develop only if the dip of the dyke is lower than the plunge of the lineation (Fig. 3.12). Furthermore, in at least two cases, a contractional jog has been observed at the contractional stepover between left-stepping segments of the veins (Fig. 3.10a; 3.14), while dilational jogs with pull-apart structure have been observed at the stepover between right stepping segments of the veins (Fig. 3.19).

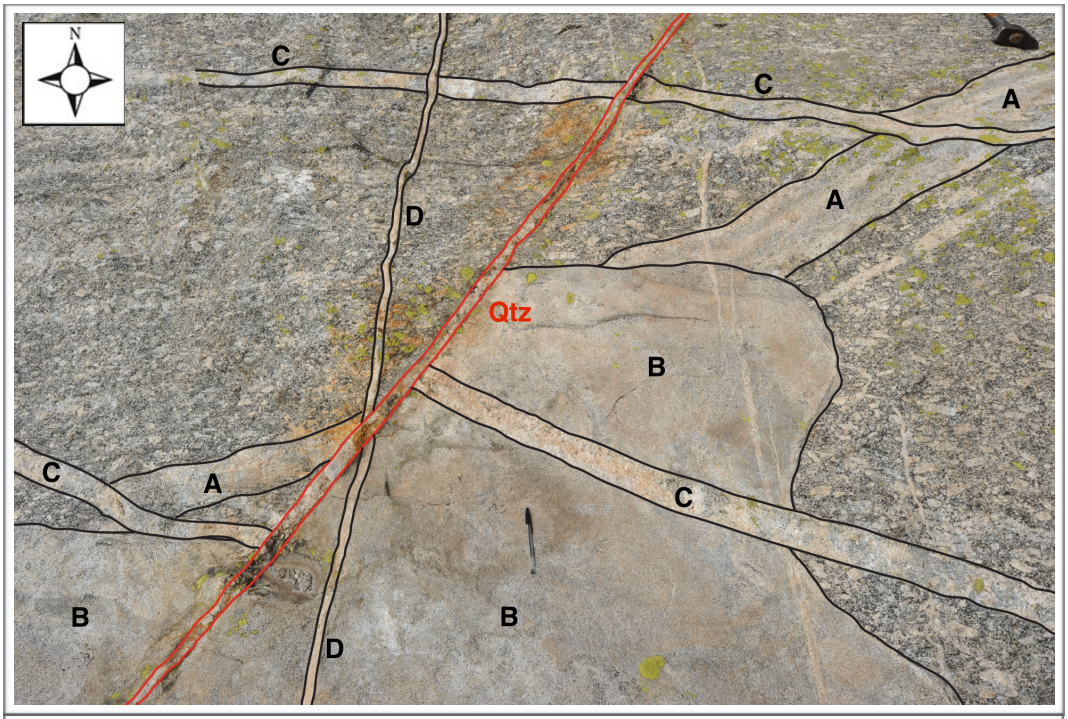


Figure 3.15 This outstanding outcrop shows the crosscutting relationships among the four sets of dykes, that are crosscut and displaced by a sinistral mylonitic quartz vein.

These are sound kinematic indicators of dextral sense of shear along the veins/ fractures.

In order to explain these features we need to consider the eventuality of a change in kinematics of these structures during the deformation. In figure 3.14c a hypothetical conceptual model of evolution of these structures is shown. In stage I joints form in response to thermal stresses and dextral slip nucleation along left-stepping joints leads to the development of contractional jogs. In stage II quartz precipitates in dilational regions along the sheared joints and in stage III it accomodates a sinistral shear at temperatures probably higher than 500°C (see chapter 6.3.3) producing quartz mylonites.

3.4 Brittle deformation

The sheared quartz veins are overprinted by late veins filled with chlorite, quartz and/or epidote (3.16). These veins are generally not more than a few millimetres in thickness and they often are located at the border or even crosscut the quartz veins. No alteration halo surrounds the veins, differently from what has been observed by other authors in similar geological settings (e.g. Pennacchioni & Mancktelow, 2007). These veins are reactivated by cataclasites.

On the fracture surface, that shows a dark green color due to the abundance of chlorite and/or epidote, a very clear lineation is commonly visible (Fig. 3.16c). These lineations have the same orientation than the lineations in the quartz mylonites, meaning that the kinematics has not changed in the time span between the last ductile deformation and the brittle reactivation (Fig. 3.11b).

The only shear sense indicator that can be observed for the chlorite-epidote faults is the dislocation of the crosscut dykes that in our few observations is always sinistral. In one case the geometry of a wing-crack at the tip of the fracture is consistent with a sinistral sense of shear (Fig. 3.16a).

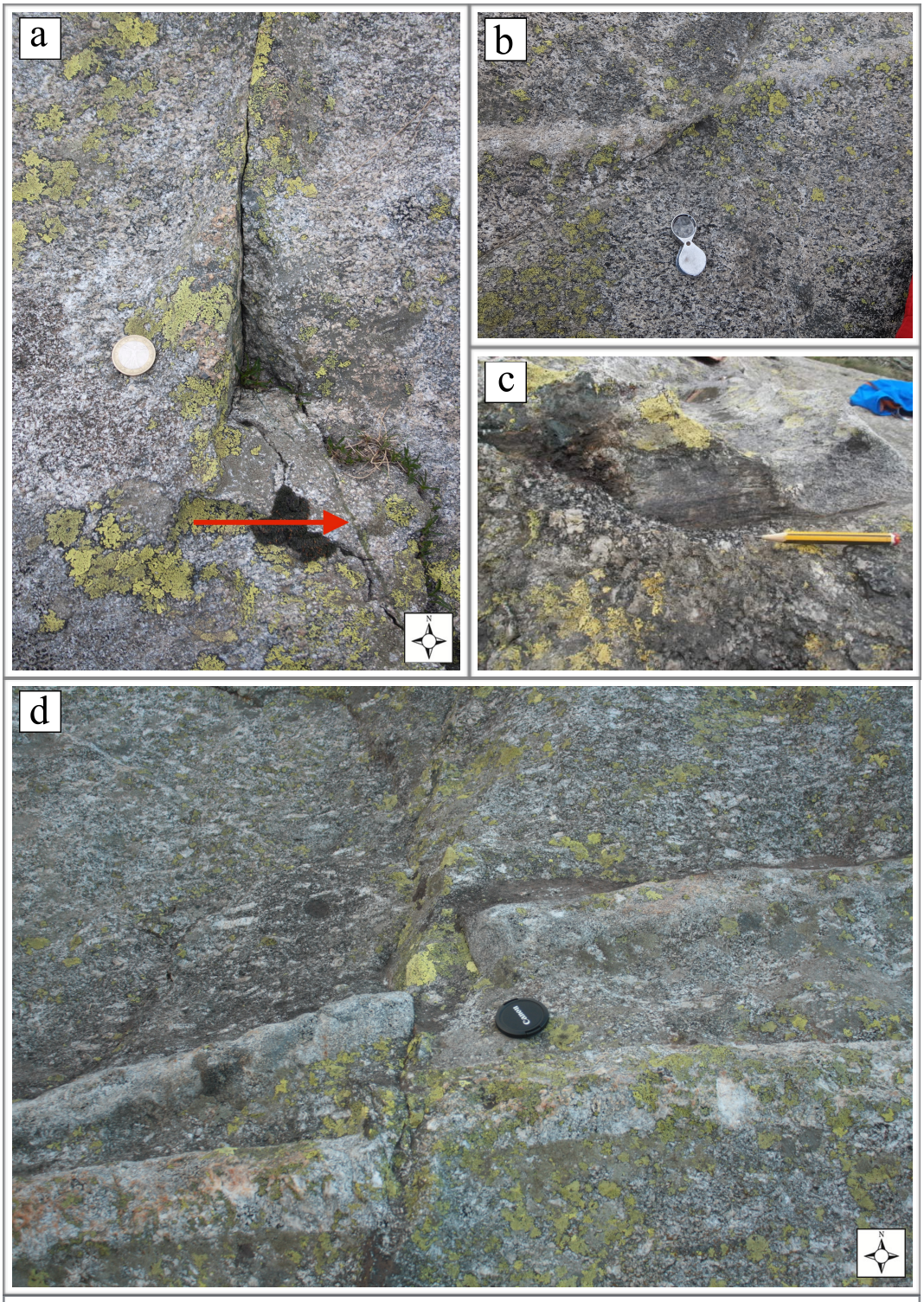


Figure 3.16 **a)** Shear fracture with a wing-crack (indicated by the red arrow) filled with chlorite and/or epidote. The orientation of the wing-crack suggests a sinistral sense of shear on the shear fracture. **b)** A leucocratic dyke displaced sinistrally along a chlorite-epidote vein. **c)** Detail of the fracture plane shown in d). The fracture surface is decorated with chlorite and show a clear strike-slip lineation. **d)** Two dykes displaced sinistrally along a brittle fault plane.

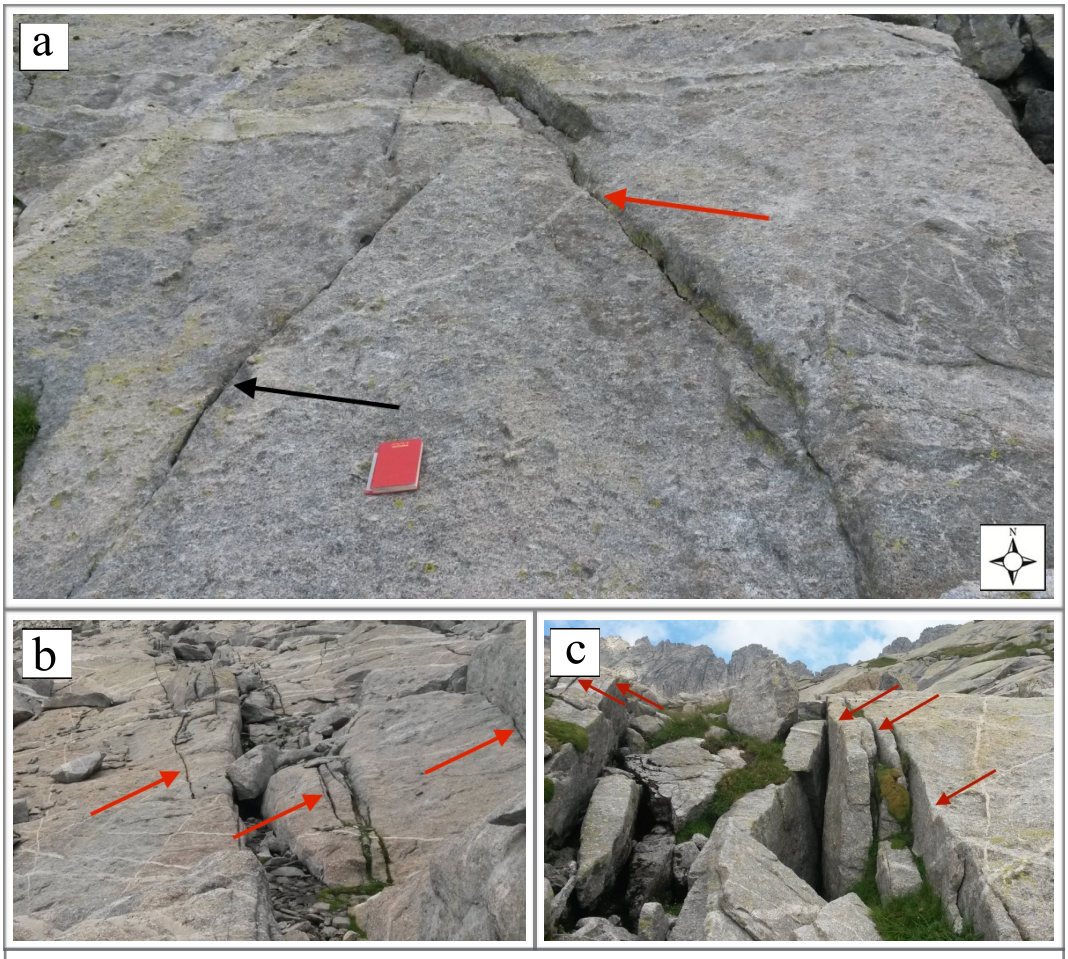


Figure 3.17 **a)** The black arrow indicates a NE-SW striking fracture (orientation corresponding to the quartz-filled fractures) that crosscuts and slightly displaces sinistrally the thin leucocratic dyke. The NW-SE striking joint (red arrow) crosscut all the other objects without showing any displacement. **b-c)** NW-SE striking joints are indicated by the red arrows. These lineaments are dominant in the uppermost part of the valley.

In the Val dei Ratti area, a second set of lineaments (in addition to the fracture set corresponding to the quartz-filled fractures) is already visible from satellite images (Fig. 3.18). This set strikes NW-SE (average: 224/73, dip direction/dip) and is dominant in the upper part of the valley. These lineaments correspond to steeply-dipping joints free of any quartz or epidote vein filling. They crosscut all the sets of dykes and the fracture set decorated by the quartz veins (Fig. 3.17).

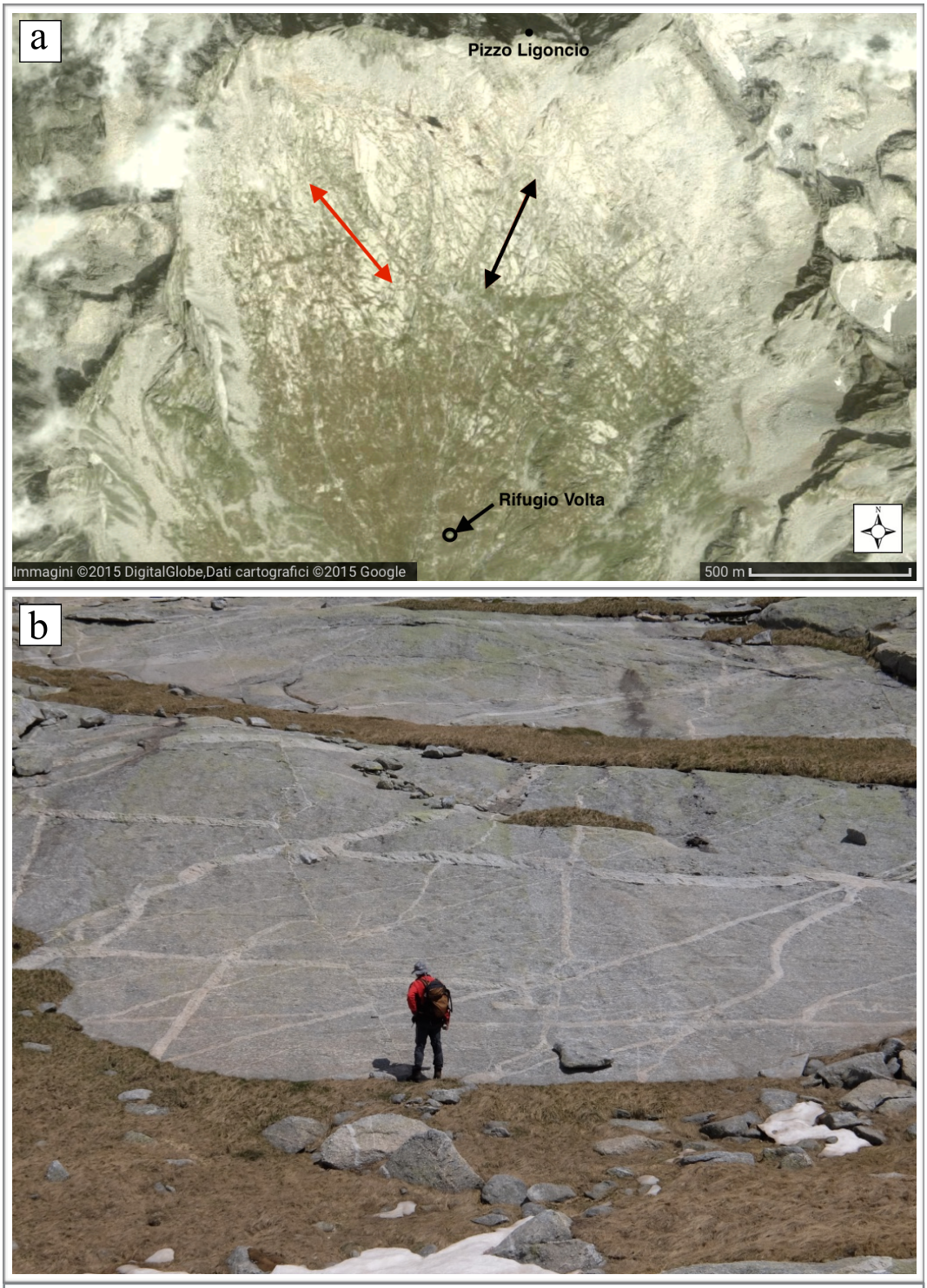


Figure 3.18 **a)** Google Earth image of the upper Val dei Ratti area. The black double arrow indicates the older set of joints, fractures and quartz veins, while the red one the younger set of joints that crosscuts the quartz veins. **b)** The outstanding granodiorite outcrop whose partial photomosaic is shown in figure 3.18. G.P. for scale.

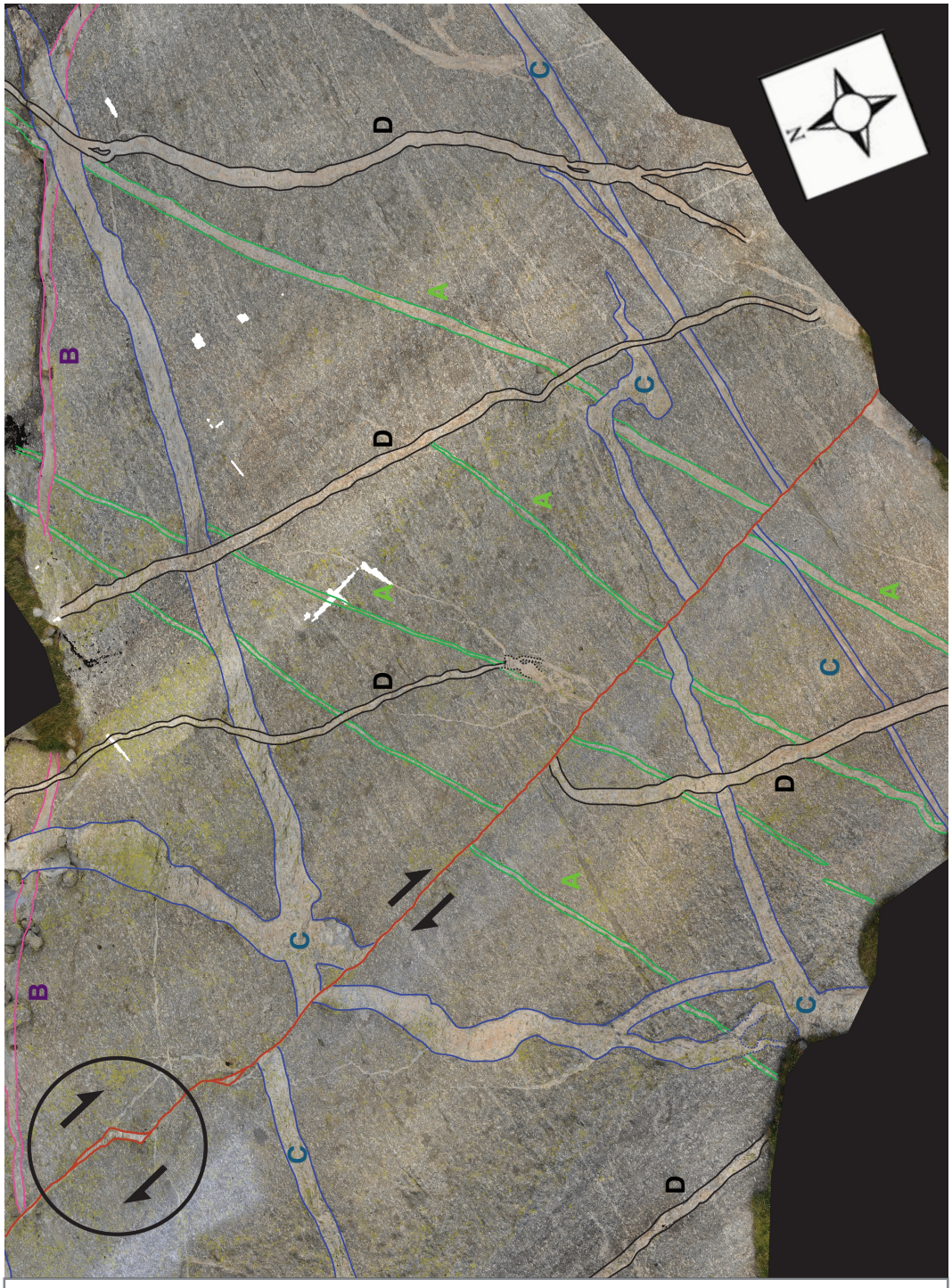


Figure 3.19 Photomosaic assembled by photogrammetry of a glacier-polished outcrop showing the four sets of dykes (different colours) and a deformed quartz vein (in red) crosscutting the dykes. The black circle highlights a pull-apart structure along the vein indicating a dextral sense of shear.

4. PETROGRAPHY OF SAMPLED DYKES

Pegmatite and granite dykes were sampled in three different sites, corresponding to the code number 21 (Gps coordinates: N 46°13’52,8”, E 9°32’20,5”), 24 (N 46°13’49,6”, E 9°32’12,3”) and 25. The term pegmatite is here used *sensu lato*, and refers to leucocratic dykes with either aplitic or pegmatitic textures. Sampling sites 21 and 24 were selected because all the four sets of dykes crop out, and their crosscutting relationships are clear and consistent. At these two sites at least one sample for each set of dykes was collected. As already described in the previous chapters, set A comprises both granite and pegmatite dykes, so we took at least a sample for both of them. At site 25 we collected an extra sample from set D. The list of sampled dykes and corresponding label codes (year, site and progressive letter) is reported in table 4.1.

SET	ROCK TYPE	YEAR	SITE	LETTER
A	GRANITE	15	21	D
	PEGMATITE	15	21	C
	PEGMATITE	15	24	A
B	GRANITE	15	21	B
	GRANITE	15	24	B
C	PEGMATITE	15	21	E
	PEGMATITE	15	24	C
D	PEGMATITE	15	21	A
	PEGMATITE	15	24	D
	PEGMATITE	15	25	D

Table 4.1 List of the sampled dykes.

4.1 Petrographic description

Optical and scanning electron microscopy (SEM) analysis of samples listed in table 4.1 were carried out on polished thin sections cut parallel to the strike of the dykes and orthogonal to the dyke boundaries.

4.1.1 Pegmatite dykes

Type-A pegmatite (samples 15-21C and 15-24A) mainly shows a fine-grained aplitic texture with local domains in which the grain size can reach up to 1 cm. It mainly consists of quartz, K-feldspar, plagioclase and minor biotite, almost completely altered in chlorite. The most abundant accessory minerals are apatite, titanite and allanite, the latter commonly shows a coronitic texture with epidote overgrowth (Fig. 4.1a). This pegmatite lacks garnet, and muscovite is very scarce. SEM-BSE imaging shows that this pegmatite is relatively rich of small (generally about 10-20 microns) monazite-(Ce) crystals (Fig. 4.2a,b,c). Zircon and apatite are relatively abundant and commonly associated with monazite (Fig. 4.2a,b,c). The main opaque minerals are magnetite and hematite. Thorite is rare (Fig. 4.2d). Domains with relatively large crystals locally show well developed micrographic textures of quartz and K-feldspar (Fig. 4.1f).

Type-C (samples 15-21E and 15-24C) and type-D (samples 15-21A, 15-24D and 15-25D) pegmatite dykes, show very similar petrographic features. They are distinguished in the field because of their orientation, though. Quartz, K-feldspar and plagioclase make up the most of the rock; biotite (completely altered in chlorite and rutile needles) and muscovite are scarce. Garnet is small (c.a 1-2 mm), and subhedral (Fig. 4.1b); small individuals often gathered in small areas or are aligned along planar layers and show a weak pinkish colour in thin section. In sample 15-25D garnet shows a strong colour zonation with reddish cores and

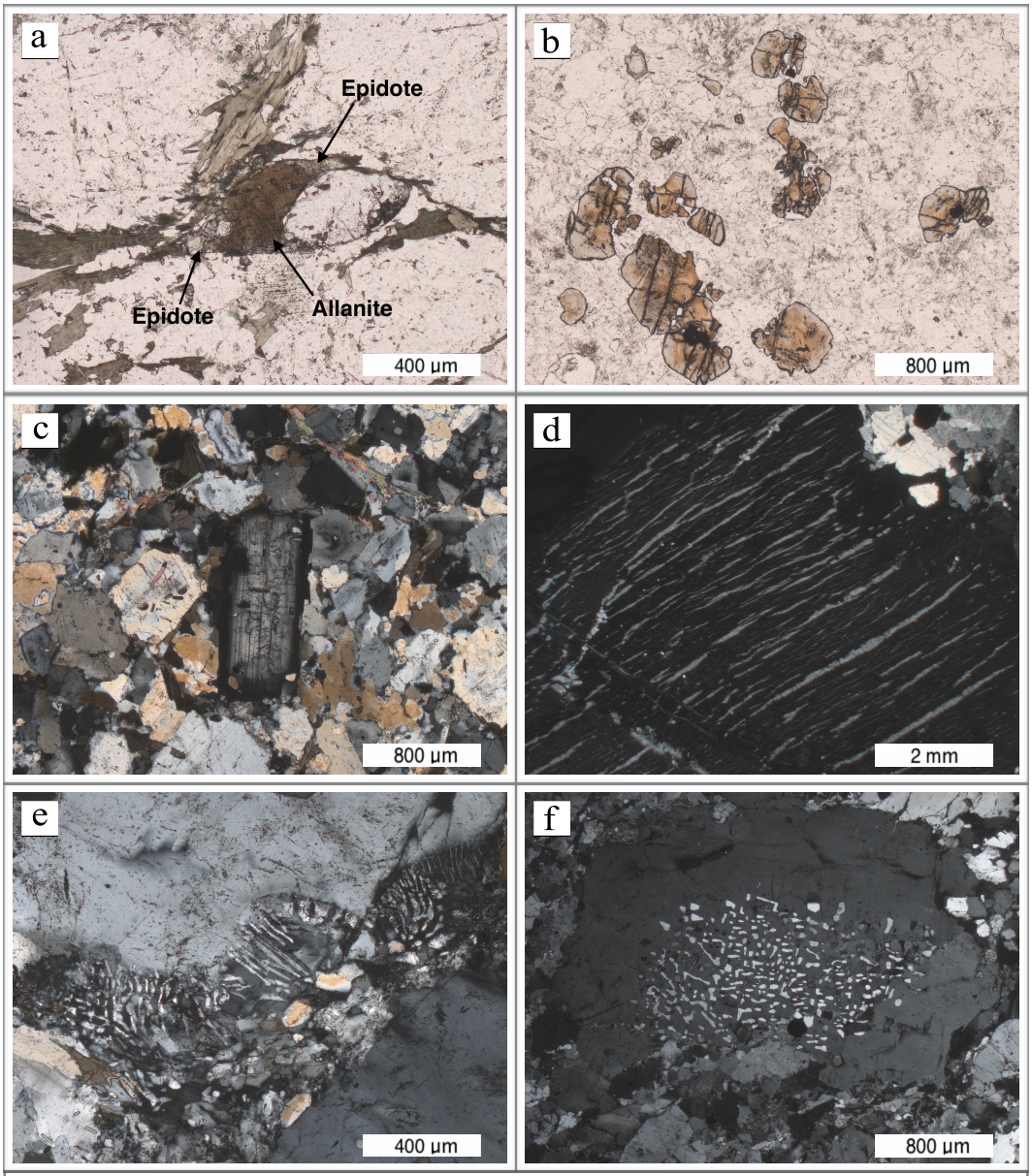
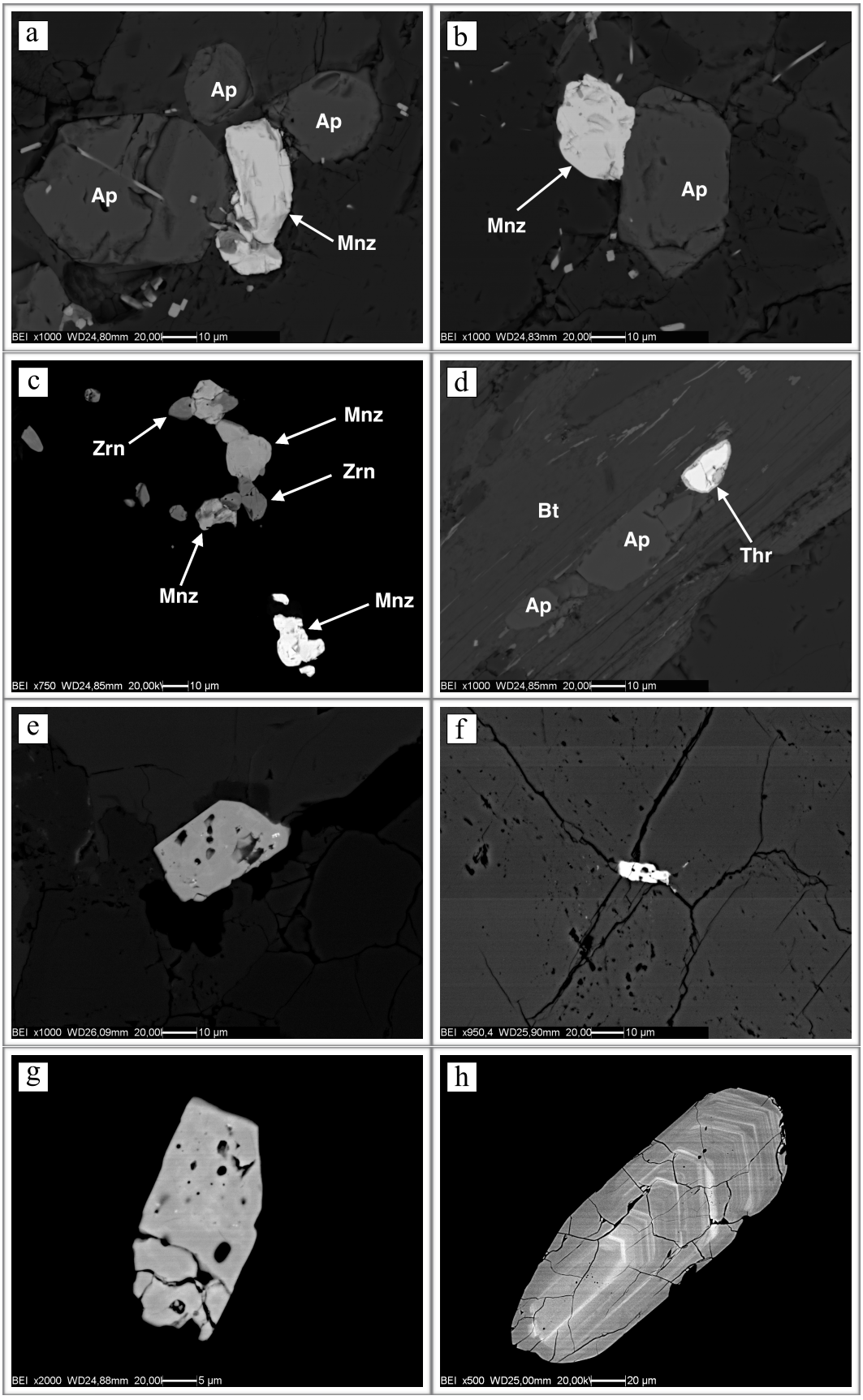


Figure 4.1 **a-f)** Microphotographs of selected minerals and textures in the pegmatite and granite dykes. **a-b)** taken under plane polarised light, **c-f)** with crossed polars. Description of the microphotographs in the text.

Figure 4.2 (next page) Highly contrasted SEM-BSE images. **a-b)** Subhedral monazite-(Ce) crystals (Mnz) surrounded by euhedral apatite (Ap) crystals (sample 15-21C). **c)** Intergrowth of several anhedral monazite-(Ce) and zircon (Zrn) crystals (sample 15-21C). **d)** A thorite crystal (Thr) showing a reaction rim, included in biotite (sample 15-21C). **e-g)** Pecilitic zircon crystals (the brightest ones). Samples are respectively 15-21C, 15-21A and 15-24C. **h)** Large and euhedral zircon crystal showing an outstanding growth zonation, in the granodioritic host rock.


a
Ap
Ap
Ap
Mnz
BEI x1000 WD24,80mm 20,00 10 µm
b
Mnz
Ap
BEI x1000 WD24,83mm 20,00 10 µm
c
Zrn
Mnz
Zrn
Mnz
Mnz
BEI x750 WD24,85mm 20,00k 10 µm
d
Bt
Ap
Thr
Ap
BEI x1000 WD24,85mm 20,00 10 µm
e
BEI x1000 WD26,09mm 20,00 10 µm
f
BEI x950,4 WD25,90mm 20,00 10 µm
g
BEI x2000 WD24,88mm 20,00 5 µm
h
BEI x500 WD25,00mm 20,00k 20 µm

pinkish to colourless rims (Fig. 4.1b). Zircon is not abundant and is often found in the vicinity of biotite. Zircon is very small (normally less than 10 microns, occasionally up to 25-30 μm) and shows a pecilitic texture (Fig. 4.2f,g), locally defined by thorite inclusions. In the host rock (granodiorite), zircon is way larger (more than 100-200 μm), euhedral, and show a well-developed growth zonation (Fig.4.2h). Among opaque minerals magnetite is the most abundant, but also hematite and ilmenite are present. Apatite is scarce, and no allanite was observed. Monazite-(Ce) is rare and very small (generally less than 10 μm), and is often associated with zircon and thorite. Thorite, columbite-(Mn), uraninite, aeschynite-(Y) and U-phosphates were detected by means of SEM-BSE imaging combined with EDS analysis. Aquamarine beryl, observed in the field in both type-C and type-D pegmatite dykes, was not found in thin section, possibly because the thin sections were prepared from portions of the dykes with a rather small grain size.
The sampled dykes are characterised by an alternation of aplitic and pegmatitic texture, with grain size up to 2 cm in the coarsest portions. Sample 15·21A shows a well-developed comb texture at the boundary of the dyke, with crystals that locally show micrographic texture. Large (up to 2 cm) K-feldspar crystals commonly show microperthitic texture (Fig. 4.1d).

The main mineralogical difference between the two types of pegmatite is thus the presence of allanite in the older ones and the presence of garnet and beryl in the younger ones.

4.1.2 Granite dykes

The type-A granite dyke (15-21D) have a mineral assemblage similar to that of the A-type pegmatite. The main differences are that allanite crystals of the granite are bigger, zircon is very abundant, commonly euhedral and can reach up to 150

μm in size and biotite is much more abundant. Grain size is generally coarser than that of the type-B granites (Fig. 4.3). Texture is characterised by large (up to 5-10 mm), euhedral and undeformed crystals of perthitic K-feldspar, typically showing tartan gemination, and plagioclase. The matrix is made of quartz aggregates, typically showing pervasive grain size reduction. Myrmekites are common at the rim of K-feldspar.

Type-B granite consist of fine grained two-micas granites with hypidiomorphic granular texture. Plagioclase is generally euhedral and zoned (Fig. 4.1c). K-feldspar, which shows local myrmekitic rims (Fig. 4.1e) is euhedral/subhedral, zoned, only locally perthitic and very often shows epitaxial growth of secondary muscovite. Biotite is generally fresh, with only minor chloritisation. Muscovite is both primary and secondary (alteration of feldspars). Other abundant accessory

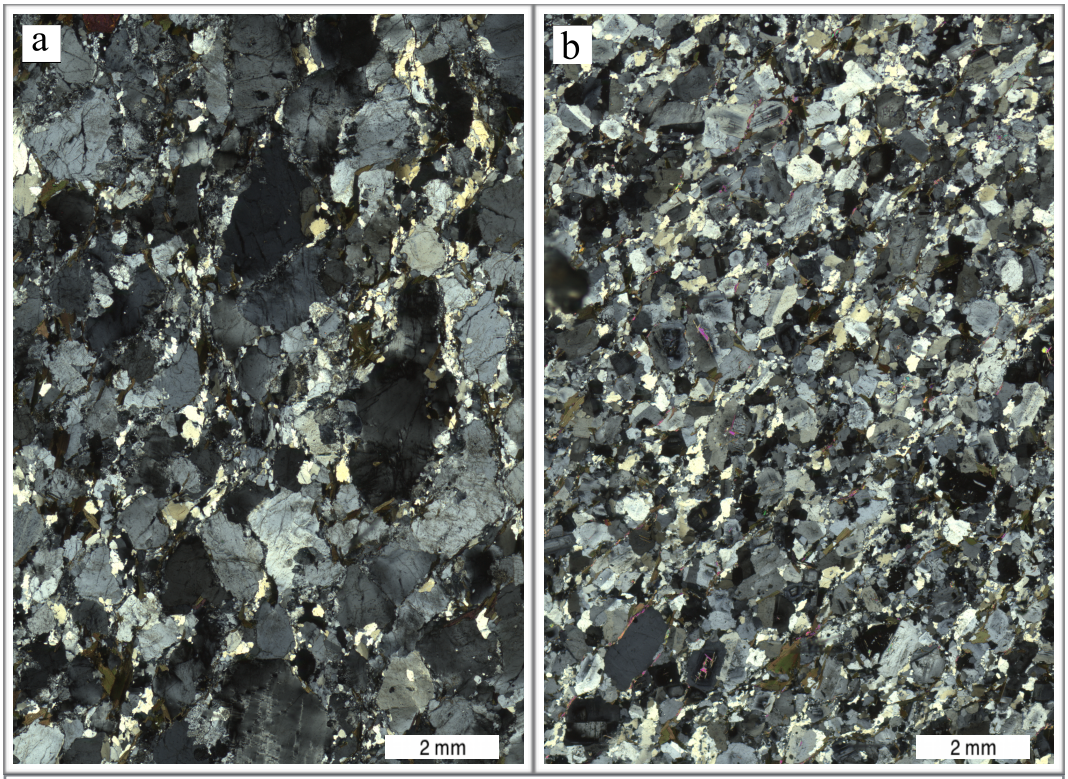


Figure 4.3 Comparison between the texture of the type-A granite (**a**) and the type-B granite (**b**), at the same scale.

minerals are apatite, epidote and zircon. Myrmekites along feldspar rims are locally present (Fig. 4.1e).

The main difference between the two types of granite is textural. Grain size of type-A granite, in fact, is coarser than that of the type-B ones (Fig. 4.3).

4.2 Separation of minerals for dating

The final aim of the sampling was dating the different dykes whose relative sequence of emplacement was established in the field. Because of the lack of time, the dating of the dykes has not been carried out yet. However, preliminary work for dating has been performed during the thesis with separation of monazite, apatite and zircon from all the samples listed above.

In order to separate the minerals, we used the following procedure:

i) crushing and sieving of the rock samples to obtain a granular material with a grain size of less than 200 μm;
ii) washing of the samples with denatured water to eliminate the lightest clay portion;
iii) sieving of the washed sample in four granulometric classes (<63 μm - 60<μm<100 - 100<μm<160 - 160<μm<200) of which the two intermediate classes have later been used for separation;
iv) gravity separation by preferential flotation using a solution of sodium polytungstate (SPT) with a density of 2,98 g/cm^3;
v) separation of ferromagnetic minerals (i.e. magnetite) with a magnet;
vi) magnetic separation of diamagnetic minerals (e.g. apatite, zircon and monazite) from paramagnetic minerals (e.g. garnet) with a Frantz Magnetic Separator;
vii) hand picking of monazite, zircon and apatite crystals.

In figure 4.4 are shown, for example, two individuals of monazite-(Ce) separated from sample 15-24D (Type-D pegmatite). The crystals are subhedral to anhedral and generally intergrown with other undetected minerals. Besides Ce, this monazite contains relevant amounts of La, Nd and Th. Monazite will be used for U-Th-Pb dating of each set of dykes.

Zircon and apatite instead, have been separated in order to obtain cooling ages with methods such as the fission tracks or the U-Th/He geochronology.

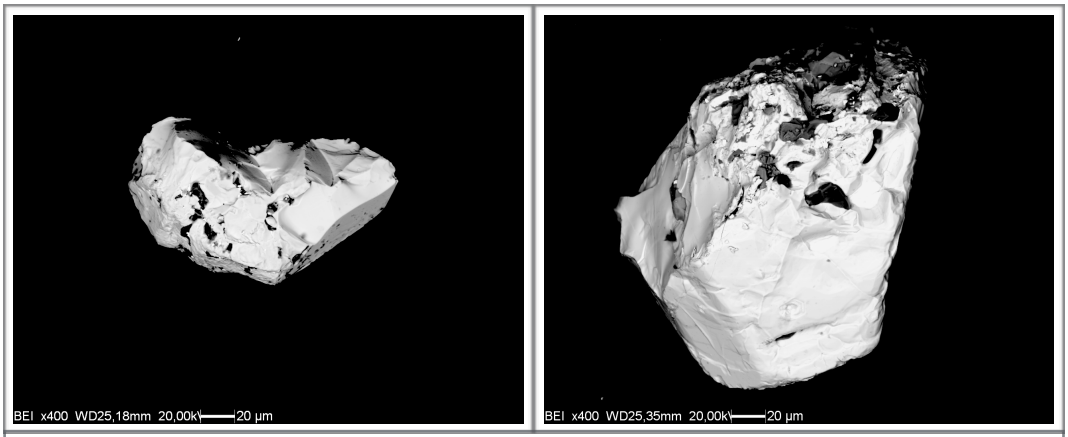


Figure 4.4 SEM-BSE images of two monazite-(Ce) crystals separated from sample 15-24D

5. GEOCHEMISTRY OF SAMPLED DYKES

5.1 Geochemical characterisation

XRF chemical analysis (see analytic techniques) of major and selected trace elements is reported in Tab. 5.1 and illustrated in variation and classification diagrams. Bulk chemical analysis of pegmatites can be troublesome when the grain size is very coarse, so we selected homogeneous fine-grained portions of the dykes. Based on chemical composition and mineral content, a classification of pegmatite dykes is attempted.

5.1.1 Silica vs oxide Harker variation diagrams

Silica vs oxide variation diagrams of figure 5.1 show that type-A and type-B granite dykes have similar SiO_2 contents (68-69 wt.%), however type-A granite has higher TiO_2, Fe_2O_3, MgO, K_2O and P_2O_5 and lower Na_2O, Al_2O_3 and CaO. Granite of both sets can be distinguished from all pegmatites by their lower SiO_2 and higher TiO_2, Fe_2O_3, MgO and Al_2O_3 contents, indicating a lower degree of evolution.

Type-C and type-D pegmatites are similar, although type-C one has lower SiO_2 and MnO contents and higher K_2O content. In particular, the enrichment in MnO of type-D pegmatite is strong and most likely due to the abundance of spessartine-rich garnet in this pegmatite. Type-C and type-D pegmatites are distinguished from type-A pegmatite for their lower TiO_2, MgO and CaO contents and their generally higher MnO content. Type-D pegmatite can have an higher P_2O_5 content than granites, though P_2O_5 should generally decrease with increasing silica, because some P_2O_5 is retained in almandine-spessartine garnet (Guastoni, 2012).

	SET A			SET B		SET C		SET D		
	GRA	PEG	PEG	GRA	GRA	PEG	PEG	PEG	PEG	PEG
	15.21D	15.21C	15.24A	15.21B	15.24B	15.21E	15.24C	15.21A	15.24D	15.25D
SiO_2	67,99	74,63	75,17	68,97	68,98	73,68	72,47	74,58	73,97	74,28
TiO_2	0,35	0,06	0,14	0,30	0,26	0,02	0,01	0,01	0,01	0,02
Al_2O_3	15,61	13,99	13,87	17,16	16,83	14,03	14,65	14,39	14,26	14,22
Fe_2O_3	2,89	0,70	1,09	2,01	1,82	0,57	0,62	0,65	0,69	0,61
MnO	0,04	0,02	0,02	0,04	0,07	0,02	0,09	0,30	0,17	0,26
MgO	1,05	0,15	0,29	0,79	0,67	0,06	0,06	0,05	0,06	0,07
CaO	1,55	1,25	1,57	3,30	3,03	0,60	0,56	0,36	0,50	0,62
Na_2O	2,38	3,02	3,22	4,69	5,24	3,06	4,77	4,60	3,85	4,86
K_2O	7,68	5,95	4,86	2,32	2,20	7,01	5,79	5,07	6,06	4,18
P_2O_5	0,25	0,07	0,08	0,12	0,10	0,06	0,09	0,13	0,11	0,06
Tot	99,79	99,84	100,31	99,70	99,20	99,11	99,11	100,14	99,68	99,18
L.O.I.	*0,50*	*0,34*	*0,29*	*0,58*	*0,41*	*0,25*	*0,19*	*0,29*	*0,23*	*0,17*
S	*18*	*<10*	*<10*	*<10*	*15*	*<10*	*<10*	*<10*	*<10*	*<10*
Sc	7	8	9	<5	<5	11	<5	<5	10	7
V	29	7	8	22	16	6	<5	<5	<5	6
Cr	<6	<6	<6	7	<6	<6	<6	12	<6	<6
Co	9	9	9	9	9	5	8	11	14	9
Ni	<3	<3	10	57	<3	<3	<3	12	4	3
Cu	21	25	36	18	23	18	25	19	202	15
Zn	57	19	24	51	61	12	16	18	28	17
Ga	25	22	21	22	25	28	28	26	23	28
Rb	228	139	128	93	128	206	231	289	291	233
Sr	379	111	213	506	442	42	32	14	39	23
Y	14	11	10	10	11	10	7	7	6	15
Zr	269	40	84	148	128	33	36	36	36	37
Nb	<3	3	5	5	11	18	17	21	<3	12
Ba	1814	161	613	494	495	75	35	24	98	24
La	145	11	20	17	17	<10	12	<10	21	10
Ce	284	35	71	47	54	22	14	12	14	<10
Nd	13	24	<10	16	10	26	35	30	14	26
Pb	52	48	53	31	42	43	45	27	36	31
Th	35	3	5	4	<3	3	<3	6	<3	5
U	6	9	11	<3	4	<3	<3	11	42	9
ASI	1,06	1,03	1,04	1,07	1,03	1,03	0,98	1,06	1,04	1,05
AI	1,28	1,23	1,31	1,68	1,53	1,11	1,04	1,10	1,11	1,14

Table 5.1 XRF bulk chemical analysis. Major and minor elements are expressed in wt. % as oxides, while trace elements in ppm as elements. ASI (Alumina Saturation Index) and AI (Alkalinity Index) calculated as explained in the text.

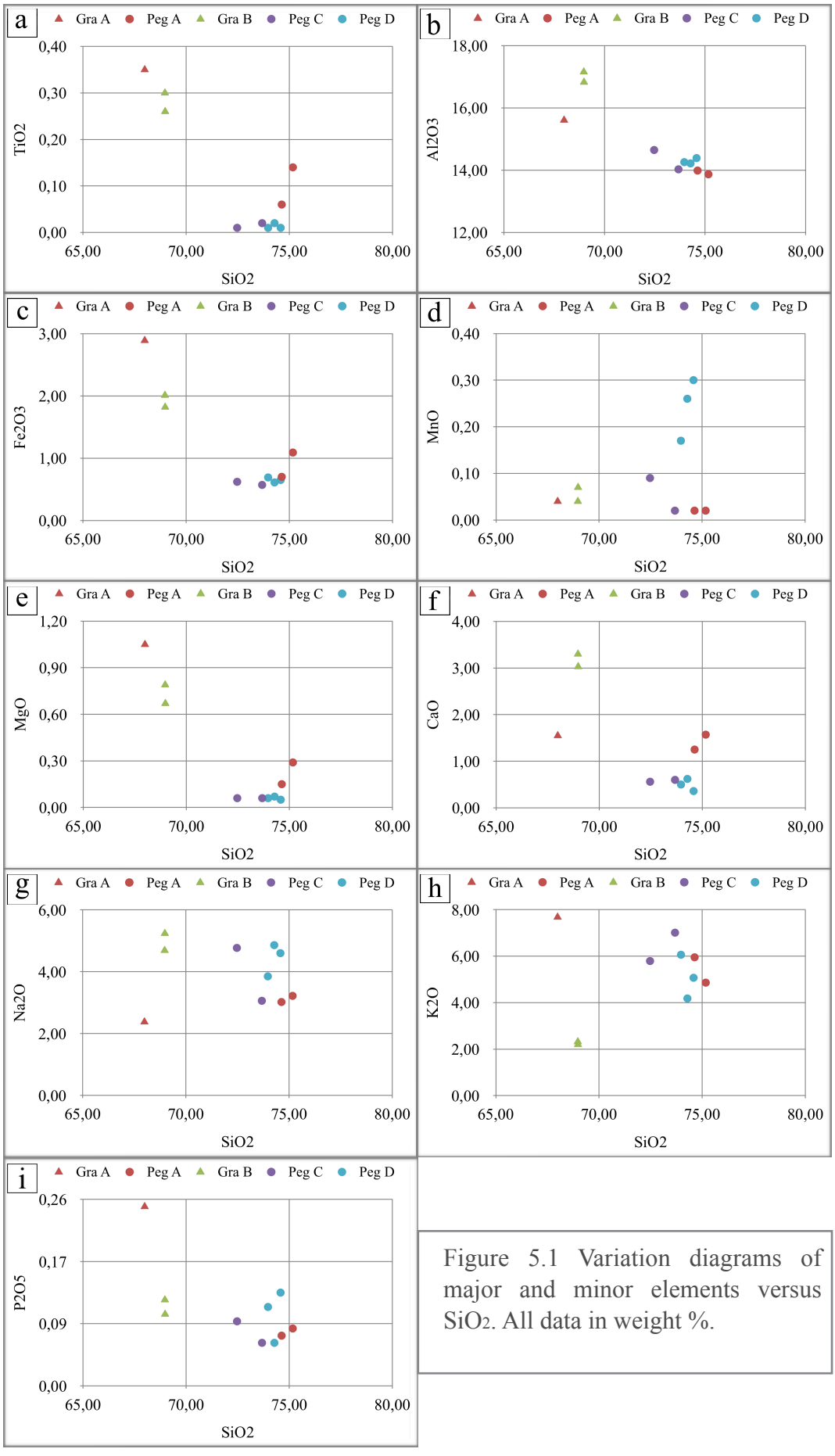


Figure 5.1 Variation diagrams of major and minor elements versus SiO_2. All data in weight %.

We observe that the differences in bulk chemical composition among pegmatites and granites of the same type is negligible in both major and trace elements and pegmatites and granites of different types appear to show slightly distinct chemical characters.

5.1.2 AFM diagram and classification of granitoids

Several classification diagrams has been used to better characterise the rocks. In the AFM ternary diagram, our granites and pegmatites plot in the field of calc-alkaline rocks (Fig. 5.2). They define a trend with granitoids plotting in a single cluster toward the alkali (A) apex and pegmatites plotting further down, showing the strongest alkali enrichment.

In figure 5.3c all the compositions are plotted in a variation of the TAS diagram proposed by Cox et al. (1979) and adopted by Wilson (1989) for plutonic rocks.

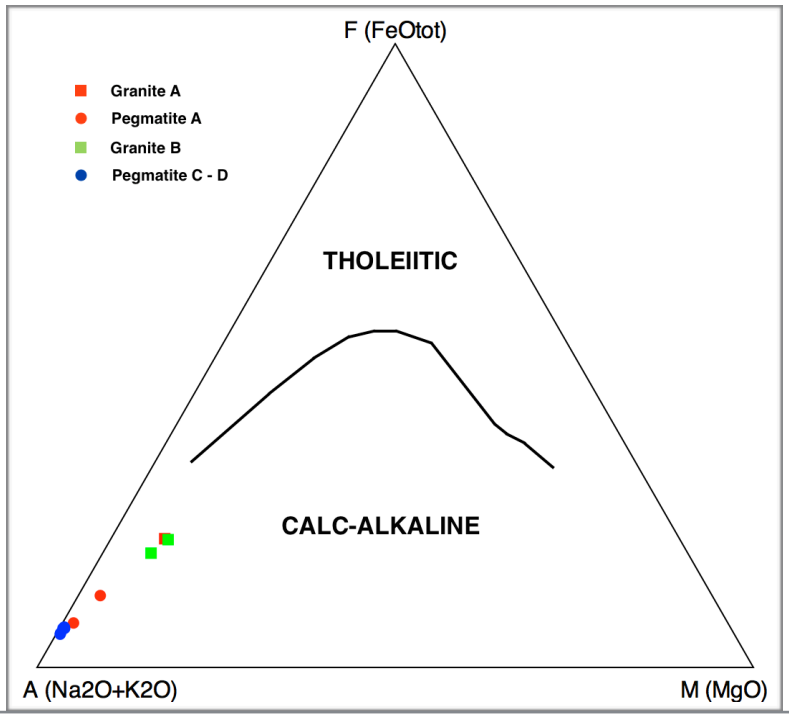


Figure 5.2 AFM diagram. Line separating fields of tholeiitic and calc-alkaline suits after Irvine and Barragar, 1971, Figure 2.

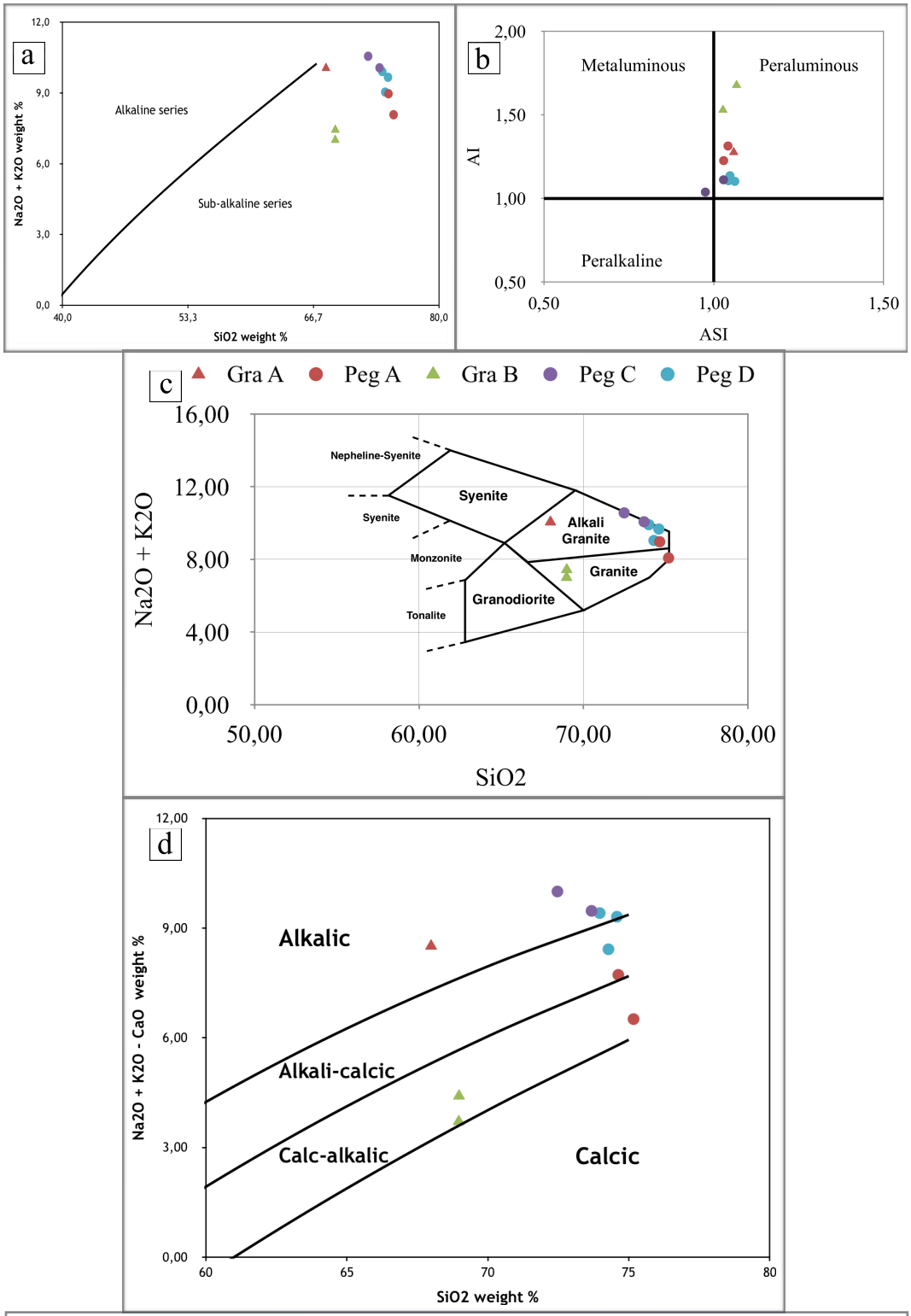


Figure 5.3 Classification diagrams for granitoid rocks. See detailed description in the text.

Type-B granite falls in the 'granite' field, type-A granite and type-C and D pegmatites are richer in alkali and fall in the 'alkali-granite' field, whilst type-A pegmatite falls in between. In this nomenclature the word 'alkali' refers to the abundance of alkali-feldspars in the granite and does not mean that the rock belongs to an 'alkaline serie'. In fact, the alkali vs silica diagram, as proposed by Irvine and Barragar (1971) (Fig. 5.3a), shows that all the rocks fall in the 'sub-alkaline series' field of the diagram. Alkalies saturation is also measured by the Alkali Index (**AI**), defined as the molecular ratio $Al_2O_3/(Na_2O+K_2O)$. Peralkaline rocks have an **AI** < 1, but, as shown in figure 5.3b , all the analysed samples have **AI** > 1.

The Alumina Saturation Index (**ASI**) is defined by Frost et al. (2001) as the molecular ratio $Al_2O_3/(CaO-1{,}67*P_2O_5+Na_2O+K_2O)$. In alumina-oversaturated or peraluminous rocks, excess alumina is accomodated in micas, especially muscovite, and in aluminous accessory minerals (e.g. almandine-spessartine garnet, tourmaline) (Best, 2003). All the analysed rocks, with the only exception of sample 15-24C, have an **ASI** slightly higher than 1, and thus are classified as peraluminous rocks (Fig. 5.3b). All these rocks contain a variable amount of muscovite. High **ASI** values are typical of peraluminous and Ca-poor liquids derived from metapelites. S-type granite magmas derived from the incipient partial melting of metapelites, if equilibrium is attained during melting, should be strongly peraluminous (ASI = 1.3–1.4) (Holtz et al., 1992; Wolf and London, 1995; Patiño Douce, 1996). Our samples however, have an **ASI** only slightly higher than 1, ranging from 1,03 to 1,07.

The Modified Alkali-Lime Index (**MALI**) vs silica diagram has been proposed by Frost et al. (2008), together with the **AI**/**ASI** diagram (Fig. 5.3b), for the classification of granitoid rocks. The **MALI** is calculated as (Na_2O+K_2O-CaO) in weight percent (Frost et al., 2001). As we have already seen there is a huge difference in alkali content between type-A and type-B granites: the first one falls in the alkalic field, whereas the second ones are calc-alkalic (Fig. 5.3d). The term

calc-alkalic describes suites of rocks that show moderate enrichment in calcium over alkalis (Peacock 1931) and has nothing to do with the definition of a calc-alkaline suite. The type-C and D pegmatites have the highest **MALI**, and plot in the alkalic field with the exception of one sample; type-A pegmatites can be distinguished by their lower **MALI** and plot between the alkali-calcic and calc-alkalic field.

In conclusion we can summarise all these observations into the following points:

i) all the sampled dykes have a granitic composition, are subalkaline, belong to the calc-alkaline serie and are slightly peraluminous (with the only exception of sample 15-24C, that is metaluminous);
ii) type-A granite and type-C and D pegmatites are enriched in alkali, whereas type-A pegmatite and type-B granite show an enrichment in calcium over alkalis;
iii) pegmatites are depleted in Ti, Al, Fe, Mg and Ca with respect to granites;
iv) type-D pegmatite is significantly enriched in MnO.

5.1.3 Trace elements

In the 'spider diagram' of figure 5.4 the content of several trace elements, normalised to the chondrite data from McDonough and Sun (1995), have been plotted. These elements belong to the LILE (Sr, Pb, Ba, Rb), HFSE (P, Nb,Ti, Zr, Th, U), LREE (La, Ce, Nd) and HREE (Y) groups of incompatible elements. Both granites and pegmatites are strongly enriched in the most incompatible elements, that tend to partition in the magma during the magmatic fractionation. Highly compatible, strongly depleted, elements as V, Cr, Co, Ni, Cu, Zn have not been plotted whatsoever.

The diagram shows that type-C and type-D pegmatites are enriched in Rb, and depleted in Ba and Sr with respect to all the other samples. This behaviour will be explained by the following diagrams as an indicator of a higher degree of

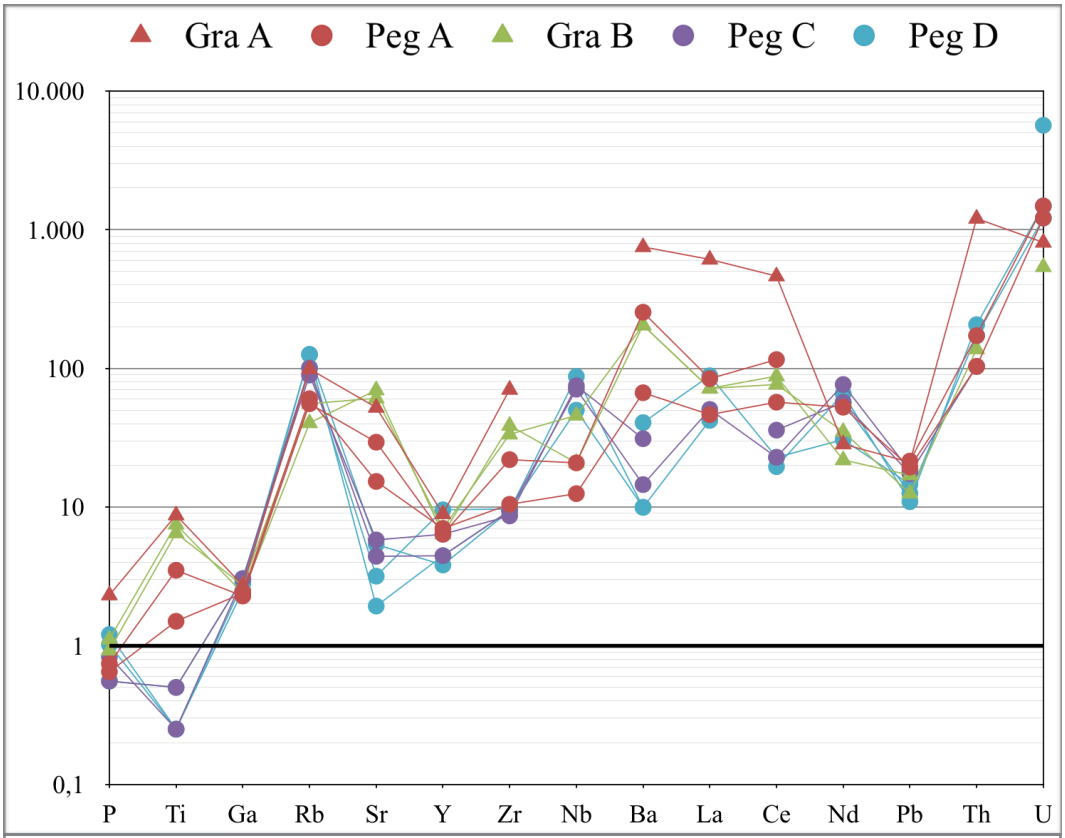


Figure 5.4 'Spider diagram' showing trace elements of bulk pegmatites and granitoids versus chondrite. Chondrite data after McDonough and Sun (1995).

evolution. Furthermore, type-C and type-D pegmatites are enriched in Nb, U and Th; while type-A pegmatites show higher Ti, Zr, Ce, U and Th contents.

K/Rb vs Rb

Biotite and K-feldspar show K/Rb decreasing with advancing crystallisation owing to rapid depletion of K and relative accumulation of Rb in the residual melt (Černý et al., 1985). In figure 5.5a a weak trend of enrichment of Rb from granites to pegmatites is particularly clear for type-C and D pegmatites, while type-A pegmatite has an unusually low content of Rb and high K/Rb. The Rb content and the K/Rb ratio of granites are mainly controlled by K-feldspar and biotite, so, not surprisingly, the alkali-rich type-A granite and type-C and D pegmatites are the richest in Rb.

K/Ba vs Ba

Barium content increases during magmatic fractionation up to 2000 ppm (K/Ba down to 20) in early granites, and becomes rapidly depleted with the onset of crystallisation of K-feldspar and other K minerals (Černý et al., 1985). In figure 5.5b this trend is well represented with an increasing K/Ba from granites to pegmatites; Ba content ranging from 500 ppm in calcic granite to 1500 ppm in alkali granite, and decreasing to contents as low as 24 ppm in the most evolved

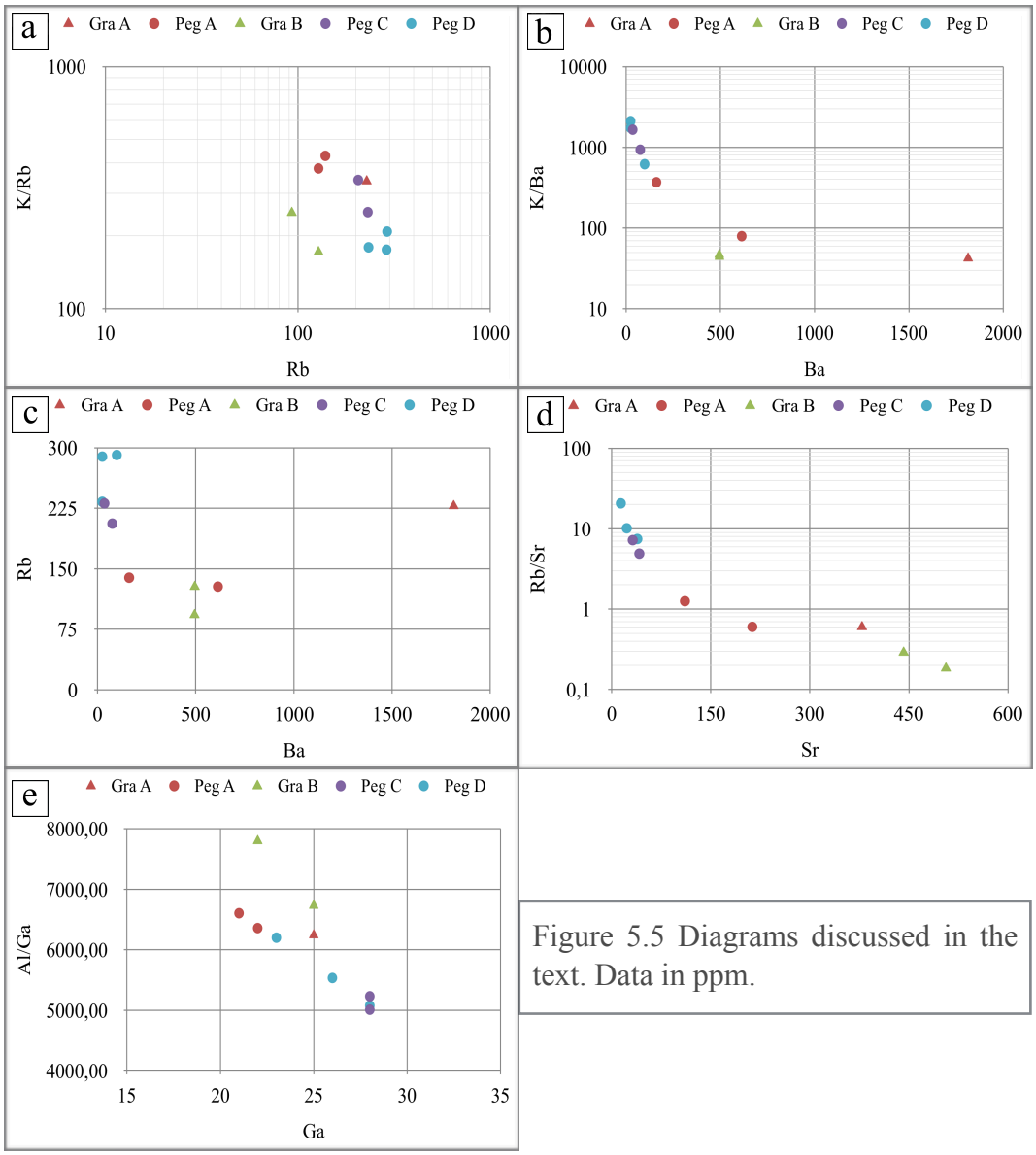


Figure 5.5 Diagrams discussed in the text. Data in ppm.

pegmatites. Guastoni (2012) observed that pegmatites which show sensible increasing in Ba content, above 100 ppm, and low K/Ba ratio are associated with NYF or mixed NYF-LCT geochemical character.

Ba/Rb

The depletion of Ba in late granitic differentiates is reciprocal to the behaviour of Rb, and so the Ba/Rb ratio is one of the most sensitive indicators of fractionation (Taylor & Heier 1960, Taylor 1963). Figure 5.5c then confirms that type-D pegmatites are the most fractionated ones. According to Černý et al. (1985) the Ba/Rb ratio of granitoid rocks varies from about 20 in tonalites to 2 in biotite granites. In our granitoids it is in the range 3-8, in type-A pegmatites it is as low as 1,16 and in type-D pegmatites down to 0,08.

Rb/Sr vs Sr

The Rb/Sr ratio is an indicator of fractionation, since Sr content of K-feldspars and thus of the whole rock, as well as Ba, changes antipathetically with its Rb content (Černý et al., 1985). In granites, the Sr content is higher in Ca-rich samples (up to 506 ppm) and lower in alkali-rich samples (379 ppm). Pegmatites appear to show a trend of decreasing Sr (as low as 14 ppm in type-D pegmatite) with increasing Rb/Sr (Fig. 5.5e).

Al/Ga vs Ga

Ga shows a slight concentration in residual melts. The absolute concentration of Ga varies with that of Al, and the average Al/Ga ratio decreases with differentiation (Černý et al., 1985). Figure 5.5f shows that Ga enrichment in pegmatites with respect to granites is not notable, though.

In conclusion, these diagrams show that:

i) type-A and type-B granites have trace elements composition within the typical compositional range for granitoid rocks;
ii) the differences in Ba, Rb and Sr contents between the two granite types is related to the high difference in Ca content (alkalic vs calc-alkalic granites);
iii) type-A pegmatites are less evolved than type-C and D;
iv) type-C and type-D pegmatites show Rb, Ba and Sr contents close to those typical for pegmatitic granites parental to groups and fields of complex rare-element pegmatites.

5.2 Classification of pegmatites

A classification of pegmatites is here attempted, following the scheme adopted by Černý and Ercit (2005).

Type-A pegmatite is enriched in Ti, Zr, Ce, U and Th. Besides the major rock forming minerals they contain apatite, allanite-(Ce), monazite-(Ce), thorite, titanite, euxenite-(Y), zircon, ematite, magnetite and ilmenite. Apatite, allanite and monazite-(Ce) are particularly abundant. These characteristics link this older pegmatite to the REL-REE subclass as described by Černý and Ercit (see also Tab. 5.2):

> *Members of the REL–REE subclass are derived chiefly from post- to anorogenic metaluminous to peraluminous granites at somewhat variable crustal depth, largely (but not exclusively) in extensional crustal settings (Černý 1991a, b). The REL–REE subclass has a characteristic assemblage of HFSE, and is subdivided into three types: allanite–monazite type, characterized by predominance of LREE, euxenite type with prominent Y, variable HREE/LREE ratio and negligible amounts to virtual absence of Be (Wise 1999), and gadolinite type, marked by dominance of HREE, Y and Be. The REL–*

REE pegmatites are impoverished in phosphorus (despite the characteristic presence of accessory REE phosphates), boron and sulfur and the contents of lithium, rubidium and cesium also are typically low (Černý 1991a, Brown 1999, Nizamoff et al. 1999).

Type-C and type-D pegmatites are enriched in Nb, Th and U and contain beryl, Fe-Mn garnet, zircon, thorite, columbite, uraninite, U-phosphates, apatite, monazite-(Ce), aeschynite-(Y) and hematite. Unfortunately XRF analysis cannot provide chemical compositions of light elements as Li, Be and B, and of discriminant elements as Cs and Ta but, considering the mineralogical assemblage (mostly the presence of beryl and columbite, both not observed in the A pegmatites) and the characteristic enrichment in Nb, we tentatively propose to classify type-C and type-D pegmatites in the beryl type of the REL-Li subclass as described by Černý and Ercit (see also Tab. 5.2):

The REL–Li subclass is emplaced at low-pressure and differentiated dominantly from (syn-to) late-orogenic peraluminous granites, largely (but not exclusively) in compressional orogenic regimes (Černý 1991a, b). The REL–Li pegmatites constitute the most diversified subclass in the whole classification spectrum, reflecting a broad array of rare elements and conditions of solidification. Rare alkalis, Be, Sn, Nb < Ta, B, P and F are typically accumulated with progress of fractionation in the REL–Li pegmatite suites. The beryl type is represented in its simplest form by the widespread beryl–columbite subtype. Although present in virtually all pegmatite bodies of this subtype, and commonly in substantial proportions, abundances of the minerals of Be and Nb–Ta are widely variable and their ratio may become very steep.

TABLE 5. SUBDIVISION OF GRANITIC PEGMATITES OF THE RARE-ELEMENT CLASS

Subclass Type	Subtype	Geochemical signature	Typical minerals	Examples	References
REL–REE					
allanite-monazite		LREE, U, Th, (Be, Nb>Ta, F, [P])	allanite, monazite, zircon, rutile, fluorite, ilmenite	Pacoima, Los Angeles, CA	Moller (1995)
				S group, South Platte, CO	Simmons *et al.* (1987)
				Helle, Kokjen and Sonnevig, Hitterö, NO	Adamson (1942)
				Oku–Tango belt (most), JP	Tatekawa (1955)
euxenite		L-H-REE, Y, Ti, Zr, Nb>Ta, (F, P)	euxenite, monazite, xenotime, zircon, rutile, ilmenite, (fergusonite, aeschynite, zinnwaldite)	Georgeville, NS	Murphy *et al.* (1998)
				Trout Creek Pass, CO	Hanson *et al.* (1992)
				Topsham, ME	Hanson *et al.* (1998)
				S Iveland (most), NO	Bjørlykke (1935)
				Alto Molocue, MOZ	Cílek (1989)
				Otozan and Morigami, JP	Minakawa *et al.* (1978)
				Mukinbuin field (most), WA, Australia	Jacobson *et al.* (2005)
gadolinite		Be, Y, HREE, Zr, Ti, Nb>Ta, F, (P)	gadolinite, fergusonite, samarskite, zircon, rutile, ilmenite, fluorite, (zinnwaldite)	N Iveland (most), NO	Bjørlykke (1935)
				White Cloud, CO	Simmons *et al.* (1987)
				Central Mineral dist., TX	Ehlmann *et al.* (1964)
				Shatford Lake group, MB	Buck *et al.* (1999)
				Ytterby and Osterby, SWE	Smeds (1990)
				West Keivy, Kola, Russia	Lunts (1972)
				Mategawa and Hama, JP	Minakawa *et al.* (1978)
				Cooglegong, WA, AU	Simpson (1951)
				Pyörönmaa, Finland	Vorma *et al.* (1966)
REL–Li					
beryl	beryl–columbite	Be, Nb–Ta, (±Sn, B)	beryl, columbite, tantalite, (rutile)	Meyers Ranch, CO	Hanley *et al.* (1950)
				Greer Lake group, MB	Černý *et al.* (1981)
				Donkerhoek, Namibia	Schneiderhöhn (1961)
				East Selden, CT	Cameron & Shainin (1947)
				Scheibengraben, CZ	Novák *et al.* (2003)
				Big Alstead, NH	Cameron *et al.* (1949)
	beryl–columbite phosphate	Be, Nb-Ta, P, (Li, F; ±Sn, B)	beryl, columbite, tantalite, triplite, triphylite	Hagendorf-Süd, Germany	Strunz *et al.* (1975)
				Dan Patch, SD	Norton *et al.* (1964)
				Crystal Mtn. field, CO	Thurston (1955)
				Palermo No. 1, NH	Francis *et al.* (1993)
				Cross Lake #22, MB	Ercit *et al.* (1986)
				Tsaobismund, Namibia	Fransolet *et al.* (1986)
				Nevados de Palermo, AR	Galliski *et al.* (1999)

Table 5.2 Subdivision of granitic pegmatites of the rare-element class after Černý and Ercit (2005)

Table 5.3 (next page) A summary of the enriched elements and the minerals present in the two types of pegmatite and the proposed classification.

	A pegmatite	C-D pegmatite
ENRICHED ELEMENTS		
Ti	✓	
Zr	✓	
Ce	✓	
Nb		✓
U	✓	✓
Th	✓	✓
MINERALS		
apatite	✓(+)	✓(−)
allanite-(Ce)	✓	
monazite-(Ce)	✓(+)	✓(−)
thorite	✓	✓
titanite	✓	
euxenite-(Y)	✓	
zircon	✓(+)	✓(−)
hematite	✓	✓
beryl		✓
Fe-Mn garnet		✓
columbite-(Mn)		✓
uraninite		✓
U-phosphates		✓
aeschynite-(Y)		✓
PROPOSED CLASS	*REL*	*REL*
PROPOSED SUBCLASS	*REE*	*Li*
PROPOSED TYPE	*allanite-monazite (?)*	*beryl (?)*

6. SUBMAGMATIC AND SOLID STATE DEFORMATION

6.1 Submagmatic to post-magmatic deformation of the sampled dykes

The pegmatite and granite dykes show several microstructures of deformation. In the sample 15-24A (type-A pegmatite), several large (up to 5-10 mm) K-feldspar and plagioclase crystals have fractures filled with quartz (Fig. 6.1a). These fractures are confined to single crystals and quartz filling them is coarser than that in the matrix and shows no intracrystalline deformation. Same features have been reported in the literature for the Bergell host rock (Davidson et al., 1996; Bouchez et al., 1992) and interpreted as evidence for deformation before complete crystallisation (submagmatic deformation) of the rock by melt-enhanced embrittlement (Davidson et al., 1994).

Microstructural observations of pegmatite and granite dykes indicate that they were also affected by solid state ductile deformation. The principal indicators of ductile deformation are:

(i) the development of a foliation (Fig. 6.1b), well recognisable already in the field, oblique to the dyke boundaries and defined by the iso-orientation of biotite crystals;

(ii) grain size reduction, serrated grain boundaries and crystal interfingering in quartz aggregates (Fig. 6.1c,d).

Only in the type-B microgranite, quartz is generally undeformed and only locally shows an undulose extinction pattern. In the microgranites the solid state deformation is less intense than in the other dykes, but a foliation defined by biotite crystals is commonly developed.

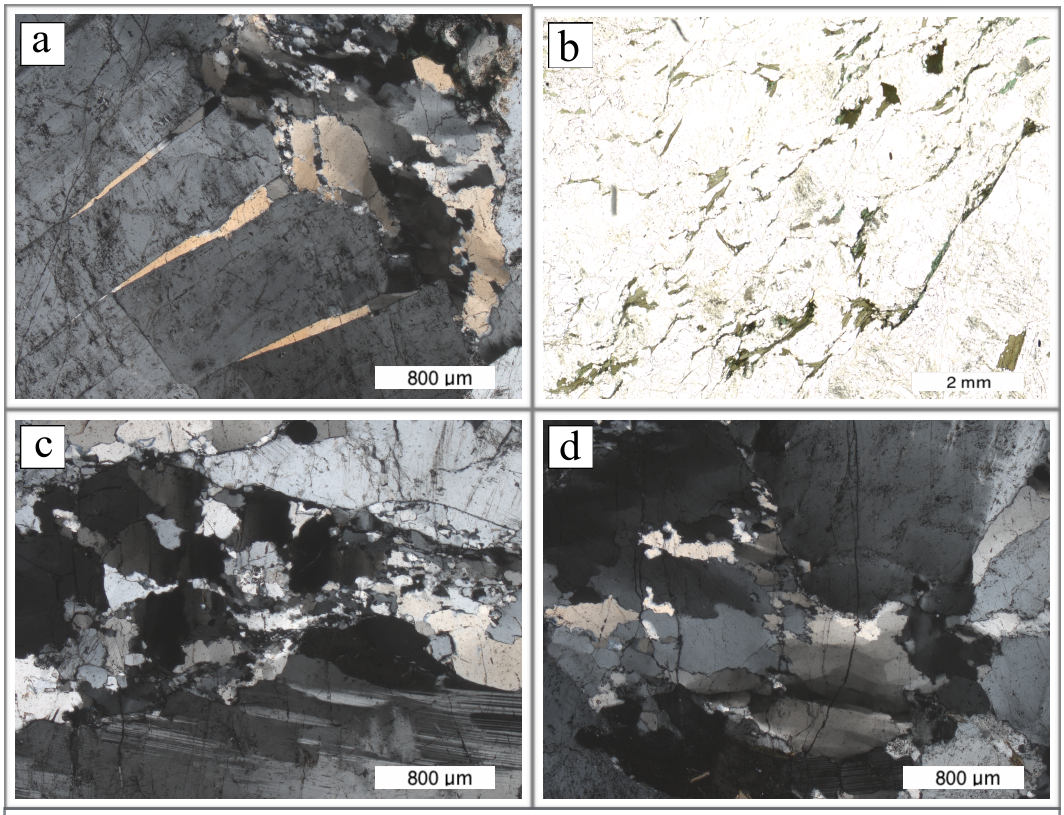


Figure 6.1 Micro-photographs of optical microstructures of deformation in the sampled dykes. **a)** Syn-magmatic fractures filled with quartz in K-feldspar (sample 15-24A). **b)** The iso-orientation of biotite crystals defines the foliation in a pegmatite (sample 15-21D). Plane polarised light, dyke boundary parallel to the base of the photos. **c-d)** Polygonisation, undulose extinction and recrystallisation in quartz aggregates (samples 15-24D and 15-24A).

6.2 Ductile deformation of the quartz veins

The microstructures of the ductilely deformed quartz veins have been studied in thin sections cut parallel to the stretching lineation (X axis of the shear zone reference frame) and orthogonal to the vein boundary that represents the shear plane (XZ plane). All the samples come from quartz veins that trend approximately N-S and dip steeply toward the W. Most of the shear zones have a dominant strike-slip kinematics with a little reverse component (pitch values

ranging between 0° and 30°), sense of shear being top to the south. This results in a sinistral sense of shear in the XZ section.

The shear deformation of the quartz veins is highly variable. Some veins are undeformed or weakly deformed, while other veins are mylonitic. However, the internal deformation within an individual vein is commonly heterogeneous and can include weakly deformed, coarse-grained portions adjacent to fine-grained, completely recrystallised, mylonitic domains. Therefore a single thin section can record the complete strain history of a quartz vein from low to high strains (e.g. Fig. 6.4d-f). We will distinguish, in the following descriptions, three different strain domains: low, medium and high strained quartz domains.

6.2.1 Low-strain domain

Coarse (up to 2 cm in size), poorly deformed grains are often preserved in low-strain domains. They commonly show undulose extinction or pervasive coarse subgrain (50-100 μm) polygonisation (Fig. 6.2f). The vein quartz grains locally include deformation lamellae (Fig. 6.2a), visible as fine sub-parallel planes with a slightly different refractive index from that of the host grain. Incipient bulging recrystallisation (Fig. 6.2e) commonly occurs along the grain boundaries, and locally evolved to thin (one or few grains thick) fine grained (10-20 μm) aggregates of new grains.

Fine recrystallisation, with the new grains of a similar grain size as the ones developed along the grain boundaries (i.e. 10-20 μm), also occurred along discrete fracture-like sets within the the large vein grains (Fig. 6.2b-d). These ‘discrete zone of recrystallization’ (DZR) initiated as one-grain-thick strings and progressively thickened with increasing strain accumulation. The grain size of these newly formed crystals is much smaller than the size of the subgrains in the polygonised grains. This microstructure in our samples has always been observed to be relegated within single crystals without crossing the grain boundaries. The

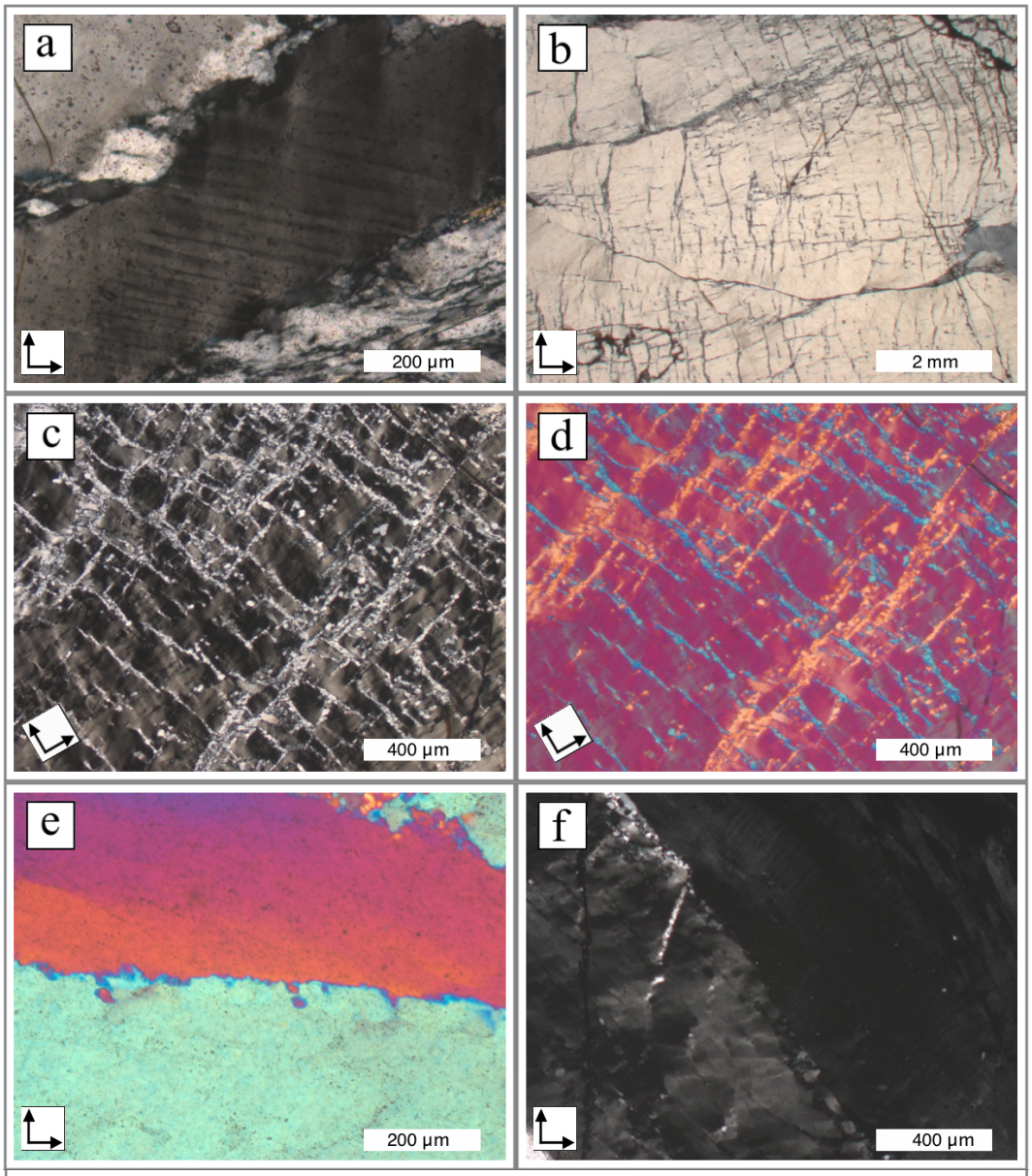


Figure 6.2 Optical microstructures of the quartz veins in the low-strain domain. The micro-photographs were taken with crossed polars and, in d) and e), with the addition of the gypsum plate. The vein boundary is parallel to the base of the photos except in c) and d). The shear sense is sinistral. **a)** Deformation lamellae trending 'ENE-WSW', in an elongated quartz grain (sample 14-025). **b)** DZRs intersecting at a high angle within a coarse vein crystal (sample 14-502). **c-d)** Detail of the previous microstructure. Blue-coloured dextral DZRs show left-stepping patterns while yellow-coloured sinistral DZRs are right-stepping (sample 14-502). **e)** Bulging along the boundary between two nearly undeformed grains (sample 14-502). **f)** Coarse subgrains within the crystal on the left-hand side. (sample 14-502).

DZRs in this weakly strained coarse vein crystals, commonly occur in 2 sets which are almost orthogonal to each other. With progressive shear accumulation along the DZR, the recrystallised grains acquire a slightly elongated shape (though the aspect ratio is very low) defining a shape preferred orientation (SPO) oblique to the DZR boundary and indicative of the sense of shear. The croscutting relationships between the different sets of DZR do not indicate a time sequence in the development of the different planes. The incipient DZR are commonly segmented and arranged en-echelon with the stepping of the segments consistent with the sense of shear of the overprinting ductile deformation (i.e. dextral microshear zones overprint left stepping DZR and viceversa). The aggregates of new grains inside the DZR microshear zones have a strong crystallographic preferred orientation (CPO) which is distinctly different from the crystallographic orientation of the host grain. Under crossed polars and with gypsum plate inserted, the new grains and the host grain show clearly distinguished colours (Fig. 6.2d). The DZR are not present in all the vein quartz grains and their development is different in different grains. This suggests a crystallographic control over the development of these features.

6.2.2 Medium-strain domain

Medium-strain domains are characterized by subparallel mono-crystalline ribbons with thickness ranging from hundreds of μm to millimetric, locally extending for the whole length of the thin section, i.e. more than 2 cm (Fig. 6.3). These ribbons define an oblique foliation (in the range of 10°-20° in the investigated thin sections) in the quartz veins defining the sense of shear zone of the overprinting ductile deformation (6.3f). The aspect ratio of the different elongate or ribbon domains is variable and is likely to reflect the different crystallographic orientation of the original vein quartz crystals.

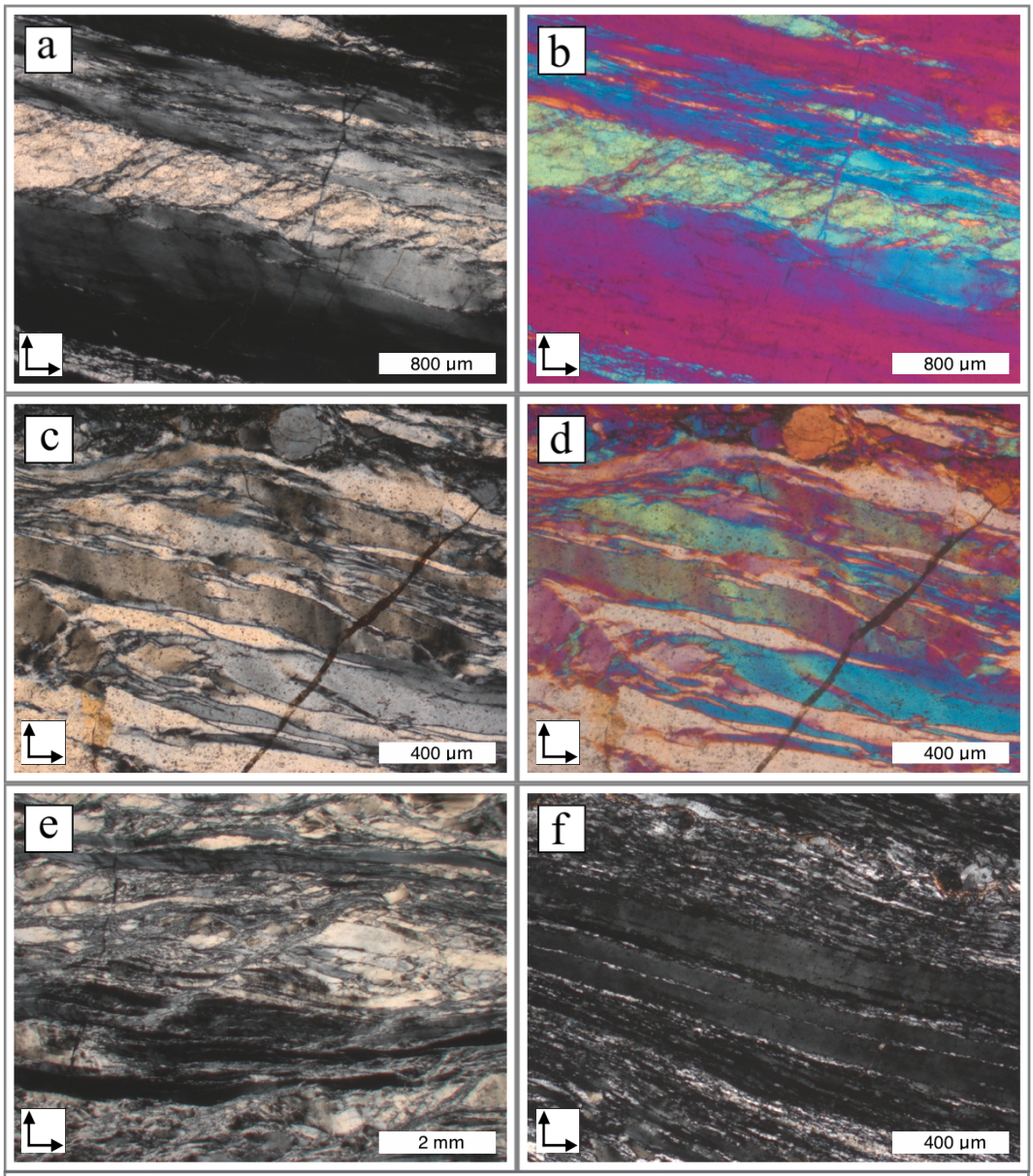


Figure 6.3 Optical microstructures of the quartz veins in the medium-strain domain. All the micro-photographs taken with crossed polars and, in b) and d), with the addition of the gypsum plate. The vein boundary is parallel to the base of the photos. The shear sense is sinistral. **a-b)** The three dominant kind of microstructures in the medium strain domain. At the bottom an elongated, internally strain-free, black ribbon of quartz. The bright white ribbon in the middle is cut, in this case mainly by synthetic micro-shear zones (yellow to red coloured, from top right to bottom left in b). The ribbon on top shows the kind of microstructure described in the text and better illustrated in c) and d) (sample 14-022). **c-d)** A single crystal (pale yellow in d)) contains several 'kinked' domains that have approximately all the same orientation (blue to green in d)); (sample 14-025). **e)** Synthetic micro-shear zones cut the ribbons and form

isolated lozenge-shaped porphyroclasts. Black ribbons have high aspect ratio and remain mainly internally strain-free (sample 14·022). **f)** The elongation of the ribbons defines the foliation, at a low angle to the vein boundary (sample 14·022). Once again, the highest aspect ratio ribbons are those always extinct.

Crystals that have dark to black colour under crossed polars (i.e. crystals oriented with their *c* axes subparallel to the Y-direction) do not exhibit evident undulose extinction, polygonisation and recrystallisation and commonly correspond to the highest aspect ratio ribbons. The DZR are commonly absent in these ribbons (Fig. 6.3a,b,f).

Other grains that do not present the *c*-axis parallel to Y, are less elongated and appear "unstable" being dissected and dismembered, along the microshear zones evolving from DZR, to separated quartz domains or porphyroclasts (Fig. 6.3a,b,e). In these ribbons the synthetic shear bands (i.e. having the same shear sense as the bulk shear and commonly inclined 30° to the ribbon boundary) are much more common than the conjugate set. As result of dissection along the microshear zone the original ribbons are separated into lozenge-shaped domains embedded into a matrix of recrystallised grains. These new grains have a strong CPO (Fig. 6.3b). The evolution of this process lead to the development of quartz porphyroclasts within a matrix of fine grained quartz. These porphyroclasts commonly show bright white colour under crossed polars (Fig. 6.3e).

In many cases, the individual ribbons can be seen as original vein crystals stretched during shearing of the vein. However, this is not always the case. Some ribbons show an internal subdivision into finer (thinner) ribbons (Fig. 6.3c,d) which do not reflect an original grain orientation but develop as result of deformation. The nature of this process is unclear. These thinner internal ribbons are lens-shaped, elongated parallel to the parent ribbon grain and develop new crystallographic orientations within the original grains. This affected the distribution of polygonisation and recrystallisation within these ribbons as strain was progressively accumulated.

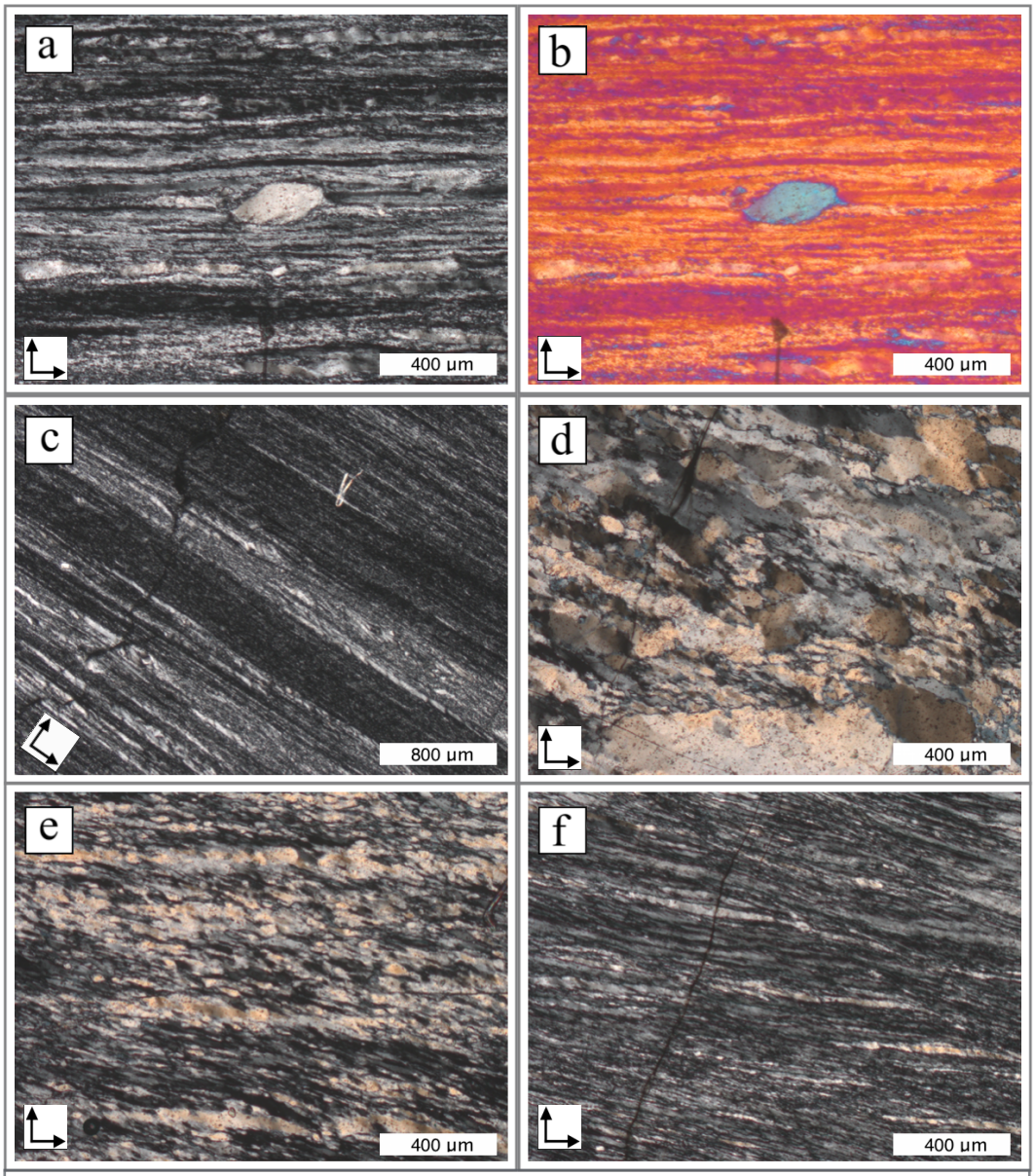


Figure 6.4 Optical microstructures of the quartz veins. All the micro-photographs taken with crossed polars and, in b), with the addition of the gypsum plate. The vein boundary is parallel to the base of the photos except in c). The shear sense is sinistral. **a-b)** In the high strain domains, the ribbons recrystallised almost completely, although some remnants are still recognisable. The foliation is subparallel to the vein boundary (horizontal) (sample 14-022). **c)** Extinction banding in the fine recrystallisation aggregate (sample 14-022). **d-f)** Comparative micro-photographs of the microstructures of a quartz vein at the same magnification along a vertical transect in the same thin section. From d) to f) the intensity of deformation is increasing. With increasing deformation the grain size decreases and the foliation rotates toward the vein boundary (sample 14-491).

The medium strain domain commonly shows the development of a secondary foliation, corresponding to an *extensional crenulation cleavage*, delineated by narrow microshear zones of recrystallised quartz. The grain size of quartz along the ECC is identical to the grain size of the aggregates developing along the main foliation as result of ribbon recrystallisation.

6.2.3 High-strain domain

High-strain domains are quartz mylonites consisting of a large proportion of fine (less than 10 μm) recrystallised grains (Fig. 6.4a-c). The main foliation in these domains is defined by the orientation of thin (generally less than 50 μm) relict of ribbons (Fig. 6.4a,b) and by a domainal CPO evidenced by extinction banding (Fig. 6.4c). This extinction banding is probably inherited from the previous different CPO of the ribbons. The mylonitic foliation is subparallel to the vein boundary indicative of high shear strain for pervasive recrystallization. The recrystallised grains are elongated with their long axes defining a shape preferred orientation (SPO) oblique (25-30°) to the main foliation and to the shear zone boundary and consistently inclined with the sense of shear. The fine-grained (down to less than 10 μm) recrystallised quartz aggregate show a dominance of dark colours under cross polars (red when the gypsum plate is inserted), meaning that most of the recrystallised grains have their *c*-axis near to the Y-axis.
Wrapped in the mylonitic foliation the remnants of the earlier deformation phases are represented by relict of quartz ribbons, still internally strain-free or showing a weak polygonisation, and quartz porphyroclasts, produced by the dismantling of the ribbons (Fig. 6.4a,b). These porphyroclasts are typically lozenge-shaped and show a bright white colour under crossed polars. The shape of these porphyroclats, isolated in the matrix mainly by disruption of ribbons by the synthetic set of micro-shear zones, has a monocline symmetry that can suggest the opposite sense of shear if the porphyroclast origin is not considered.

6.3 Deformation history of the quartz veins

In summary we envisage the following deformation evolution of the quartz veins. The first stage of deformation induced the development of subgrain, deformation lamellae, and fine recrystallization along the grain boundaries (bulging) and along sets of discrete fracture-like features within the original coarse grain veins crystals.

With increasing strain, the original vein crystals were stretched to ribbons with different aspect ratios and different internal microstructures depending on their crystallographic orientation. Grains originally well oriented for intracrystalline slip under the dominant ambient conditions of deformation were stretched to very elongate ribbons and did not develop any conspicuous internal microstructure. These grains show the c-axis parallel to the Y-direction of the shear zone reference frame. Grains that were not "suitably" oriented were stretched to a lesser extent and dissected by two conjugate sets of microshear zones evolving from discrete zones of recrystallisation. The conjugate sets with ongoing deformation link to each other and form an anastomosed matrix of very fine recrystallised grains that wraps the undeformed domains, forming relatively big quartz porphyroclasts in a soft, fine grain quartz matrix. Some other 'not suitably oriented' ribbons show an internal subdivision into thinner, lens-shaped ribbons, elongated parallel to the parent ribbon grain and showing a different crystallographic orientation (Fig. 6.3c,d).

Eventually, with progressive deformation, the recrystallisation becomes pervasive and affect these domains too, even though relics of the previous porphyroclasts, locally showing incipient polygonisation, are still present. The last phase of dynamic recrystallisation produces an homogeneous aggregate of very small grains (down to less than 10 μm), that are in turn affected by ductile deformation since they show an elongation that defines a shape preferred orientation.

6.4 Crystallographic preferred orientations (CPO) of the quartz veins

The CPO of the deformed quartz veins was determined, for the *c* axes alone, by computer-integrated polarisation microscopy (CIP) (Panozzo Heilbronner and Pauli, 1993; Heilbronner, 2000) in the medium strain domain and by X-ray texture goniometry (TG) in the high strain domain. While TG allows a volume-related, quantitative texture analysis, the CIP method gives a microstructure-related *c*-axis orientation, which can be visualized by an axis distribution analysis.

6.4.1 Medium-strain domain

The analysis of the *c*-axis CPO by CIP was carried out in a medium-strain domain of the sample 14-30 (Fig. 6.5). This is a preliminary analysis whose aim is to determine the evolution of the CPO within a strain gradient across an individual vein.

The CIP pole figures (Fig. 6.5c,d) indicate that a strong bulk CPO of the *c* axes, approximately defining a single girdle slightly concentrated near the Y-axis, was already achieved in the medium strain domain. Part of these CPO is probably inherited from the crystallographic orientation of the pristine vein crystals. However, the *c* axes from the periphery to the centre of the girdle stem from *c* axes of grains deformed by basal <a>, rhomb <a> and prism <a> slip respectively (Fig. 6.6). Since the girdle is slightly concentrated around the Y-axis, prism <a> is probably the most important intracrystalline slip system.

The *c*−axis orientation images (COIs) are useful to investigate the relationships between microstructure and CPO. The COIs of figure 6.5b show that the ribbons with the highest aspect ratio are white-coloured, which means that their *c* axes plot near the Y-axis in the pole figure. This supports the idea that prism <a> is the most efficient slip system during the deformation. The other ribbons, showing *c* axes toward the periphery of the girdle, have a low aspect ratio and show a

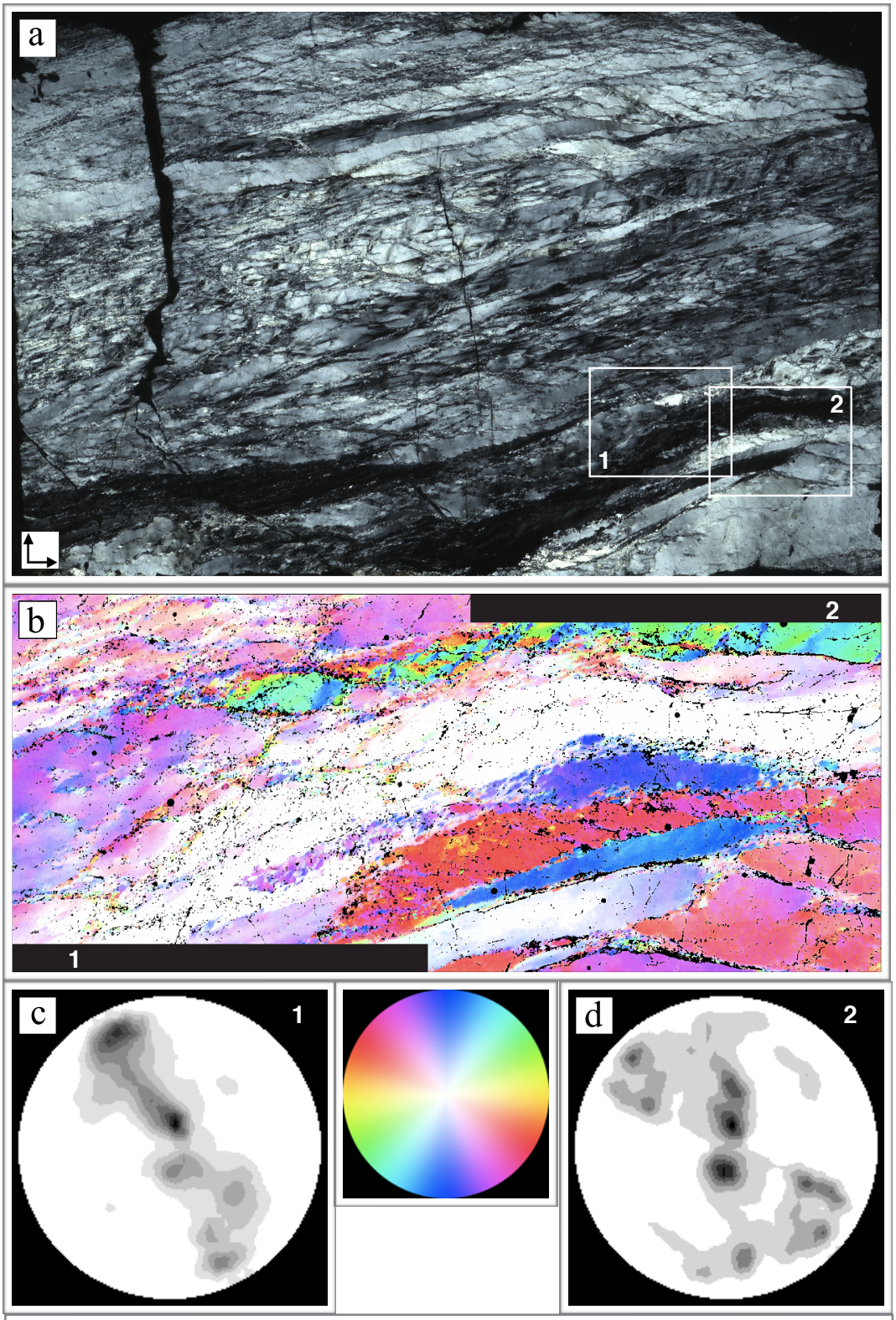


Figure 6.5 **a)** Crossed polars scan of thin section 14-30, with indicated the areas investigated with the CIP analysis. **b)** COIs (c−axis orientation images) **c-d)** CIP pole figures (equal area, lower hemisphere projections).

stronger internal distortion and polygonisation.

6.4.2 High-strain domain

CPO of the high-strain domain have been analysed by X-ray texture goniometry. The high-strain domain shows a strong bulk CPO characterized by *c* axes [001] distributed in a partial YZ girdle strongly concentrated near Y (Fig. 6.7). The c−axis CPO has a monocline symmetry, with the tips of the *c*-axis girdle slightly

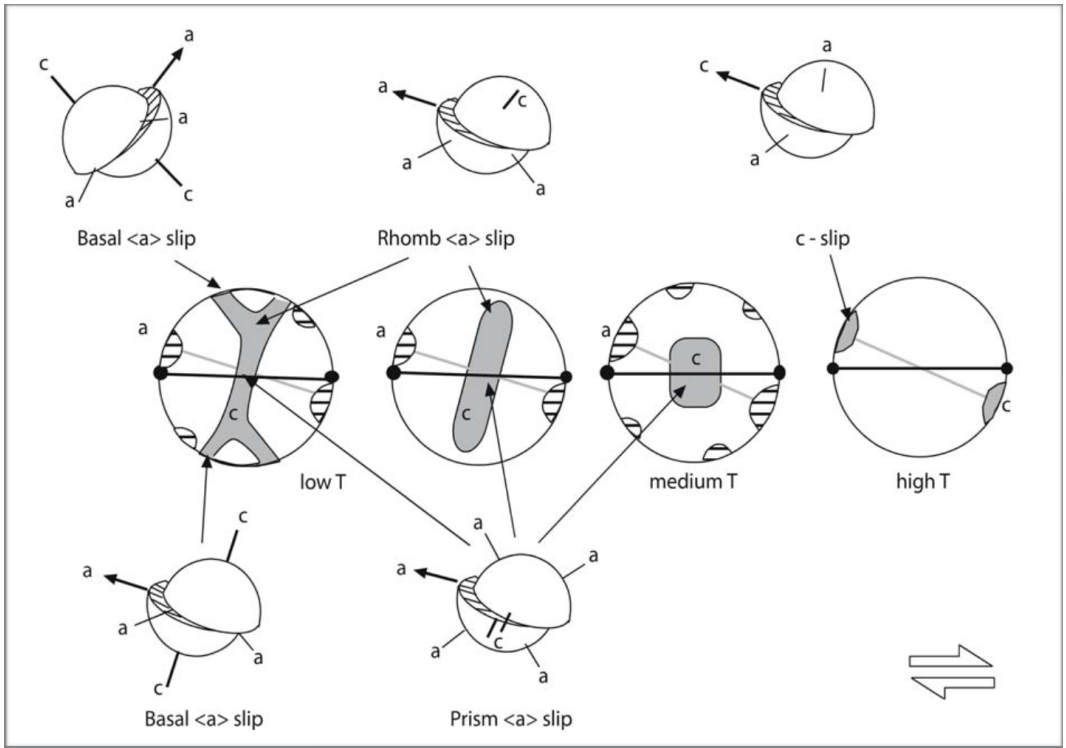


Figure 6.6 Pole diagrams showing four types of contoured CPO patterns of quartz c-axes (*grey*) and a-axes (*striped*) such as develop with increasing temperature in non-coaxial progressive deformation. The variation is due to a change in the dominant slip systems. At low temperature, basal <a> slip is most important and the girdles may have a strong cluster of c-axes in the periphery. With increasing temperature, prism <a> slip becomes more important (Wilson 1975; Bouchez 1977; Lister and Dornsiepen 1982; Law 1990) and the girdle tends to a maximum around the *Y*-axis. From Passchier and Trouw (2005).

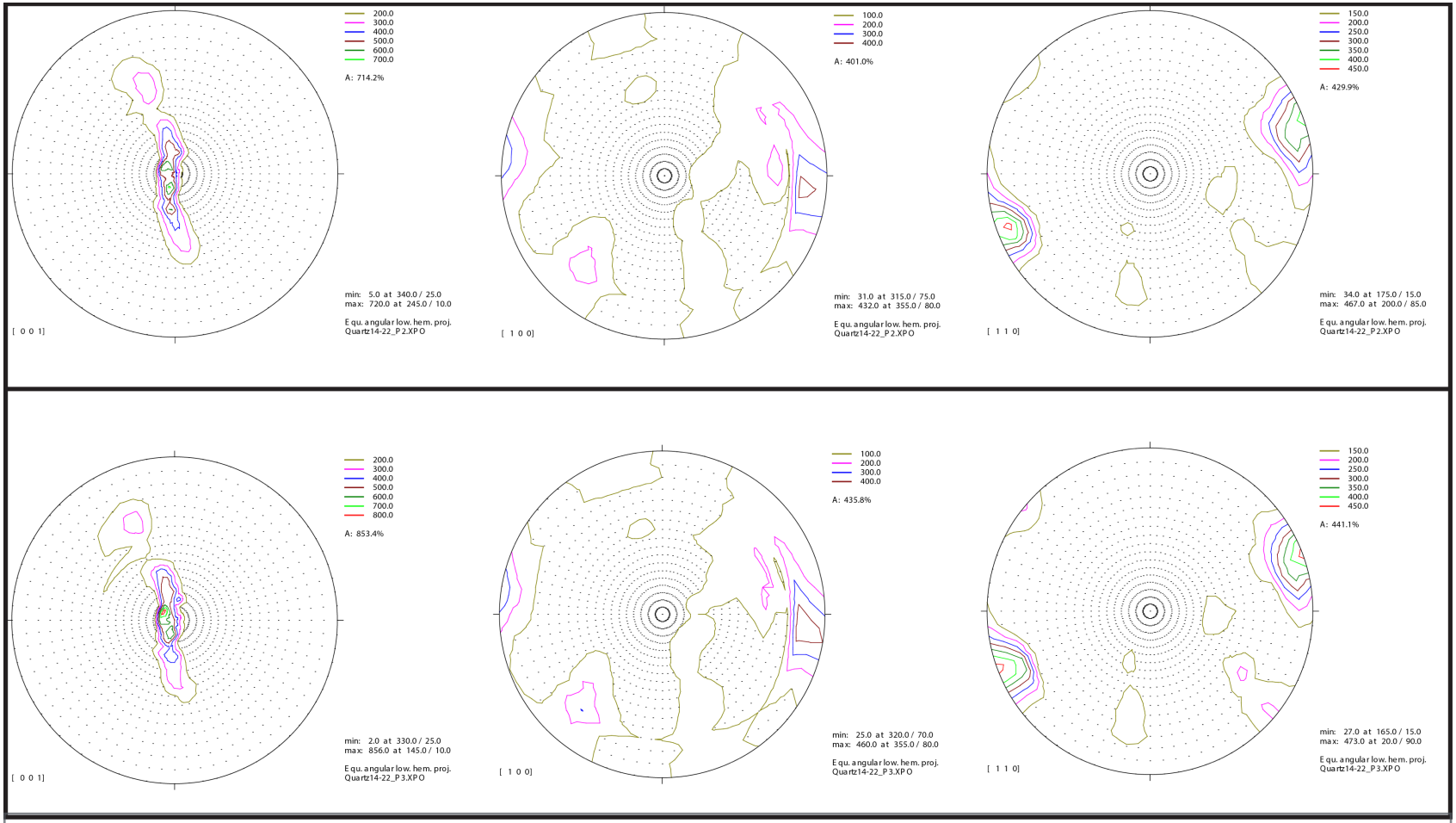


Figure 6.7 Plots (equal area, lower hemisphere projections) of two areas of the high-strain domain in sample 14-022, determined by texture goniometry. The plots are cumulative and the total area investigated in each sample is around 0,5 cm

bent in the direction of shear. The *a* axes [110] show strong and well−defined maxima at the periphery of the pole figure, with two main maxima forming a small angle with the lineation.

6.4.3 CPO evolution and comparison with the Adamello pluton quartz veins

Despite the preliminary character of the CPO analysis of the deformed quartz veins of the Bergell pluton, the CIP analysis indicates that, in the protomylonitic stage, the *c* axes define a girdle that is indicative of the activity of the basal <a>, rhomb <a> and prism <a> slip systems. The prism <a> is probably dominant over the other slip systems. In quartz mylonites, the CPO progressively evolved to a single Y maximum of c axes, indicative of largely dominant prism <a> slip.

The quartz CPO evolution studied here are rather similar to that of quartz veins from the Adamello pluton (southern Alps, Italy) (Pennacchioni et al., 2010), suggesting similar conditions of deformation for the 2 Periadriatic plutons.

According to Stipp et al. (2002), the transition from combined basal, rhomb, and prism <a> slip to dominant prism <a> slip (and therefore from a YZ girdle to a dominant single Y maximum in the *c*−axis pole figures) is rather abrupt and occurs at about 500°C. Based on this and other lines of evidence, Pennacchioni et al. (2010) concluded that the Adamello quartz veins opened and were deformed by simple shear within the range between 580°C and 500°C, during post-magmatic cooling of the Adamello pluton. Therefore, the comparison with the Adamello quartz veins allow us to conclude that the ductile deformation of the Val dei Ratti quartz veins occurred at a relatively high temperature, perhaps higher than 500°C.

Despite being deformed at similar conditions of temperature, the deformed quartz veins of the Bergell pluton show a marked difference in grain size with respect to those of the Adamello pluton. In fact, in the finest-grained mylonitic domains the former have a grain size down to less than 10 μ, while in the latter the new

grains have a grain size in the range of 34-40 μm (Pennacchioni et al., 2010). This discrepancy could be explained in at least two ways: (i) a higher strain rate in this area of the Bergell pluton with respect to the Adamello or (ii) a lower content of fluid phase along the grain boundaries during recrystallisation in the Bergell mylonites. Many recent studies (e.g. Mancktelow and Pennacchioni, 2004), in fact, have demonstrated that the content of fluid phase has a strong influence on the deformation mechanism (and thus on the grain size), but does not influence the activity of the slip systems.

6.5 Granitoid mylonite

In one of the studied thin sections mylonitisation affected also the host granitoid, for a thickness of c.a 1 cm (Fig. 6.8a,b). Quartz in the granitoid mylonite shows similar microstructures as in mylonitic quartz veins. The recrystallisation grain size of quartz aggregate is very small and homogenous, even though long and thin quartz ribbons are still present. In the granitoid mylonite feldspars commonly resist as porphyroclasts up to the ultramylonitic stages without being replaced by reaction products. This feature is typical of "amphibolite-facies" conditions (Pennacchioni, 2005; Pennacchioni & Zucchi, 2013). Biotite is stable during deformation and was only locally and statically replaced by chlorite. Accessory minerals are rutile, apatite and epidote. Feldspar porphyroclasts asymmetries, S-C fabric, asymmetric folding of the quartz ribbons and SPO of the recrystallised quartz aggregates are all consistent with a sinistral sense of shear.

6.6 Brittle deformation

The mylonitic fabric of the quartz veins is then locally overprinted by cataclasites. These fault rocks are characterised by angular fragments of quartz mylonite of variable size in a very fine greenish to brownish matrix (Fig. 6.8e). The contact

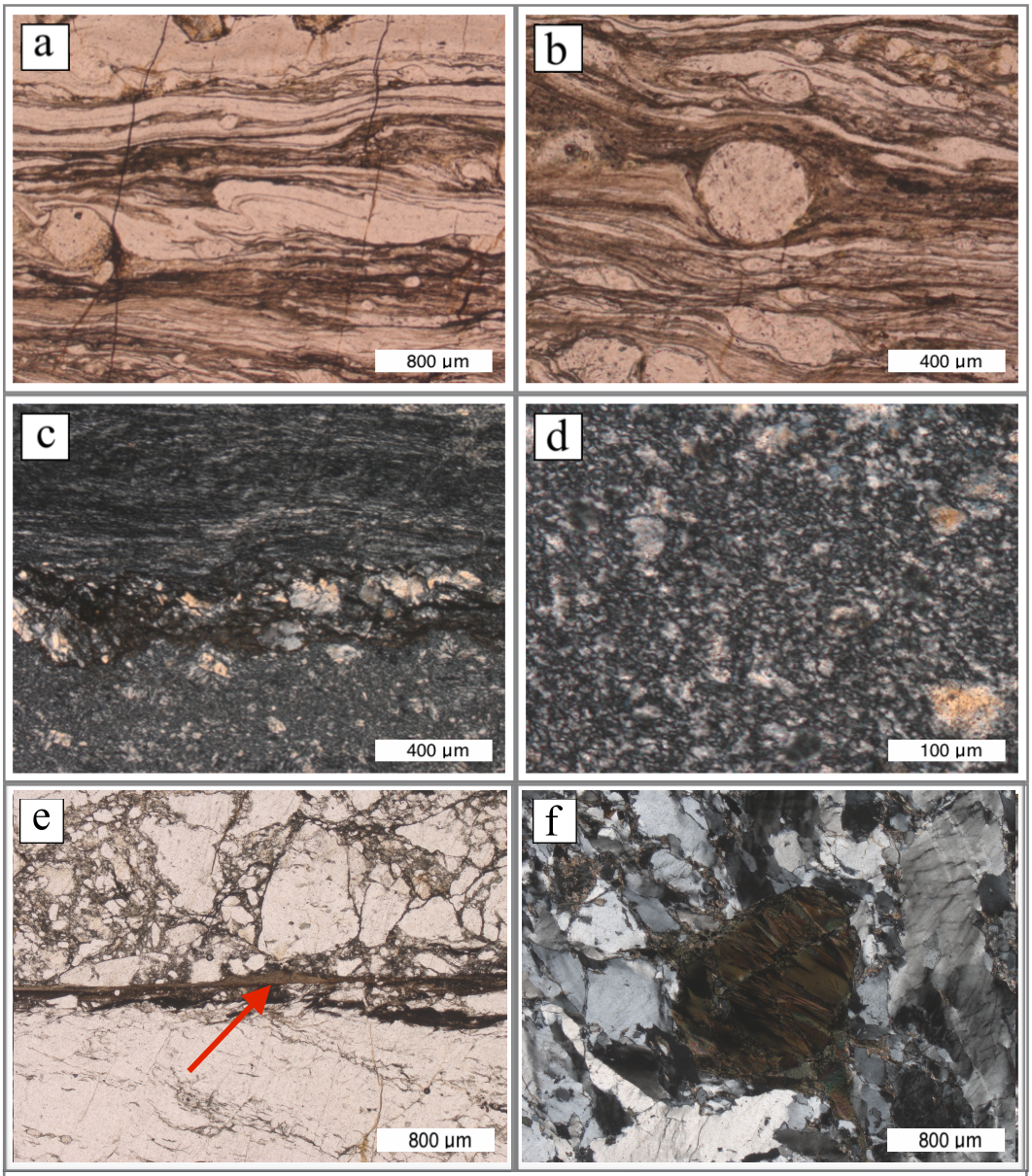


Figure 6.8 **a-b)** Optical microstructures of a granitoid mylonite flanking a quartz vein. Microphotos taken with parallel polars. Sense of shear is sinistral. The clearest kinematic indicators are the asymmetric folding of the quartz ribbon in a) and a feldspar sigma-porphyroclast in b). C-type shear bands defining an S-C fabric (where S is parallel to the base of the photo and thus to the shear zone boundary) are particularly clear in b) (sample 14-025). **c)** Sharply bounded 'cataclastic' layer in a quartz mylonite. See text for description (sample 14-491). **d)** Detail of c). Bigger clasts on the order of a hundred of microns show previous mylonitic fabric (sample 14-491). **e)** Pseudotachylite vein (red arrow) cutting through a cataclastic layer (sample 14-499). **f)** Kinked biotite crystal in proximity of the pseudotachylite vein (sample 14-499).

between the cataclasite and the intact mylonite is gradual. Commonly the cataclastic layers are cut by high angle extensional microfaults. Along the cataclastic bands, fluid infiltration leads to the precipitation of minerals other than quartz. The most common are epidote, chlorite and biotite.

In sample 14-491 a two-millimeter-thick 'cataclastic' layer parallel to the vein boundary, shows peculiar characteristics (6.8c,d). The layer is purely quartzitic and it has an heterogeneous grain size; the boundary with the intact mylonite is sharp. Large (up to a few hundreds of microns) clasts are wrapped in a fine matrix, resembling a cataclastic fabric. The clasts are randomly oriented and clearly show a previous ductile fabric, compatible with the medium-strain domain described above. So they probably are the result of the cataclasis of a medium-strain domain in the quartz vein. However, the matrix is not evidently cataclastic. The smaller grains have a grain size comparable to the grain size of recrystallised grains in the high-strain domains, they are not angular, on the contrary they are often slightly elongated and the aggregate shows a weak shape preferred

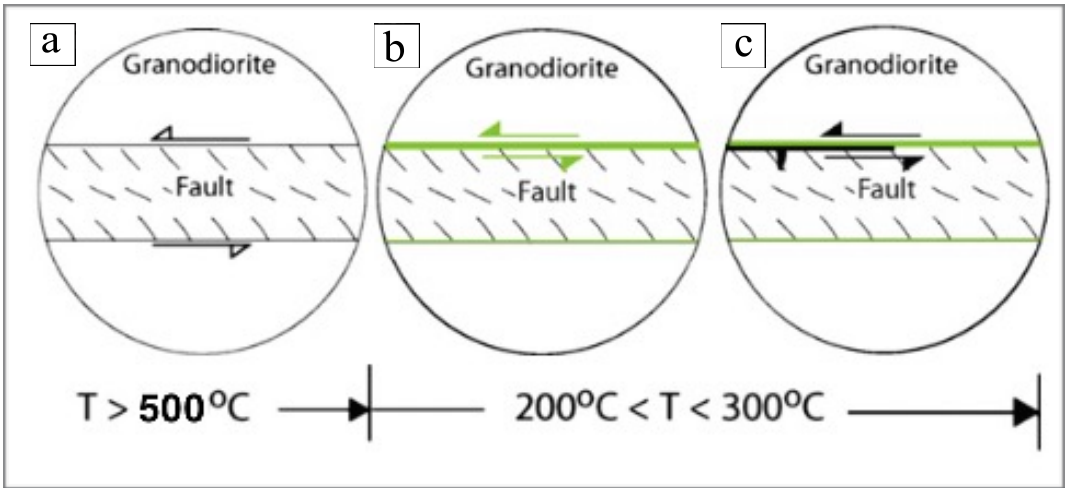


Figure 6.9 Microstructural evolution of the quartz veins. **a)** Quartz precipitated in dilatational regions along faults is sheared at temperatures probably greater than 500°C producing quartz mylonites. **b)** Boundaries between mylonites and granodiorites are filled with chlorite-epidote veins and reactivated by cataclasites. Locally cataclasites and epidote veins cut across mylonites. **c)** Thin, discontinuous pseudotachylyte veins form due to seismic slip, and locally cut mylonites and cataclasites. Modified from Griffith et al., (2008).

orientation. This microstructure deserves further investigation but we speculate, solely based on the optical microstructure, that it could represent a recrystallized cataclasite.

Within the ductilely deformed quartz veins, it has also been observed the occurence of *low angle synthetic microfaults* in an isolated feldspar crystal wrapped by the quartz mylonitic fabric. This microstructure indicates the brittle behaviour of feldspar at the same conditions at which quartz deforms mainly ductilely. These microfaults are filled with biotite, later retrograded into chlorite. All these shear sense indicators are consistent with a bulk sinistral shear sense.

In sample 14-499, the cataclastic layer is cut by a pseudotachylite (Fig. 6.8e). It is characterised by a main fault vein made of a dark brown opaque matrix with minor inclusions of mineral fragments. The vein has distinct, sharp and straight boundaries with the wall rock when it is in contact with quartz, while it shows typical embayments when in contact with the micaceous matrix. No injection vein is visible in the thin section. In proximity of the pseudotachylite biotite crystals show pervasive fine kinking (Fig. 6.8f) which is a typical microstructure of micas close to pseudotachylites (Bestmann et al., 2011, 2012).

7. CONCLUSIONS

7.1 The pegmatite field of the Central Alps in the Val dei Ratti area

i) In the Val dei Ratti area the pegmatite field of the Central Alps is represented by a polyphasic magmatism testified by a swarm of numerous aplite, pegmatite and granite dykes with different orientations. Through a detailed field study we have been able to distinguish four sets of dykes (named A, B, C and D in an older to younger sequence) with constant orientations and crosscutting relationships.

ii) All the sampled dykes have a granitic composition, are subalkaline, belong to the calc-alkaline serie and are slightly peraluminous. Type-A pegmatite is enriched in Ti, Zr, Ce, U and Th, and we tentatively propose to classify it in the allanite-monazite type of the REL-REE subclass. Type-C and type-D pegmatites are enriched in Nb, Th and U and contain beryl and Fe-Mn garnet, not observed in type-A pegmatite. We tentatively propose to classify type-C and type-D pegmatites in the beryl type of the REL-Li subclass. Type-D pegmatite shows the highest degree of evolution.

iii) The main set of pegmatite dykes in the Codera area of Guastoni et al. (2014), coincides in orientation with the set A of the studied area. In both areas these older dykes are crosscut by microgranite dykes (set B), that, as suggested by Guastoni et al. (2014), are possibly related to the emplacement of the Novate granite. The main set of pegmatites from the Bodengo area of Guastoni et al. (2014) shares the same orientation of the younger pegmatite set of the studied area (set D). Pb/Th dating on monazite yielded two different age groups with Codera pegmatites ranging from 28 to 25 Ma, and Bodengo ones from 23 to 19 Ma (Pozzi, 2014).

iv) If we interpret set B as coeval with the Novate granite (24,0 Ma according to Liati et al., 2000), we can speculate that a correlation there is between set A and the pre-Novate Codera pegmatites and between set D and the post-Novate Bodengo pegmatites.

7.2 Post-magmatic deformation in the Bergell pluton

i) Ductile shear zones that developed during the cooling of the pluton exploited precursor (or pre-existing) planar heterogeneities that include: (i) joints/ fractures, (ii) quartz veins, (iii) biotite-rich layers within granite dykes, (iv) mafic enclaves and melanocratic bands in the host rock, (v) magmatic foliation of the host rock, (vi) mafic dykes. The pegmatite dykes do not look to have localised the deformation.

ii) All the sets of dykes are crosscut by a set of ductilely deformed quartz veins. The microstructure and CPO of the quartz veins are comparable to those of the Adamello pluton quartz veins studied by Pennacchioni et al. (2010) and indicate that the ductile deformation is likely to be occurred at temperatures higher than 500 °C. Therefore, all the dykes were emplaced at temperatures higher than 500 °C.

7.3 Future development

The final aim of the work is dating the different dykes whose relative sequence of emplacement has been established in this thesis. Preliminary work for dating has been performed during the thesis with separation of monazite, apatite and zircon from 2 sets of samples each representative of the whole sequence of dykes of the area. The aim of dating is to discriminate between the following possible scenarios:

i) in the Val dei Ratti area it is exposed a dyke intrusion sequence that cover the entire time span of the pegmatite field intrusion, with older ‘Codera-like’ dykes and younger ‘Bodengo-like’ dykes;
ii) in the Val dei Ratti area it is represented a polyphasic magmatism of ‘Codera-like' age, and the younger ‘Bodengo-like’ dykes are not represented.

From field relationship and mineralogical and geochemical data shown in this thesis, the first scenario seems plausible. However, to prove (or prove wrong) this interpretation, dating of each set of dykes is needed. U-Th-Pb dating on monazite is in progress with this aim. Furthermore, since we demonstrated that the dykes were emplaced at high temperatures, U-Th/He dating on zircon will provide a minimum age of emplacement for the dykes, and thus an independent control over the monazite ages.

This will give more information in order to discriminate whether there was a migration in time and space of the pegmatite magmatism or in every different area of the pegmatite field all the dykes intrusion events are represented.

BIBLIOGRAPHY

Berger, A., Rosenberg, C and Heilbronner, R. (1994): Deformation of polyphase rocks at different temperature conditions (fi): microstructural and textural development of biotite in the Bergell tonalite. Annales Geophysicae 12, C90.

Berger, A., and R. Gieré (1995): Structural observations at the eastern contact of the Bergell pluton, Schweiz. Mineral. Petrogr. Mitt., 75, 241–258.

Berger, A. and Stünitz,H. (1996): Deformation mechanisms and reaction of hornblende: examples from the Bergell tonalite (Central Alps). Tectonophysics 257,149-174.

Berger, A., Rosenberg, C. and Schmid, S.M. (1996): Ascent, emplacement and exhumation of the Bergell pluton within the Southern Steep Belt of the Central Alps. Schweiz. Mineral. Petrogr. Mitt., 76, 357-382.

Best, M. G. 2003. Igneous and Metamorphic Petrology, 2nd ed. xxi+729 pp. Oxford Blackwell Science.

Bestmann, M., Pennacchioni, G., Frank, G., Göken, M., de Wall, H., 2011. Pseudotachylyte in muscovite-bearing quartzite: coseismic friction-induced melting and plastic defor- mation of quartz. Journal of Structural Geology 33, 169–186. http://dx.doi.org/10. 1016/j.jsg.2010.10.009.

Bestmann, M., Pennacchioni, G., Nielsen, S., Göken, M., de Wall, H. (2012), Deformation and ultrafine dynamic recrystallization of quartz in pseudotachylyte-bearing brittle faults: A matter of a few seconds, Journal of Structural Geology 38 (2012) 21e38

Bouchez JL (1977) Plastic deformation of quartzites at low temperatures in an area of natural strain gradient. Tectonophysics 39:25–50

Bouchez, J.-L., Delas, C., Gleizes, G., NedClec, A. and Cuney, M., 1992. Submagmatic microfractures in granites. Geology, 20: 35-38.

Brown, C. (1999): Mineralogy of NYF granitic pegmatites. In The Eugene E. Foord Memorial Symposium on NYF-type Pegmatites (Denver). Can. Mineral. 37, 848-849 (abstr.).

Burri, T., Berger, A., & Engi, M. (2005) Tertiary migmatites in the Central Alps: Regional distribution, field relations, conditions of formation, and tectonic implications. Sch- weizerische Mineralogische und Petrographische Mit- teilungen 85, 215–232.

Ceccato, A., Bestmann, M. and Pennacchioni, G. (2015). Multistage history of a quartz vein with increasing shear strain. Geotectonic Research 97, p. 4–6. Special Issue DRT 2015 Abstracts

Černý P., Meintzer R. E., Anderson A. J. (1985) Extreme fractionation in rare-element granitic pegmatites: selected examples of data and mechanism. Canadian Mineralogist, 23, 381-421.

Černý P. (1991a): Fertile granites of Precambrian rare-ele- ment pegmatite fields: is geochemistry controlled by tectonic setting or source lithologies? Precamb. Res. 51, 429-468.

Černý P. (1991b): Rare-element granitic pegmatites. I. Anatomy and internal evolution of pegmatite deposits. Geosci. Can. 18, 49-67.

Černý P., Ercit, T.S. (2005), The classification of granitic pegmatites revisited, The Canadian Mineralogist Vol. 43, pp. 2005-2026

Ciancaleoni, L., & Marquer, D. (2006). Syn−extension leucogranite deformation during convergence in the Eastern Central Alps: example of the Novate intrusion. Terra Nova, 18(3), 170-180.

Conforto-Galli, C., M. Spalla, G. Gosso, and A. Montrasio (1988), Synintrusive foliation of the Masino-Bregaglia tonalite and its roof pendants in Val Sissone (Val Malenco, central Alps Italy), Rend. Soc. Ital. Mineral. Petrol., 43, 509 – 516.

Cornelius, H. P. (1915), Geologische Beobachtungen in den italienischen Teilen des Albigna-Disgraziamassivs, Geol. Rundsch., 6, 166–177.

Cox, K. G., Bell, J. D. & Pankhurst, R. J. (1979). The Interpretation of Igneous Rocks. George Allen & Unwin.

Davidson, C., Schmid, S.M. and Hollister, L.S., 1994. Role of melt during deformation in the deep crust. Terra Nova, 6: 133-142.

Davidson, C., C. L. Rosenberg, and S. M. Schmid (1996), Synmagmatic folding of the base of the Bergell Pluton, central Alps, Tectonophysics, 265, 213 – 238.

Diethelm, K. H. (1989), Petrographische und geochem- ische Untersuchungen an basischen Gesteinen der bergeller Intrusion, Ph.D. thesis, Eidg. Tech. Hochsch. (ETH), Zurich.

Diethelm, K.H. (1990): Synintrusive basische Gänge und "endogene" Xenolithe: Magma-Mingling in der Bergeller Intrusion. Schweiz. Mineral. Petrogr. Mitt. 70,247-264.

Drescher-Kaden, F. K., and M. Storz (1926), Ergeb- nisse petrographischtektonischer Untersuchungen im Bergeller Granit, Neues Jahrb. Mineral., Abh., 54, 284–291.

Galli, A., Le Bayon, b., Schmidt, M.W., Burg, J.P., Reusser, E., Serggev S.A, & Larionov, A. (2012) U-Pb zircon dating of the Gruf Complex: disclosing the late Variscan granulitic lower crust of Europe stranded in the Central Alps. Contributions to Mineralogy and Petrology 163, 353–378.

Galli, A., Le Bayon, b., Schmidt, M.W., Burg, J.P., & Reusser, E. (2013) Tectonometamorphic history of the Gruf complex (Central Alps): exhumation of a granulite– migmatite complex with the Bergell Pluton. Swiss Journal of Geosciences 106, 33–6.

Gansser, A. and Gyr, T. (1964): Über Xenolith- schwärme aus dem Bergeller Massiv und Probleme der Intrusion. Eclogae geol. Helv. 57,577-598.

Gebauer, D. (1996) A P-T-t path (ultra ?) high-pressure ultra- mafic/mafic rock associations and their felsic country-rock based on SHRIMP dating of magmatic and metamorphic zircon domains. Example: Central Swiss Alps. In Earth Processes: Reading the Isotopic Code (A. Basu & S. Hart, eds.). American Geophysical Union, Monographs 65, 307–329.

Gianola, O., Schmidt, M.W., von Quadt, A., Peytcheva, I., Luraschi, P., Reusser E. (2014). Continuity in geochemistry and time of the Tertiary Bergell intrusion (Central Alps). Swiss J Geosci (2014) 107:197–222

Giger, M., and A. J. Hurford (1989), Tertiary intrusives of the central Alps; their Tertiary uplift, erosion, redeposition and burial in the South-Alpine foreland, Eclogae Geol. Helv., 82, 857–866.

Griffith, W.A., Di Toro, G., Pennacchioni, G., Pollard, D.D. (2008), Thin pseudotachylytes in faults of the Mt. Abbot quadrangle, Sierra Nevada: Physical constraints for small seismic slip events, Journal of Structural Geology 30 (2008) 1086–1094

Guastoni, A. (2012). LCT (lithium, cesium, tantalum) and NYF (niobium, yttrium, fluorine) pegmatites in the Central Alps. Exhumation history, mineralogy and geochemistry. Ph.D. Thesis, XIV° cycle, Department of Geosciences, University of Padova.

Guastoni, A., Pennacchioni, G., Pozzi, G., Fioretti, A. M., & Walter, J. M. (2014). Tertiary pegmatite dikes of the Central Alps. The Canadian Mineralogist, 52(2), 191-219.

Gyr, T. (1967): Geologische und Petrographische Un¬ tersuchungen am Ostrande des Bergeller Massivs. Mitt. aus dem Geol. Inst i tut der ETH Zürich und der Univ. Zürich NF. 66.

Hansmann, W. (1981): Geologisch-petrographische Untersuchungen im südlichen Bergell: 2. Val Ligoncio. Unpublished diploma thesis ETH Zürich.

Hansmann, W. (1996) Age determination on the Tertiary Masino-Bregaglia (Bergell) intrusives (Italy, Switzerland): a review. Schweizerische Mineralogische und Petrogra- phische Mitteilungen 76, 421–451.

Hänny, R., Grauert, b., & Soptrajanova, G. (1975) Paleozoic migmatites affected by high-grade Tertiary metamorphism in the Central Alps (Valle Bodengo, Italy). Contributions to Mineralogy and Petrology 51, 173–196.

Heilbronner, R. (2000), Optical orientation imaging, in: Stress, Strain and Structure, a Volume in Honour of W.D. Means, edited by M. W. Jessel and J. L. Urai, J. Virtual Explorer, 2, <http:// virtualexplorer.com.au/ VEjournal/Volume 2/>.

Holtz F., Johannes W., Pichavant M. (1992) Peraluminous granites: the effect of alumina on melt composition and coexisting minerals. Transactions of the Royal Society of Edinburgh, Earth Sciences 83, 409–416.

Köppel, v., Günthert, A., & Grünenfelder, M. (1980) Patterns of U-Pb zircon and monazite ages in polymetamorphic units of the Swiss Central Alps. Schweizerische Mineralogische und Petrographische Mitteilungen 61, 97–119.

Irvine, T. N. & Baragar, W. R. A. (1971). A guide to the chemical classification of the common volcanic rocks. Canadian Journal of Earth Sciences 8, 523–548.

Laubscher, H. P. (1983b), Detachment, shear and com- pression in the Central Alps, Mem. Geol. Soc. Am., 158, 191–211.

Law RD, Schmid SM, Wheeler J (1990) Simple shear deformation and quartz crystallographic fabrics: a possible natural example from the Torridon area of NW Scotland. J Struct Geol 12:29–45

Leiss, B. (2005), New techniques, measuring strategies and applications of conventional X−ray texture analysis, Conference abstracts ‘Deformation Mechanism, Rheology and Tectonics’, Zurich, Switzerland.

Leiss, B., and K. Ullemeyer (2006), Neue Perspektiven der Texturanalytik von Gesteinen mit konventioneller Röntgenbeugung, in: Symposium “Tektonik, Struktur und Kristallingeologie,” edited by S. L. Philipp et al., Universitätsverlag Göttingen, 128–130.

Liati, A., Gebauer, D., & Fanning, M. (2000). U-PbSHRIMP dating of zircon from the Novate granite (Bergell, Central Alps): evidence for Oligocene- Miocene magmatism, Jurassic/Cretaceous continental rifting and opening of the Valais trough. Schweizerische mineralogische und petrographische Mitteilungen, 80(3), 305-316.

Lister GS, Dornsiepen UF (1982) Fabric transitions in the Saxony granulite terrain. J Struct Geol 41:81–92

Mancktelow, N.S., Pennacchioni, G., 2004. The influence of grain boundary fluids on the microstructure of quartz–feldspar mylonites. Journal of Structural Geology 26, 47–69. http://dx.doi.org/10.1016/S0191-8141(03)00081-6.

Matthies, S., and G. W. Vinel (1982), An example demonstrating a new reproduction method of the ODF of texturized samples from pole figures, Phys. Status Solidi(b), 112(2), K115–K120, doi: 10.1002/pssb. 2221120255.

McDonough, W.F. and Sun, S.S., (1995), The composition of the Earth, Chemical geology, 120, 223-253

Merle, O., and B. Guiller (1989), The building of the Swiss central Alps: An experimental approach, Tec- tonophysics, 165, 41–56.

Merle, 0., 1994. Syn-convergence exhumation of the Central Alps. Geodinamica Acta, 713: 129-138.

Milnes, A.G. (1974) Structure of the Pennine Zone (Central Alps): a new working hypothesis. Geological Society of America Bulletin 85, 1727–1732.

Moticska, P. (1970), Petrographie und Strukturanalyse des westlichen Bergeller Massivs und seines Rah- mens, Schweiz. Mineral. Petrogr. Mitt., 50, 1– 355.

Nagel, T., De Capitani, C., Frey, M., Froitzheim, N., Stunitz, H., & Schmid, S.M. (2002) Structural and metamorphic evolution during rapid exhumation in the Lepontine dome (southern Simano and Adula nappes, Central Alps, Switzerland). Eclogae geologicae Helvetiae 95, 301–321.

Nizamoff, J.W., Falster, A.U., Simmons, W.B. & Webber, K.L. (1999): Phosphate mineralogy of NYF-, LCT- and mixed-type granitic pegmatites. In The Eugene E. Foord Memorial Symp. on NYF-type Pegmatites (Denver). Can. Mineral. 37, 853-854 (abstr.).

Oschidari, H., & Ziegler, U. R. F. (1992). Vergleichende Sm-Nd- und Rb-Sr-Untersuchungen an Bergeller Gero¨llen aus der Gonfolite Lombarda („Su¨dalpine Molasse“) und an Bergeller und Novate Granitoiden des Ursprungsgebietes. Eclogae Geologicae Helve- tiae, 85, 375–384.

Panozzo Heilbronner, R., and C. Pauli (1993), Integrated spatial and orien- tation analysis of quartz c−axes by computer−aided microscopy, J. Struct. Geol., 15(3–5), 369–382, doi: 10.1016/0191-8141(93)90133-U.
Passchier, C.W., Trouw, R.A.J., 2005. Microtectonics, second ed. Springer, Berlin.

Patino Douce A. E. (1996) Effects of pressure and H2O content on the. compositions of primary crustal melts. Transactions of the Royal Society of Edinburgh, Earth Sciences 87, 11–21.

Peacock M.A. (1931) Classification of igneous rock series. Journal of Geology, 39, 54-67.

Pennacchioni, G. (2005), Control of the geometry of precursor brittle structures on the type of ductile shear zone in the Adamello tonalites, Southern Alps (Italy), J. Struct. Geol., 27(4), 627–644, doi:10.1016/j. jsg.2004.11.008.

Pennacchioni, G., and N. S. Mancktelow (2007), Nucleation and initial growth of a shear zone network within compositionally and structurally heterogeneous granitoids under amphibolite facies conditions, J. Struct. Geol., 29(11), 1757–1780, doi:10.1016/j.jsg.2007.06.002.

Pennacchioni, G., Menegon, L., Leiss, B., Nestola, F., & Bromiley, G. (2010). Development of crystallographic preferred orientation and microstructure during plastic deformation of natural coarse−grained quartz veins. Journal of Geophysical Research: Solid Earth (1978–2012), 115(B12).

Pennacchioni, G., & Zucchi, E. (2013). High temperature fracturing and ductile deformation during cooling of a pluton: The Lake Edison granodiorite (Sierra Nevada batholith, California). Journal of Structural Geology, 50, 54-81.

Piccoli, G (1961): Metasomatismo e migmatiti nelle rocce verdi di Novate Mezzola (Sondrio, Alpi Lombarde). Rend. Soc Mineral. Ital. 17,427^154.

Pozzi, G. (2014). Tertiary pegmatite dikes in the Codera and Bodengo areas of the Central Alps. M.Sc. Thesis, Department of Geosciences, University of Padova.

Repossi. E. (1915). La bassa Valle della Mera. Studi petrografici e geologici II Mem. Soc Ital. Sci. Nat. Milano 8,186 pp.

Reusser, C. E. (1987), Phasenbeziehungen im Tonalit der Bergeller Intrusion, Ph.D. thesis, Eidg. Tech. Hochsch. (ETH), Zurich.

Romer, R.L., Schärer, U., & Steck, A. (1996) Alpine and pre-Alpine magmaism in the root-zone of the western Central Alps. Contributions to Mineralogy and Petrology 123, 138–158.

Rosenberg, C, Berger, A. and Heilbronner, R. (1994): Deformation of polyphase rocks at different temperature conditions (1): rheological versus mineralogical phases in the Bergell tonalite. Annales Geophysicae 12 (Abstract)

Rosenberg, C. L., A. Berger, and S. M. Schmid (1995), Observations from the floor of a granitoid pluton: Inferences on the driving force of final emplacement, Geology, 23, 443–446.

Rosenberg, C. L., and F. Heller (1997), Tilting of the Bergell pluton and Central Lepontine area: Com- bined evidence from paleomagnetic, structural and petrological data, Eclogae Geol. Helv., 90, 345 – 356.

Rosenberg, C. L., and H. Stünitz (2003), Deformation and recrystallization of plagioclase along a tempera- ture gradient: An example from the Bergell tonalite, J. Struct. Geol., 25, 389–408.

Rosenberg, C. L. (2004). Shear zones and magma ascent: a model based on a review of the Tertiary magmatism in the Alps. Tectonics, 23, TC3002.

Rubatto, D., Hermann, J., Berger, A., & Engi, M. (2009) Protracted fluid-induced melting during Barrovian meta- morphism in the Central Alps. Contribution to Mineralogy and Petrology 158, 703–722.

Salomon, W. (1897), Uber Alter, Lagerungsform und Entstehungsart der periadriatischen granitisch kornigen Massen, Tschermaks Mineral. Petrogr. Mitt., 17, H 2/3, 109–284.

Schärer, U., Cosca, M., Steck, A., & Hunziker, J. (1996) Termination of major ductile strike-slip shear and differ- ential cooling along the Insubric line (Central Alps): U-Pb, Rb-Sr and 40Ar/39Ar ages of cross-cutting pegmatites. Earth and Planetary Science Letters 142, 331–351.

Schmid, S.M.. Rück, P. and Schreurs, G. (1990): The significance of the Schams nappes for the recon¬ struetion of the paleotectonic and orogenic evolu¬ tion of the Penninic zone along the NFP 20 East Tra¬ verse (Grisons, eastern Switzerland). Mein. Soc. gSol. France 156,263-287.

Schmid. S.M. and Froitzheim, N. (1993): Oblique slip and block rotation along the Engadine line. Eclogae geol. Helv., 569-593.

Schmid,S.M., A.Berger, C.Davidson, R.Gieré, J. Hermann, P. Nievergelt, A. R. Puschnig, and C. Rosenberg (1996b), The Bergell pluton (south- ern Switzerland, northern Italy): Overview accom-

panying a geological-tectonic map of the intrusion and surrounding country rocks, Schweiz. Mineral. Petrogr. Mitt, 76, 329–355.

Staub, R. (1918), Geologische Beobachtungen am Bergellermassiv, Vjschr. Natf. Ges. Zu¨rich, 63, 1–18.

Stern, W.b. (1966) Zur Mineralchemie von Glimmern aus Tessiner Pegmatiten. Schweizerische mineralogische und petrographische Mitteilungen 86, 137–188.

Stipp M, Stünitz H, Heilbronner R, Schmid SM (2002) The eastern Tonale fault zone: a “natural laboratory” for crystal plastic de- formation of quartz over a temperature range from 250 to 700 °C. J Struct Geol 24:1861–1884

Stüder, b. (1851) Geologie der Schweiz. Stämpfli, Bern, Germany (485).

Taylor & Heier,K.S. (1960) The petrological significance of trace elements variations in alkali feldspars. Int. Geol. Congress 21st (Norden)14, 47-61.

Taylor S.R. (1963) The application of trace element data to problems in petrology. Physics and Chemistry of the Earth 6, 133-213

Trommsdorff, V., and P. Nievergelt (1983), The Brega- glia (Bergell) Iorio intrusive and its field relations, Mem. Soc. Geol. Ital., 26, 55–68.

Villa, I. M., and F. von Blanckenburg (1991), A horn- blende 39Ar-40Ar age traverse of the Bregaglia tonalite (southeast central Alps), Schweiz. Mineral. Petrogr. Mitt., 71, 73–87.
vILLA, I.M. (1998) Isotopic closure. Terra Nova 10, 42–47.

Von Blanckenburg, F. (1992). Combined high-precision chronometry and geochemical tracing using accessory minerals: applied to the Central-Alpine Bergell intrusion (central Europe). Chemical Geology, 100(1), 19-40.

Wassermann, G., and J. Grewen (1962), Texturen metallischer Werkstoffe, Springer−Verlag, Berlin.

Wenk, E. (1970). Zur regionalmetamorphose und Ultrametamorphose im Lepontin. Fortschr. Mineral, 47, 34-51.

Wenk, H. R. (1973). The structure of the Bergell Alps. Eclogae Geol. Helv, 66, 255-291.

Wenk, H.R. (1986): Introduction to the geology of the Bergell Alps with Guide for Excursions. Jber. Natf. Ges. Graubünden 103,29-90.

Wenk, H.R. and Cornelius, S.B. (1977): Geologischer Atlas der Schweiz. 1 : 25'000. Blatt 70 Sciora. Schweiz. Geol. Kommission.

Wenk, HR.. Hsiau, J., Flowers. G., Weibel, M., Ayranci, B. and Fejér, Z. (1977): A geochemical survey of granitic rocks in the Bergell Alps. Schweiz. Mineral. Petrogr. Mitt. 57,233-265.

Wenk, H. R. (1985), Preferred orientation in deformed metals and rocks: An introduction to modern texture analysis, Academic Press, Orlando, Florida.

Wenk, H. R., S. Matthies, J. Donovan, and D. Chateigner (1998), BEARTEX: a Windows−based program system for quantitative texture analysis, J. Appl. Crystallogr., 31(2), 262–269, doi: 10.1107/ S002188989700811X.

Wilson CJL (1975) Preferred orientation in quartz ribbon mylonites. Bull Geol Soc Am 86:968–974

Wilson, M. (1989). Igneous Petrogenesis. London: Unwin Hyman.

Wise, M.A. (1999), Characterization and classification of NYF-type pegmatites. In The Eugene E. Foord Memorial Symp. on NYF-type Pegmatites (Denver). Can. Mineral. 37, 802-803 (abstr.).

Wolf M.B., London D. (1995) Incongruent dissolution of REE and Sr-rich apatite in peraluminous granitic liquids: differential apatite, monazite, and xenotime solubilities during anatexis. American Mineralogist 80, 765–775.

ANALYTICAL TECHNIQUES

Scanning Electron Microscope (SEM)

A CamScan MX2500 SEM, equipped with a LaB6 cathode, a four quadrant solid state BSE (Backscattered Electrons) detector and EDAX-EDS (Energy Dispersive Spectroscopy) system has been used for microstructural observation. The analytical conditions were: accelerating voltage = 20 kV, filament emission ~60 μA, beam current ~100 nA, working distance ~21-24 mm.

X-Ray Fluorescence (XRF) analysis

Representative samples of pegmatite and granite were analysed by X-ray fluorescence spectrometry (XRF) for major and trace elements composition. The analyses were carried out on fused glass discs (1:10 ratio with flux $Li_2B_4O_7$) using a WDS sequential Philips PW2400 spectrometer, operating under vacuum conditions and equipped with: 3 kW Rh X-ray tube, 5 analysing crystals (LiF220, LiF200, Ge, PE, TlAP), 2 detectors (flow counter and scintillator), 3 collimators (150 μm, 300 μm and 700 μm), 4 filters (Al 200 μm, Brass 100 μm, Pb 1000 μm and Brass 300 μm).

Computer Integrated Polarization Microscopy

The photomicrographs used to derive the CIP pole figures were acquired with a Zeiss AxioCam MRm digital camera on a Zeiss Axioplan microscope. Images are oriented with the top and bottom edges parallel to the shear zone boundaries (XY plane of the bulk finite strain). For all CIP analyses, a magnification of 2.5 × was used. With this setup, the pixel size is 6 mm^2 and the area of individual regions of interest ranges from 4 to 7 mm^2 (0.7 to 1.2 megapixels). The main goal of the CIP analysis was not to represent the bulk texture but to understand the texture of a particular microstructural domain. The CIP analysis estimates the c−axis orientation at each pixel of the image and derives (i) area−weighted pole figures and (ii) c−axis orientation images (COI) according to two−dimensional color look−up tables (CLUTs). For each measured domain the bulk pole figure was calculated. The c−axis orientation images were visualized by means of a spectrum CLUT that represents the Z direction in blue, the X direction in yellow, and the Y direction in white.

X−ray Texture Goniometry

The pole−figure measurements for quantitative texture analysis were carried out on a PANalytical X−ray texture measuring system installed at the Geoscience Centre of the University of Göttingen, Germany (Leiss, 2005; Leiss and

Ullemeyer, 2006). A poly-capillary glass fiber lens at the primary beam side provides high X-ray intensities, an optically parallel beam, and an exceptionally large beam size of up to 7 mm. This allows a short measuring time per pole figure (1 s per pole-figure direction at an anode current of 40 mA and a voltage of 40 kV), a high resolution, and a relative large measured volume. Computer-controlled sample movement allows automated measurements of a series of local textures on a regular or irregular grid within a polished sample area of 100 × 100 mm. This provides a control on the texture homogeneity of the sample texture and/or improves the measuring statistics especially for coarse-grained samples by accumulating several pole-figure measurements into a bulk pole figure. In the case of the coarse-grained WDV and MDV samples, we accumulated up to six local texture measurements to establish a representative global texture of the samples. A standard pole-figure measuring grid of 5° × 5° was applied for quartz (100), (101), (110), (102), (111), (200), (201), (112), (211) and for background measurement. After subtraction of the background from the quartz measurements, a defocusing correction based on functions derived from pole-figure measurements of quartz powder (e.g., Wassermann and Grewen, 1962; Wenk, 1985) was carried out. At high tilt angles, reasonable defocusing corrections are not possible, therefore measurements were cut off at a tilt angle of 85°, leading to incomplete pole figures. The orientation distribution function (ODF) values in three-dimensional orientation space were calculated by means of the WIMV algorithm (Matthies and Vinel, 1982), included in the BEARTEX software package (Wenk et al., 1998). From the results of the ODF, full pole figures and pole figures that cannot be directly measured, such as quartz (001) (c axis), were calculated.

ACKNOWLEDGEMENT

I would like to express my gratitude toward my supervisor Prof. Giorgio Pennacchioni who gave me the opportunity to do this project. I am very thankful to him for his constant supervision.
I am highly indebted to Alberto Ceccato, for giving me such attention, help and time.
I would also like to thank: Prof. Luciano Secco for his supervision on mineral separation and for logistical support; Anna Maria Fioretti for her precious contribution in mineral separation and geochemistry; Alessandro Guastoni who took the samples; Leonardo Tauro (thin section preparation and SEM), Sandra Boesso (mineral separation), Luca Peruzzo (rock crushing), Daria Pasqual (XRF spectrometry) and Stefano Castelli (photography) for technical support.
Microphotographs for the CIP analysis were taken by Alberto Ceccato at the University of Basel (Switzerland). Photographs for photomosaics were taken and processed by Giorgio Pennacchioni. Several photographs taken in the field are courtesy of Giorgio Pennacchioni, Alessandro Guastoni, Alberto Ceccato, Mariangela Schiazza and Daniele Giuliani. The X−ray texture goniometer analysis was carried out by Prof. Bernd Leiss at the University of Göttingen (Germany).